THE UNIVERSITY OF CHICAGO

STRUCTURAL INSIGHTS INTO THE FORMATION OF AXON GUIDANCE COMPLEXES

A DISSERTATION SUBMITTED TO

THE FACULTY OF THE DIVISION OF THE BIOLOGICAL SCIENCES

AND THE PRITZKER SCHOOL OF MEDICINE

IN CANDIDACY FOR THE DEGREE OF

DOCTOR OF PHILOSOPHY

GRADUATE PROGRAM IN BIOCHEMISTRY AND MOLECULAR BIOPHYSICS

BY

JESSICA MARIE PRIEST

CHICAGO, ILLINOIS

DECEMBER 2023

To my dad, Russell Priest, for his unwavering love and support. You are missed.

1965-2022

“And so, does the destination matter? Or is it the path we take? I declare that no accomplishment has substance nearly as great as the road used to achieve it. We are not creatures of destinations. It is the journey that shapes us. Our callused feet, our backs strong from carrying the weight of our travels, our eyes open with the fresh delight of experiences lived.”

—Brandon Sanderson, *The Way of Kings*

TABLE OF CONTENTS

LIST OF FIGURES

LIST OF TABLES

ABBREVIATIONS

AP	Alkaline phosphatase
ASU	Asymmetric unit
AU	Arbitrary unit
AVEXIS	Avidity-based Extracellular Interaction Screening
Beat	Beaten Path protein
BMP	Bone morphogenetic protein
BMPR	Bone morphogenetic protein receptor
BPIA	Bio-Plex Interactome Assay
BSA	Bovine serum albumin
CAR	Coxsackievirus and adenovirus receptor
CNS	Central nervous system
COMP	Cartilage oligomeric matrix protein
CRISPR/Cas9	Clustered regularly interspaced short palindromic repeats/CRISPR-associated protein 9
Cryo-EM	Cryogenic electron microscopy
CSSP	Cell surface and secreted proteins
CV	Column volume
Da	Dalton
DCC	Deleted in Colorectal Cancer receptor
DD	DEATH domain
DIC	Differential interference contrast
DIP	Dpr-interacting protein

Dpr	Defective proboscis extension response protein
DSCAM	Down syndrome cell adhesion molecule
ECD	Extracellular domain
ECIA	Extracellular Interactome Assay
ECM	Extracellular matrix
EGF	Epidermal growth factor
ELISA	Enzyme-linked immunosorbent assay
Fc	Fragment crystallizable region
FN3	Fibronectin type-III domain
FP	Floor plate
GABA	Gamma-aminobutyric acid
GAG	Glycosaminoglycan
GPI	Glycophosphatidylinositol
HBS	HEPES-buffered saline
HBS-MS	10 mM HEPES pH 7.2, 150 mM NaCl, 100 mM $MgSO_4$
HEPES	N-2-hydroxyethylpiperazine-N'-2-ethanesulfonic acid
HS	Heparan sulfate
HSPG	Heparan sulfate proteoglycan
IG	Immunoglobulin domain
IgSF	IG superfamily
ipTM	Interface predicted template modeling score
ISN	Intersegmental nerve
JAML	Junctional adhesion molecule–like protein

K_D	Dissociation constant
LamVI	Laminin VI domain
LAR	Leukocyte common antigen-related receptor
LOF	Loss-of-function
MALS	Multi-angle light scattering
MFI	Mean fluorescence intensity
MW	Molecular weight
NGM	Nematode growth media
NMJ	Neuromuscular junction
NTA	Nitriloacetic acid
NTR	Netrin-like domain
PBS	Phosphate-buffered saline
PDB	Protein Data Bank
PDZ	Postsynaptic density protein of 95 kDa, *Drosophila* disc large tumor suppressor, and ZO-1
PIDD	P53-induced protein with a death domain
PMSF	Phenylmethylsulfonyl fluoride
PPI	Protein-protein interaction
Robo	Roundabout receptor
RP	Roof plate
SAXS	Small-angle X-ray scattering
SDN-1	Syndecan-1
SDS-PAGE	Sodium dodecyl-sulfate polyacrylamide gel electrophoresis

SEC	Size-exclusion chromatography
Side	Sidestep protein
SNa-d	Segmental nerve a-d
SPR	Surface plasmon resonance
SV	Synaptic vesicle
SYG-1 and -2	Synaptogenesis abnormal-1 and -2 protein
TSP	Thrombospondin type-I domain
UNC	Uncoordinated
UPA	Unc5/PIDD/Ankyrin
WT	Wild-type
ZO-1	Zonula occludens-1 protein
ZU-5	ZO-1/Unc5

ACKNOWLEDGEMENTS

This dissertation would not be possible without the collective efforts of numerous individuals who I owe my deepest and sincerest gratitude.

To my thesis advisor, Dr. Engin Özkan: You've been dreaming about publishing the Netrin story since 2006. I am honored to contribute to a project that spans decades of work. Thank you for trusting me with your passion project; I hope I did it justice. I would be remiss not to mention your enthusiastic mentorship, always offering guidance (pun intended). I deeply appreciate all that you've done for me.

To my thesis committee, Dr. Juan Mendoza, Dr. Minglei Zhao, and Dr. Robert Carrillo: Thank you for taking the time and energy to provide invaluable feedback, in addition to filling out too many availability polls to arrange meetings. I am lucky to have all my committee members as collaborators. To Juan, my chair, you spent hours personally teaching me the ins and outs of yeast surface display. You never failed to answer my questions promptly, no matter how silly. Thank you for being a great teacher. To Minglei, who not only graciously offered to collect cryo-EM data for me but also reprocessed my existing cryo-EM and negative stain data, thank you for lending me your expertise. To Robert, thank you and your lab, especially Dr. James Ashley and Ruiling (Renee) Zhang, for contributing to the Beat-Side project.

To my collaborators: I am fortunate to have several collaborators, in addition to Juan, Minglei, Robert, James, and Renee. To Dr. Kang Shen and Ev Nichols from Stanford University, Dr. Jesse Hopkins from Argonne National Laboratory, Szymon Kordon and Dr. Agnieszka Olechwier from the University of Chicago, Dr. Rob Meijers from the Institute for Protein Innovation, and Dr. Robert Smock from the European Molecular Biology Laboratory, thank you for your contributions to my graduate research.

To the Özkan lab members: You are all fantastic scientists and it was a privilege to work together. To my (first and only, therefore the best!) mentee, Asaf Lebovic, I owe you a tremendous debt for all the gels you ran for me.

To my family: To my mom and brothers, Tyler and Jared, thank you for shaping me into who I am today. To my dad, who never saw this adventure completed, I am eternally grateful to have you for the time that I did. You were always bragging about your "scientist daughter" to anyone and everyone. I know you would have been my loudest and proudest supporter.

To my friends: I am a firm believer that family is not just who you are related to but who you choose to surround yourself with. To Victor, you are truly a compassionate and wonderful person. To Esmeralda, despite being separated by nearly 800 miles, we manage to talk almost every day. Not many people can say they have a friend as supportive or encouraging as you. To my boyfriend's family, Mary, Scott, Freddy, Joey, Holly, and Jeff, you welcomed me with open arms even though I am a terrible golfer. Thank you all for being a part of my chosen family.

Lastly, to Bobby: Nothing I write will accurately put into words the impact you've had on my life. You are incredibly kind and understanding, never doubting I'd succeed. Thank you for coming on this journey with me; here's to many more adventures. P.S. I finally outrank your MST.

ABSTRACT

Given the magnitude of the neuronal population and the degree of neural connectivity, the intricate nature of the human nervous system is undeniable. How do neurons reach their proper targets in a highly complex and dynamic environment? Despite their importance, only a small number of molecules have been shown to create neural circuits or specify synapse locations. My work aims to explore and clarify the mechanisms behind directed cellular and axonal growth, synapse formation and development, addressing crucial gaps in our understanding.

Chapter 1 reviews our current knowledge regarding the development and wiring of the nervous system. Cell-surface receptors bind to extracellular guidance cues, directing neurons to their intended targets. These cues create intracellular signaling responses, resulting in cytoskeleton remodeling and translocation of the growth cone. The emphasis on commissural axonal guidance at the central midline and motor axon pathfinding supports later chapters 2 and 3.

Chapter 2 focuses on repulsive Netrin guidance complexes. The extracellular cue UNC-6/Netrin regulates a variety of biological functions, including axon guidance, cell morphology, axon branching, and cell adhesion, by binding to cell-surface receptors. As a result, there is a strong disease association with UNC-6/Netrins, implicated in neurological disorders as well as cancer, cardiovascular disease, and diabetes. My work characterizes the poorly understood interaction between UNC-6/Netrin and its repulsive axon guidance receptor UNC-5, elucidating the molecular mechanism of repulsive axon signaling and UNC-6/Netrin-dependent cell survival, valuable information for the design and creation of therapeutic agents to treat Netrin-associated diseases.

Chapter 3 discusses the Beaten Path (Beat)-Sidestep (Side) interactome. This network of cell surface receptors is combinatorically expressed and can act as molecular identity tags on Beat-expressing motor neurons and their Side-expressing sensory neuron or muscle cell partners. Beat-Side binding influences axon growth, defasciculation, and synaptic formation. This neuronal *Drosophila melanogaster* protein family serves as a model to investigate the development of neuromuscular junctions and motor axon pathfinding. My work presents the first known Beat-Side complex structure, giving key structural and mechanistic details of how these proteins interact.

CHAPTER 1: INTRODUCTION

1.1 Why did the commissural axon cross the midline? To get to the other side.

1.1.1 Navigation in the ventral midline of the central nervous system

During the development of the human nervous system, over 10^{11} neurons send their axons out to make connections with target cells, establishing an outstanding 10^{15} synaptic connections[1]. In order to reach their intended targets, the axons need to travel in a complex and ever-changing environment, avoiding a myriad of obstacles. The nervous system has the daunting task of establishing these connections at the right time and location. Wiring errors result in neurological disorders, such as Schizophrenia[2], autism spectrum disorder[3,4], Alzheimer's disease[5], and bipolar disorder[6]. Gene mutations in patients with mental and neurological disorders often disrupt neural wiring by affecting axon guidance, synapse formation, and synapse assembly[7].

In the late 1800s, Santiago Ramón y Cajal, known as the father of modern neurobiology, made major breakthroughs towards understanding the complexity of the nervous system[8]. Cajal studied the spinal cords of chick embryos and observed that axons move through their environment "without deviation or error, as if guided by an intelligent force." Using the Golgi staining method to identify structural details, Cajal produced the first drawings of the axonal growth cone[9]. Growth cones are located at the leading edge of an axon and are highly dynamic. Extracellular cues induce structural changes within the growth cone, where cytoskeleton remodeling dictates the course and rate of growth of the developing axon. Once the neuron reaches the target, the growth cone turns into a presynaptic terminal, allowing signal transmission between the neuron and the postsynaptic cell[1]. Although Cajal, and later Roger Sperry[10], postulated the existence of axon guidance cues, one was not discovered until the 1980s

in model organisms, such as *Caenorhabditis elegans*. One of these cue discovered early was UNC-6, which belonged to the Netrin protein family[11]. Netrin is derived from the Sanskrit "netr", appropriately meaning "the one who guides"[12].

Bilaterians have bilateral symmetry where the left and right sides of the body are mirror images. A significant portion of neurons within the central nervous system (CNS) are contralateral, crossing the midline at commissures that link the two sides. These commissural neurons lead to each half of the brain controlling the opposite half of the body. At the midline, neuronal circuitry must assemble in a precise manner for proper left-right coordination[13,14].

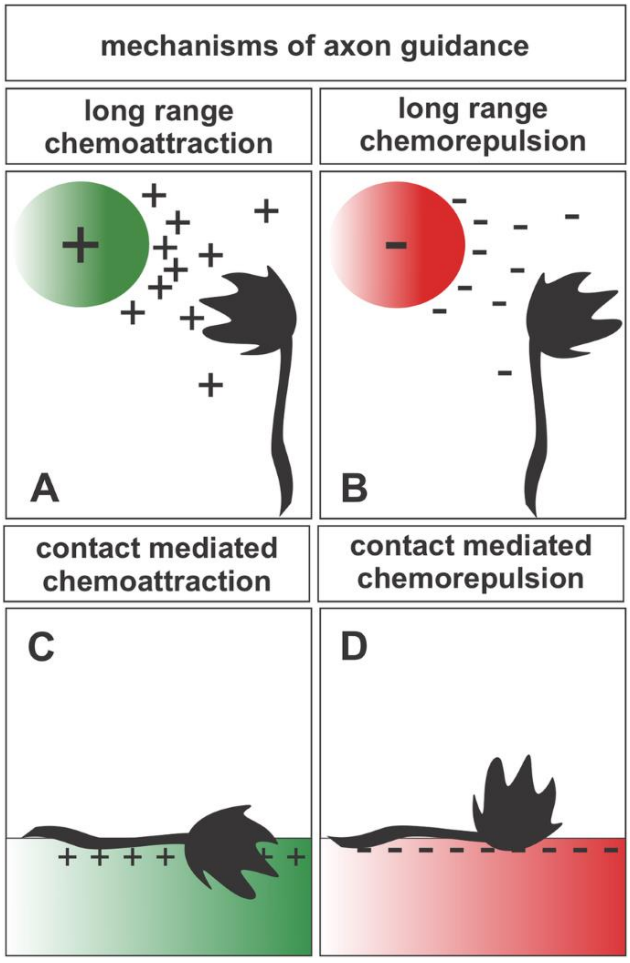

Figure 1.1. Long-range and short-range chemoattraction and chemorepulsion are mechanisms of axon guidance (from Comer et al. 2019).

Continued on next page.

Figure 1.1 continued. Molecular guidance cues can attract or repel growing axons over long and short distances. **A,B.** Long-range cues are diffusible and secreted. **C,D.** Short-range cues are non-diffusible, and the neuron must come into direct contact with them for signal transduction.

A conserved set of wiring molecules establishes synaptic connectivity of the nervous systems in bilaterian animals, including those that guide the growth of axons and determine synaptic partners[15–17]. These molecules can attract or repel growing axons via short- and long-range mechanisms[18]. Long-range cues are soluble, acting at a distance (**Figure 1.1A-B**), while short-range cues are substate bound to the extracellular matrix (ECM) or cell surfaces and signal through direct contact with the neuron (**Figure 1.1C-D**)[1].

In vertebrates, commissural neurons cross at the ventral midline. The floor plate (FP) and the roof plate (RP) exist along the midline of the spinal cord at the dorsal and ventral sides, respectively (**Figure 1.2A**). Commissural neurons traverse ventrally to the midline, where they cross and then move rostrally or caudally. Ligand-receptor pairs ensure directionality. First, a group of cues repel the axon from the RP. Bone morphogenetic proteins (BMPs) secreted from the RP, chemorepellents, signal by binding bone morphogenetic protein receptors (BMPRs) (**Figure 1.2B**)[1,19–21]. Then, Netrins secreted from the FP, acting as chemoattractants, direct the axon to the FP by binding to Deleted in Colorectal Cancer (DCC) receptors (**Figure 1.2C**)[1,19–22]. Once the neuron crosses the midline, it does not re-cross, successfully establishing its contralateral projection. To prevent re-crossing, the neuron loses its response to attractive signals in the FP. This switch occurs through the expression of novel, repulsive receptors or the loss of expression of pre-existing, attractive receptors[20]. Once the axon crosses the ventral midline, Roundabout (Robo) receptor expression is upregulated. Robo receptors bind to FP-derived Slit to repel the axon (**Figure 1.2D)**[1,19–21].

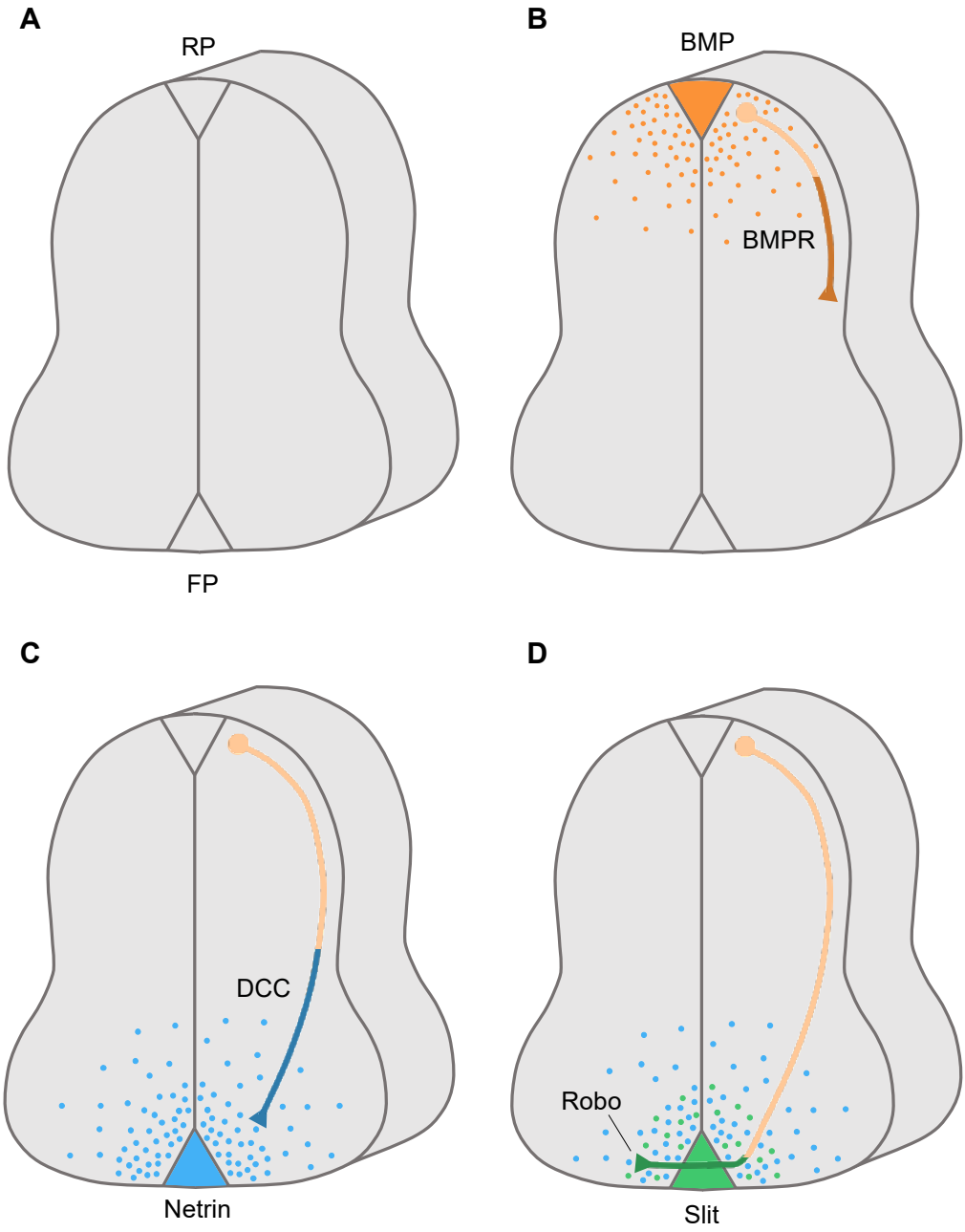

Figure 1.2. Schematic of a commissural interneuron traveling through the vertebrate spinal cord.

A. Diagram of a cross-section of the vertebrate spinal cord showing the midline, RP, and FP. **B.** The axon originates on the dorsal side of the spinal cord. RP-derived BMPs bind to BMPRs on the axon, repelling the neuron from the dorsal side. **C.** FP-derived Netrins bind to DCC receptors on the axon, attracting the neuron ventrally. **D.** Once the axon crosses the ventral midline, the axon loses its attraction to the FP. The expression of Robo receptors is upregulated. Robo-Slit binding acts as a chemorepellent, ensuring that the axon does not recross the midline.

1.1.2 Netrins and their receptors

Netrins are guidance cues that are unique in their ability to exert attractive and repulsive responses on growing axons[1]. In addition to their neuronal functions, Netrins and their receptors are known to control cell proliferation, migration, differentiation, and survival; thus, they are targets for treating a multitude of diseases, including cancer and diabetes[23–25]. Discovered first in *C. elegans*, Netrins are highly conserved, existing in all bilaterians. They are related to laminins with the typical structure of an N-terminal laminin VI domain (LamVI), three epidermal growth factor (EGF) repeats, and a C-terminal Netrin-like domain (NTR domain) (**Figure 1.3**)[26]. Instead of an NTR domain, Netrin-G proteins contain a glycophosphatidylinositol (GPI) anchor on the C-terminal end. Netrins are secreted, except for Netrin-Gs, which are tethered to the plasma membrane[17,27–29].

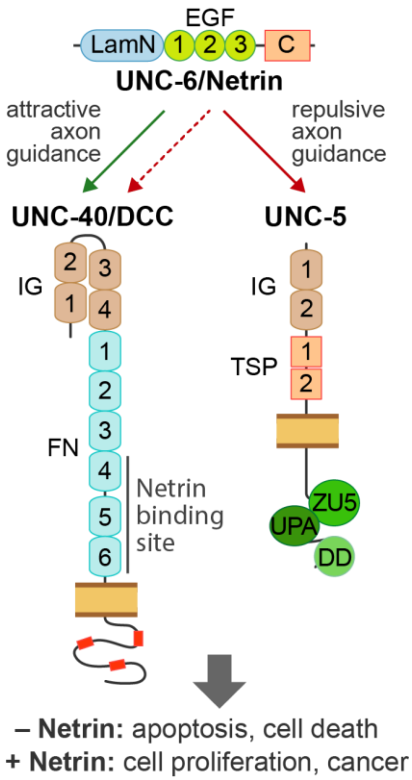

Figure 1.3. Domains and functions of Netrin and its receptors.

Continued on next page.

Figure 1.3 continued. While UNC-6/Netrin-mediated attractive responses require UNC-40/DCC, UNC-40/DCC may be needed for repulsive responses with the cooperation of UNC-5. Both UNC-40/DCC and UNC-5 are dependence receptors, where absence of the ligand, UNC-6/Netrin, is pro-apoptotic and ligand binding promotes cell proliferation.

Netrin receptors are part of the immunoglobulin (IG) superfamily (IgSF) and are single-pass transmembrane proteins. The focus of Chapter 2 is on the interactions of Netrins with the DCC and UNC-5 receptor families. However, an additional receptor, Down syndrome cell adhesion molecule (DSCAM), binds to Netrin and interacts with the other receptor families, although its exact mechanisms are not known[30–32]. The EGF repeats and LamVI of Netrins bind to the extracellular regions of the DCC and UNC-5 receptor families[12]. The NTR domain is not required for binding and is not found in all Netrins[17]. Netrin receptors can form either hetero- or homodimers for axon attraction or repulsion. The DCC class of receptors (named UNC-40 in nematodes) are required for both attractive and repulsive responses, while UNC-5 receptors are required only for repulsive responses (**Figure 1.3**)[33]. See **Table 1.1** for nomenclature in the model organisms *Mus musculus, C. elegans,* and *Drosophila melanogaster*[17].

Protein Family	*M. musculus*	*D. melanogaster*	*C. elegans*
Netrin	Netrin-1 Netrin-3 Netrin-4 Netrin-5 Netrin-G1 Netrin-G2	Net-A Net-B	UNC-6
DCC	DCC Neogenin	Frazzled	UNC-40
UNC-5	Unc5A Unc5B Unc5C Unc5D	Unc-5	UNC-5

Table 1.1. Netrin, DCC, and UNC-5 family proteins in model organisms.

Nomenclature in the model organisms *M. musculus, C. elegans,* and *D. melanogaster*.

DCC family receptors contain four IG domains and six fibronectin type III (FN3) repeats in their extracellular region. They have no defined domains in their cytoplasmic region; instead, they contain three peptide motifs: P1, P2, and P3 (**Figure 1.3**)[29,34]. For attractive signaling, Netrins can cause oligomerization or clustering of DCC/Neogenin through the interaction of the receptors with multiple binding sites on Netrin molecules, bringing P3 motifs together (**Figure 1.4**). Such oligomerization likely leads to the proximity of intracellular signaling molecules recruited at motifs conserved in DCC/Neogenin cytoplasmic domains[35].

UNC-5 family receptors contain two IG domains and two thrombospondin type-I (TSP) domains (**Figure 1.3**). Unlike DCC family receptors, UNC-5 family receptors have defined domains in their cytoplasmic region: Zonula occludens-1 (ZO-1)/Unc5 (ZU-5), Unc5/P53-induced protein with a death domain (PIDD)/Ankyrin (UPA), and DEATH Domain (DD)[34,36]. The P1 motif of DCC interacts with the UPA of UNC-5 to initiate long-range repulsion (**Figure 1.4**)[12,37]. It is not clear, however, how Netrin can induce repulsive responses, as there is only limited biochemical characterization and structural information for the proposed Netrin–UNC-5 complexes.

First discovered due to its association with Down syndrome, DSCAM is a transmembrane cell adhesion receptor containing nine IG domains and six FN3 domains, making it one of the largest members of the IgSF[38]. DSCAM is a co-receptor for both DCC and UNC-5, although the mechanisms and roles in axon guidance are poorly understood (**Figure 1.4**)[12,30]. Homologs of DSCAM exist in vertebrates and *D. melanogaster* but not *C. elegans*[17].

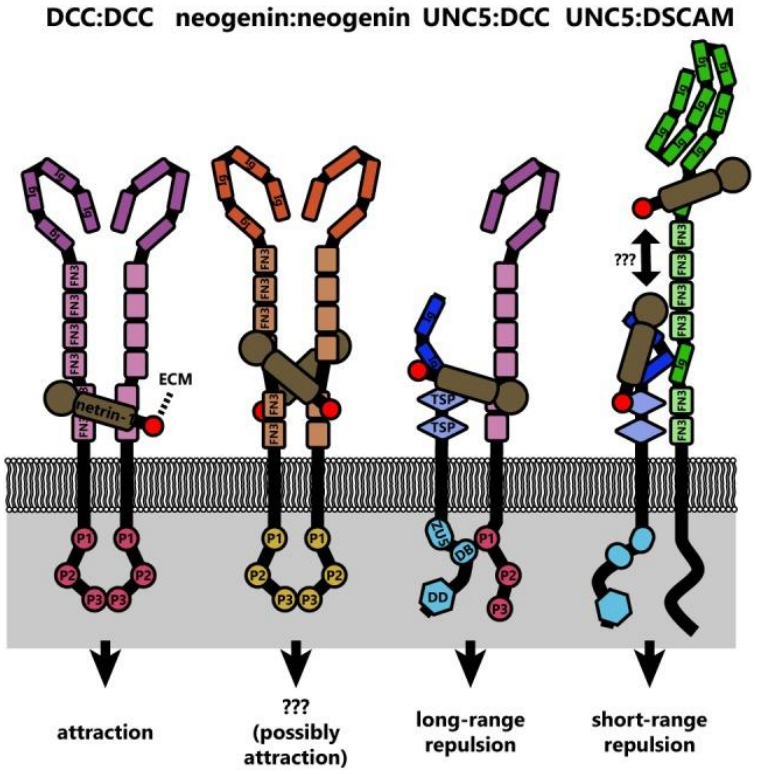

Figure 1.4. Netrin-1 receptor homodimers and heterodimers bound to Netrin-1 (from Boyer and Gupton et al. 2018).

Netrin receptors dimerized, bringing their cytoplasmic regions into close proximity for downstream signaling.

1.1.3 Role of glycosaminoglycans and proteoglycans

Another important player in the Netrin guidance system is glycosaminoglycans (GAGs) such as heparan sulfate (HS), which are present on cell surfaces and in the extracellular matrix in the form of proteoglycans. GAGs are acidic, negatively charged molecules with multiple mechanistic roles in the formation of ligand-receptor complexes. A GAG can facilitate complex formation by acting as a molecular bridge or bringing the molecules into close proximity. Alternatively, GAGs can repress ligand-receptor binding by physically blocking the interaction. By acting as both an activator and a repressor, a GAG can favor the formation of one complex over another, operating as a selector (**Figure 1.5**)[39].

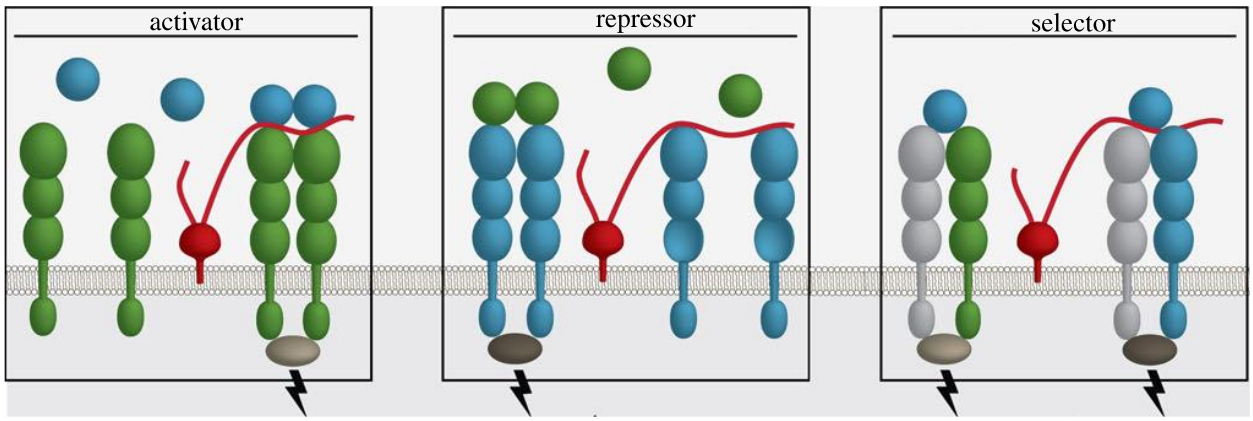

Figure 1.5. GAGs are molecular switches in complex formation (from Smock and Meijers 2018).

Through their interactions with ligand-receptor complexes, GAGs can act as an activator or repressor of complex formation. By acting as a activator of one complex and a repressor of another, GAGs can select for the formation of certain ligand-receptor pairs.

Netrins were first purified from tissue with the help of their strong affinity for heparin[26]. Their relevance for signaling has also been recognized, as lack of the HS-polymerizing enzyme, Ext1, leads to defective Netrin- and DCC-mediated axon guidance in mouse spinal cord commissural neurons[40]. Mutations in two heparan sulfate proteoglycans (HSPGs), syndecan (SDN-1) and glypican (LON-2), show defects in UNC-6/Netrin-mediated repulsive dorsal guidance of motor axons in *C. elegans*. A screen searching for mutations to enhance HSPG-dependent guidance pathway defects identified multiple *unc-5* mutants, hinting at an interaction between UNC-5 and HSPGs[41]. Similarly, mutations in the HSPG *unc-52/perlecan* enhance distal tip cell migration defects of *unc-5* hypomorphs[42]. An interaction between *C. elegans* UNC-40/DCC and the protein backbone of LON-2/glypican, proposed as a modulator of Netrin-mediated axon guidance, has also been reported[43]. Finally, Netrins can act as short-range or immobilized cues[44–46], where Netrins would need to be immobilized within the growth substrate[47]. Interactions with cell surface proteoglycans or the extracellular matrix can immobilize Netrin and allow for signaling via mechanotransduction and haptotactic responses.

Given clear functional relevance and available structural models, HS binding has been proposed as a mechanism for regulating receptor selection and binding to Netrins[35], although experimental evidence is lacking. It is not clear if the contribution of GAGs is essential for signaling, as the major heparin-binding site of Netrins, the C-terminal NTR domain[48], is not required for guidance activity of UNC-6/Netrin[49] or binding to either DCC/Neogenin or UNC-5[50,51]. As Netrin without the NTR domain might still have some heparin-binding activity, it has been difficult to dissect the roles of GAGs in Netrin signaling via simple domain deletions and truncations.

Finally, the functional roles of HSPGs in axon guidance is not limited to Netrin signaling. For example, HS is known to mediate interactions between other guidance cue-receptor pairs, including Slit and Robo [52], and the LAR class of neuronal receptor tyrosine phosphatases to control neurite outgrowth [53,54]. Heparan sulfate is also shown to interact with classical guidance cues Semaphorins and Ephrins [55].

1.2 Pathfinding: Where straying from the Beaten Path is highly discouraged

1.2.1 Nerve and muscle connection at the neuromuscular junction

The nervous system transmits signals to muscles to efficiently coordinate the body. The neuromuscular junction (NMJ) is a chemical synapse between the presynaptic terminal of a motor neuron and the postsynaptic surface of a muscle cell (**Figure 1.6**). An action potential in the motor neuron triggers the release of neurotransmitters. These neurotransmitters subsequently bind to receptors on the cell surface of the muscle fibers, leading to muscle contraction. To initiate muscle movement, NMJs need to be properly formed and maintained. Lack of NMJ integrity is associated with complete loss of or weakened muscle function[56].

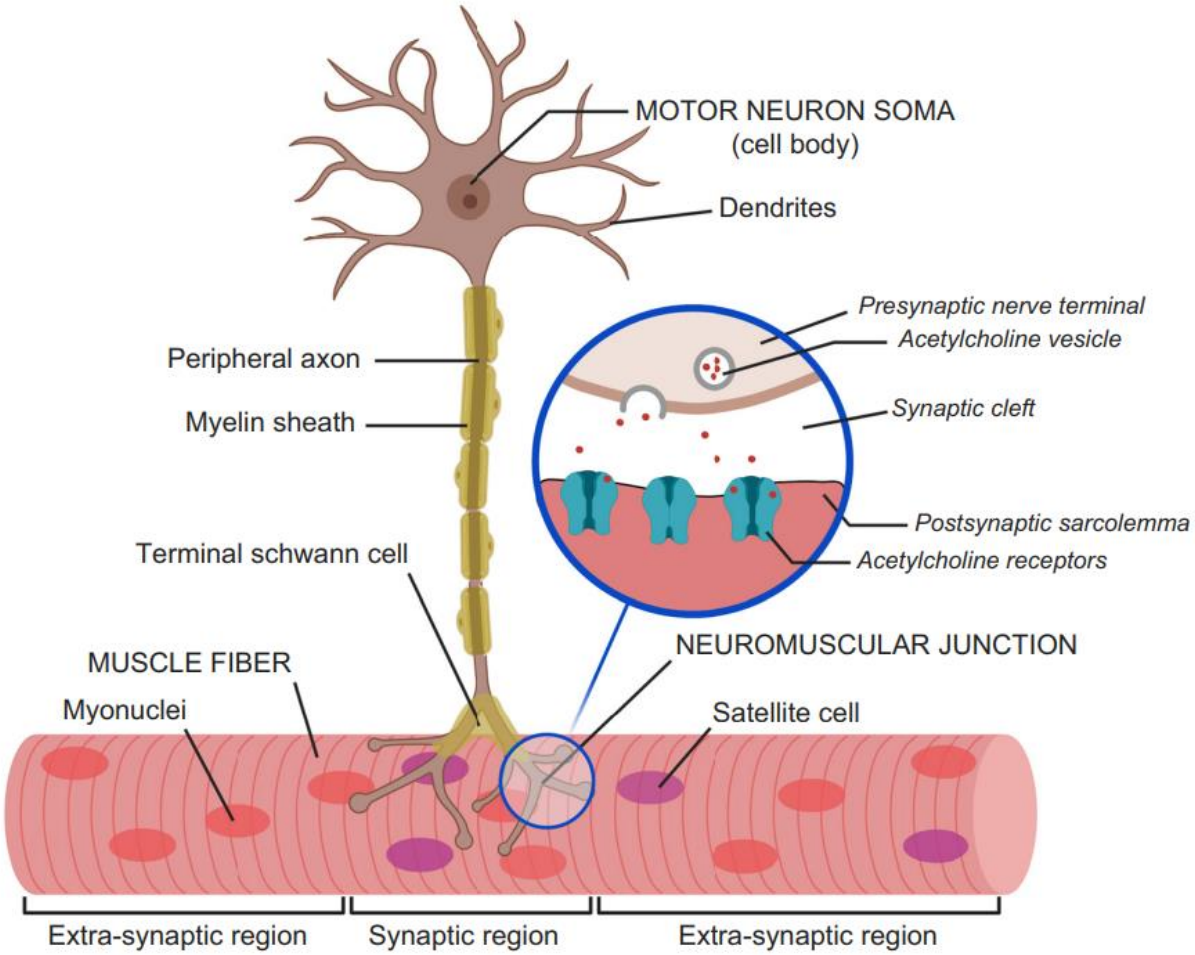

Figure 1.6. Components of a neuromuscular junction (from Soendenbroe et al. 2021).

An NMJ consists of the presynaptic terminal of a motor neuron and the postsynaptic membrane of a muscle cell. An action potential in the neuron causes neurotransmitters to be released from the presynaptic terminal into the synaptic cleft. These neurotransmitters then bind to receptors on the postsynaptic membrane, resulting in muscle contraction. While the diagram shows only one motor neuron and one muscle fiber, in reality, a motor unit comprises all the muscle fibers a neuron innervates.

The neuromuscular transmission pathway is common to most animals. Neurotransmitters include serotonin, histamine, dopamine, acetylcholine, glutamate, and gamma-aminobutyric acid (GABA). *D. melanogaster* and humans use many of the same neurotransmitters despite their long evolutionary history. Within the presynaptic terminal, synaptic vesicles (SVs) contain approximately 10,000 molecules of neurotransmitter each. The amount of neurotransmitter contained in a single SV is referred to as a "quantum." Neuromuscular transmission efficacy

depends on the amount of quanta released, a factor of the contacts between the neuron and muscle[57]. Once an action potential reaches the presynaptic terminal, voltage-gated calcium channels open to further depolarize the terminal, causing SVs to fuse to the membrane and release their contents into the synaptic cleft. Neurotransmitters bind to ligand-gated ion channels on the membrane of the postsynaptic muscle cell. Upon binding, the channels open, allowing for the influx of positive ions, triggering an action potential to propagate along the muscle fiber and leading to muscle contraction.

1.2.2 Cell surface proteins determine how cells interact with one another

Each cell encodes a variety of proteins at the cell surface, creating a unique molecular identity. Cell surface proteins and all the proteins they interact with is known as an interactome. The interactome dictates how cells form connections with one another, relying on their molecular identities to establish highly specific and context-dependent protein-protein interactions (PPIs)[57–60]. Interactomes play roles in adhesion and cell-cell communication.

Over the course of history, evolution significantly expanded protein domain families involved in cell surface PPIs. Despite comprising a substantial portion of all encoded proteins, cell surface proteins lack complete interactome data due to challenges in protein purification and fast binding kinetics. Cell surface PPIs range in affinity from micromolar to picomolar. Weak interactions are difficult to detect due to their low affinity and transient nature[61]. We and others have developed biochemical assays to combat these issues by bypassing the need for protein purification and using avidity effects via oligomerization to increase affinity[62,63].

The Extracellular Interactome Assay (ECIA) is a high-throughput, colorimetric technique to detect low-affinity interactions, inspired by the enzyme-linked immunosorbent assay (ELISA). In this assay, Protein-A-coated plates are used to capture fragment crystallizable protein (Fc)-tagged proteins, the bait. Once the Fc-tagged proteins bind, the plates are incubated with pentameric alkaline phosphatase (AP)-tagged proteins, the prey. AP activity using BluePhos as a substrate allows for prey binding detection as measured by absorbance by the product at 650 nm (**Figure 1.7**)[63].

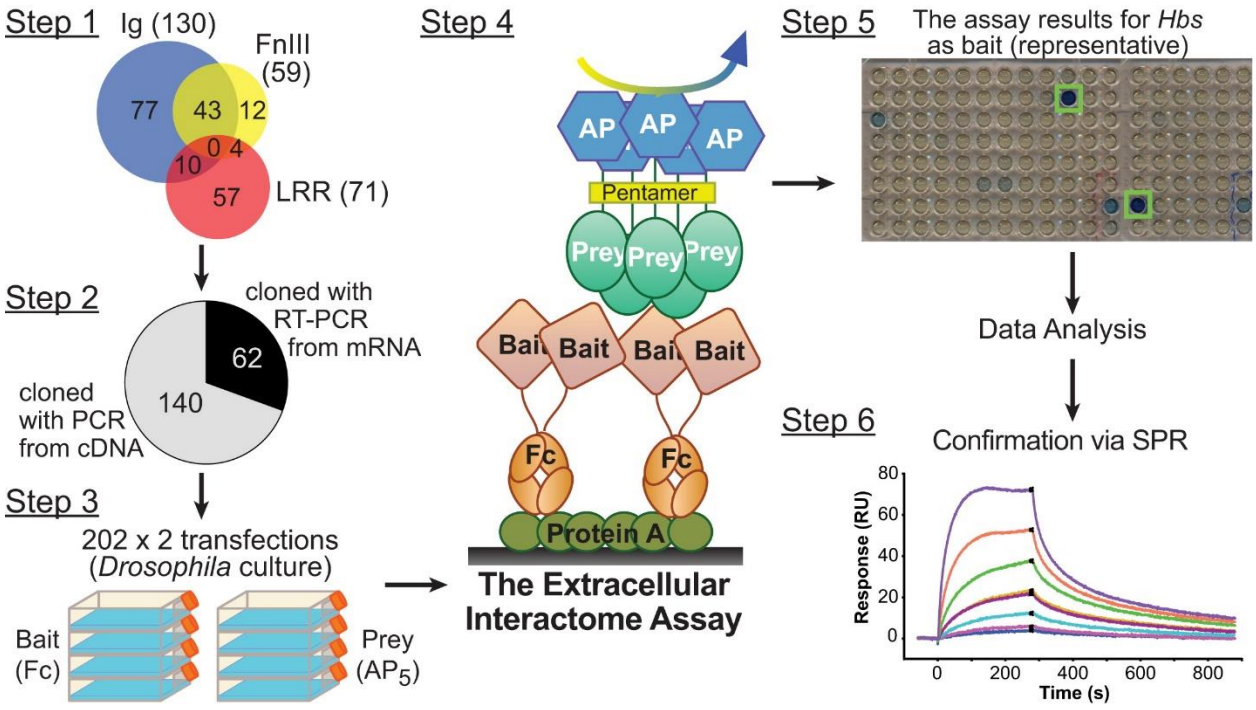

Figure 1.7. Extracellular Interactome Assay protocol (from Özkan et al. 2013).

Fc- and AP-tagged constructs are cloned for expression in insect cells (Steps 1-2). After expression (Step 3), Fc-tagged proteins incubate in a Protein-A-coated plate to bind the bait to the plate. Then, AP-tagged proteins, the prey, incubate with the bait-bound plate (Step 4). Prey binding is monitored via the activity of AP using BluePhos as a substrate, leading to a blue color change (Step 5). Identified PPIs are confirmed with surface plasmon resonance.

The Bio-Plex Interactome Assay (BPIA) uses a similar concept of baits and preys; however, the technique employs multiple baits for one prey. In this assay, baits are AP-tagged while preys are Fc-tagged, the opposite orientation of ECIA. Streptavidin beads, each labeled with a unique bead region to identify the bead, capture biotinylated AP-tagged bait proteins. One prey incubates with multiple bait-coated beads. Primary and secondary antibodies for the prey protein assess binding. A Bio-Plex 200 machine analyzes each bead individually to determine the bait protein and if any prey is bound (**Figure 1.8**)[64].

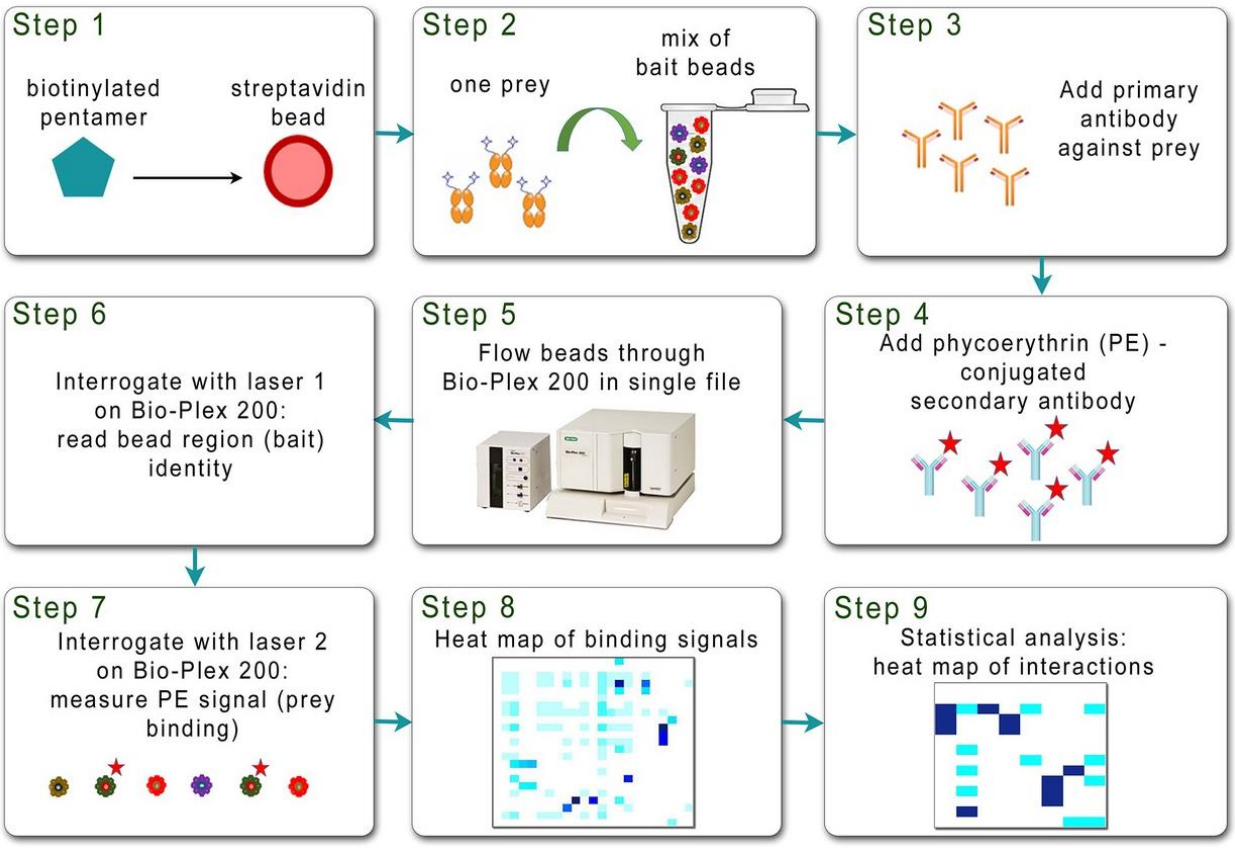

Figure 1.8. Bio-Plex Interactome Assay protocol (from Li et al. 2017).

Continued on next page.

Figure 1.8 continued. Bait fusion proteins contain AP for pentamerization and Avitag for biotinylation. Biotinylated baits bind to streptavidin beads. Each bead has a unique bead region that determines its identity (Step 1). Each Fc-tagged prey incubates with a mixture of bait beads (Step 2). After incubation, primary and secondary phycoerythrin (PE)-conjugated antibodies bind to the preys (Steps 3-4). Each bead flows through a Bio-Plex 200 machine one at a time to analyze the bead region, and therefore its bait protein, and the strength of prey binding through PE signal (Steps 5-7). A heat map summarizes all interactions detected (Steps 8-9).

Cell surface PPIs influence motor axon pathfinding. Motor axons follow specific pathways to reach their muscle targets and establish NMJs. The axons navigate from the spinal cord and extend into the periphery at choice points, innervating the body by sensing the environment and interacting with nearby cells[65]. A pioneer axon is the first axon to leave the CNS and sets the stage for others to follow. Motor axons form bundles during selective fasciculation, effectively establishing a pathway to a target location[66]. The process of fasciculation and defasciculation is under tight regulation during wiring.

1.2.3 Beaten Paths and Sidesteps

Beats and Sides are two families of proteins from the IgSF identified in *D. melanogaster* through genetic screens for motor axon guidance defects[67,68]. The evolutionary origins of both proteins are mysterious. Clear orthologs are present across arthropods, including crustaceans, myriapods and chelicerates, but not beyond in other Ecdysozoans, such as *C. elegans*, or vertebrates[69,70].

In the extracellular region, Beats have two IG domains, while Sides have five IGs followed by one FN3 domain. They are type I membrane proteins with an extracellular N-terminus, single-pass transmembrane helix, and cytosolic C-terminus (**Figure 1.9A**)[71,72]. Beaten Path (now Beat-Ia or Beat) was originally thought to be secreted, but new evidence supports it being membrane bound. Beat-Ia lacking its transmembrane region does not localize to the membrane but retains its ability to bind Sidestep (now Side-I or Side)[73]. While no conserved motifs or domains in their

intracellular regions have been reported for Beats, Sides have one conserved motif: a C-terminal PDZ (named for postsynaptic density protein of 95 kDa, *Drosophila* disc large tumor suppressor, and ZO-1) peptide (**Figure 1.9B**)[64,67]. Beats contain a cysteine-rich region near their C-terminus, similar to a cysteine-knot motif[72], however due to its intracellular localization this is likely a false identification.

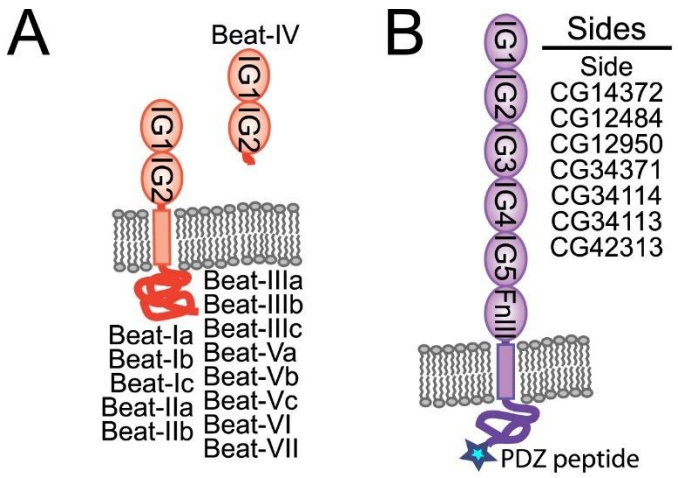

Figure 1.9. Structure of Beats and Sides (from Özkan et al. 2013).

Both Beats and Sides are transmembrane proteins. Certain Beats, such as Beat-Ia and -IV, have been implicated as secreted, although evidence is lacking. **A.** Beats have 2 IG domains extracellularly and an unstructured cytosolic region. **B.** Sides have 5 IG domains followed by a FN3 domain extracellularly and a PDZ peptide in the cytosolic region.

The functions of Beats and Sides in axon guidance in *D. melanogaster* have been incompletely documented. The mutant phenotypes for the founding members of the families, Beat-Ia and Side-I, are similar despite different expression patterns[74,75]. In *D. melanogaster*, approximately 50 motor axons innervate 30 muscle targets. Two motor nerves, the intersegmental nerve (ISN) and the segmental nerve (SN or SNa) exit the CNS. At choice points along these nerves, axons branch off to innervate either dorsal or ventral muscles. The SNb and SNd branch off the ISN to innervate ventral muscles and the SNc branches off the SNa to innervate dorsal muscles (**Figure 1.10A-B**). In *beat* and *side* mutant animals, axons fail to

branch off at these designated choice points, remaining fasciculated or stalling, and do not progress into the periphery (**Figure 1.10C-D**)[74].

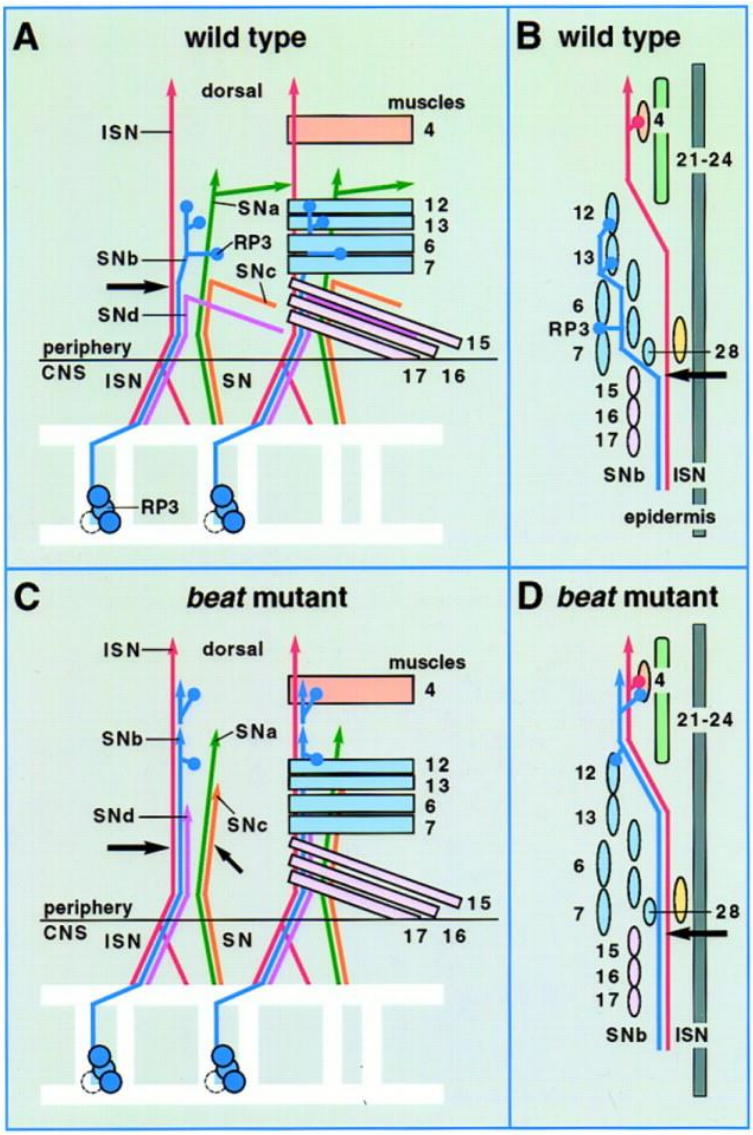

Figure 1.10. Drosophila motor neuron pathways in wild-type and *beat* mutant embryos (from Fambrough and Goodman 1996).

Schematic of two hemisegments, anterior (left) and dorsal (right), of a stage 17 *Drosophila* embryo. Arrows represent choice points for defasciculation in the CNS. **A,B.** In the wild-type embryo, SNb and SNd defasciculate from ISN and SNc defasciculates from SNa. **C,D.** In the *beat* (and *side,* not shown) mutant embryo, the neurons remain fasciculated., failing to branch at the designated choice points.

Motor neurons express Beats while sensory neurons and muscles express Sides. Beat-expressing motor axons selectively defasciculate towards attractive Side-expressing cells[73]. There are 14 Beats and 8 Sides. Some Beats are known to selectively bind to certain Sides. A third of Beats and Sides remain orphans (7 out 21) (**Figure 1.11**), and only Beat-Ia, -Ic, -IV and -Va/b/c interactions have been studied by a quantitative method, such as SPR. The measured affinities are relatively weak and lie in the low μM range[63,64].

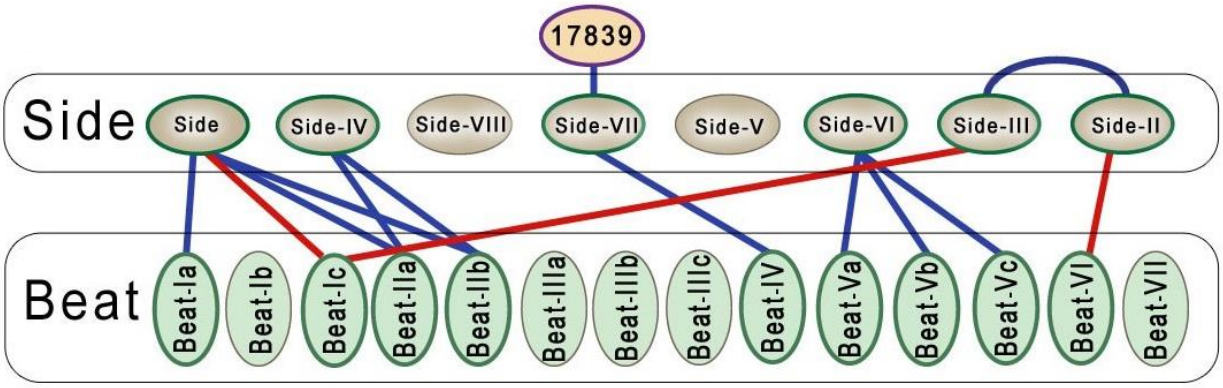

Figure 1.11. Beat-Side interactome map (from Li et al. 2017).

A map of the interactions between Beats and Sides shows interactions discovered using ECIA (blue lines) and BPIA (red lines).

CHAPTER 2: REPULSIVE NETRIN GUIDANCE COMPLEXES

2.1 Introduction

While Netrin's affinity for heparin-like molecules is well established, it is not clear if the receptors interact with GAGs directly [76]. Here we chose to work with *C. elegans* UNC-6/Netrin and UNC-5, the first molecules of their families to be identified, since they have clear axonal guidance and cell migration phenotypes and come with a large body of mutational and functional data. To study UNC-6–UNC-5 interactions and possible roles for heparin in this interaction, we established a yeast display system for UNC-5 and show that the binding between UNC-5 and UNC-6 is strongly enhanced when heparin is added. Through directed evolution of UNC-5 displayed on yeast, we have identified and engineered the UNC-5 interface used for heparin binding, and we confirmed heparin binding to this surface with a crystal structure of a complex formed between UNC-5 and a short form of heparin. Addition of heparin allows for the formation of the UNC-6–UNC-5 ectodomain complex with a surprisingly rigid and globular structure, which mostly excludes the attractive receptor, UNC-40. Importantly, we have shown that abolition of heparin affinity of UNC-5 in *C. elegans* results in cell migration defects associated with loss of function of *unc-5* and *unc-6*, indicating mechanistic dependence of Netrin:UNC-5-mediated guidance on HS. Finally, we show that the mammalian Netrin-1–UNC5B complex is also strongly enhanced by HS, which competes with DCC binding to favor Unc5B binding, demonstrating conservation between the nematode and mammalian systems. Our results provide detailed biochemical and functional insights into repulsive Netrin complexes and may be crucial in explaining chemo- and haptotactic responses to Netrin sources.

2.2 Results

2.2.1 High-affinity UNC-6–UNC-5 binding depends on heparin

The interactions of UNC-6/Netrins with their attractive receptors, DCC and Neogenin, have been heavily characterized using structural and mutational studies [77,78]. However, structural data for Netrin interactions with its repulsive receptor, UNC-5, remain sparse, likely due to the low affinity for this ligand-receptor pair. To study UNC-6/Netrin–UNC-5 interactions, we established a yeast surface display system as a platform to measure and engineer this interaction, which also enabled us to investigate the effects of additional molecular players, most importantly GAGs. Briefly, we displayed on yeast cells the ectodomain of *C. elegans* UNC-5, including its two IG and two Thrombospondin type I (Tsp1) domains, by way of a fusion to the yeast cell wall protein, Aga2 (**Figure 2.1A**). UNC-5 is expressed on yeast cells as evident from antibody staining of the C-terminal myc tag.

To measure UNC-6/Netrin binding to UNC-5-expressing cells, we expressed and purified a soluble construct of *C. elegans* UNC-6 lacking its C-terminal NTR domain (UNC-6ΔC), since the NTR domain is known to limit solubility [50] and is dispensable for much of its function. We created a yeast-staining reagent by biotinylating UNC-6ΔC (**Figure 2.2A**) and incubating it with Alexa Fluor 647-coupled streptavidin. In the absence of heparin, UNC-6ΔC binds very weakly to UNC-5-displaying yeast, as measured with flow cytometry by the weak fluorescence shift relative to the negative control yeast (**Figure 2.1B red**). To test if the interaction can be improved by GAGs, we added heparin (from porcine intestinal mucosa, ~16 kilodalton [kDa]) and UNC-6ΔC on UNC-5-expressing yeast, which showed strong UNC-6 binding (right shift of the fluorescence histogram) with an apparent K_D of 35 nM in the presence of 5 μg/ml (0.31 μM) heparin (**Figure 2.1A right**, **1B green,** and **Figure 2.2C**). This demonstrates that strong UNC-6–

UNC-5 binding may require heparin, likely in the form of a HSPG on the growth cone or the substrate tissue *in vivo*.

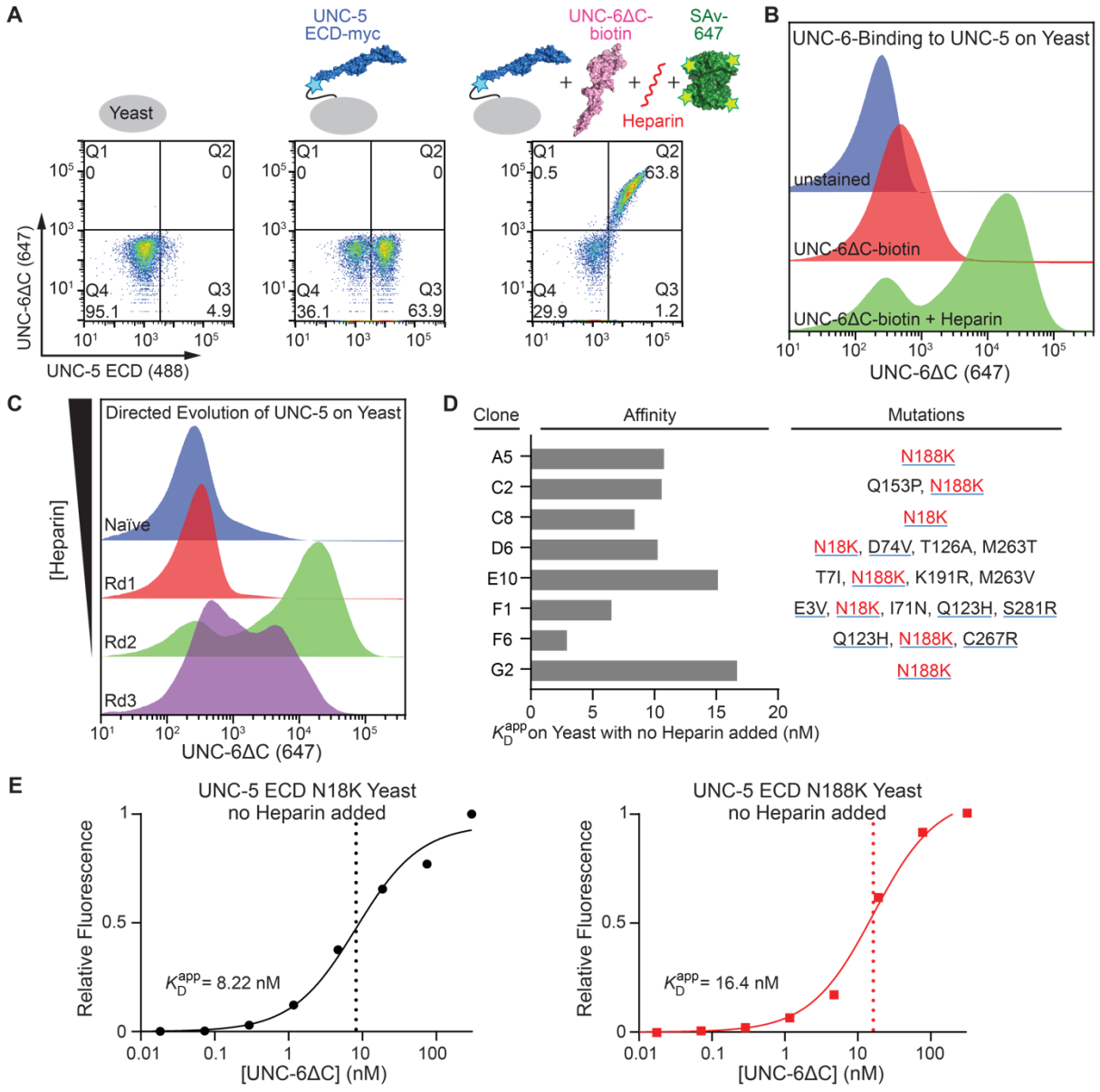

Figure 2.1. UNC-6 binding and directed evolution of UNC-5 ectodomain on yeast.

Continued on next page.

Figure 2.1 continued. A. UNC-5 extracellular domain (ECD) displays on yeast, as detected by anti-myc staining (Alexa 488), and strongly interacts with biotinylated UNC-6ΔC monomers bound to Alexa 647-coupled Streptavidin in the presence of heparin. (*Left*) Unstained cells, (*Middle*) Cells stained with anti-myc antibody, (*Right*) Cells double-stained with anti-myc and UNC-6ΔC–streptavidin with 5 μg/ml heparin added. **B.** Histograms for Alexa 647 fluorescence of unstained cells (blue), UNC-6ΔC-stained cells (red), and UNC-6ΔC-stained cells in the presence of 5 μg/ml heparin (green). UNC-6ΔC-stained cells were incubated with 1μM UNC-6ΔC. **C.** Histograms of bulk UNC-6ΔC labeling of the yeast library displaying randomly mutated UNC-5 ECD variants, including naïve library (blue), and resulting libraries during three rounds of selections, where heparin concentration was decreased. The final round of selection contained no added heparin. **D.** Apparent UNC-6ΔC-binding affinities for the selected UNC-5 variants on yeast. All binding isotherms are shown in **Figure 2.2C**. Mutations increasing net positive charge on UNC-5 ECD are underlined blue; no mutation in the selected colonies added net negative charge. Data were collected in the absence of added heparin. **E.** Binding isotherms repeated for two single-site mutants of UNC-5 ECD, N18K and N188K, interacting with UNC-6ΔC in the absence of added heparin.

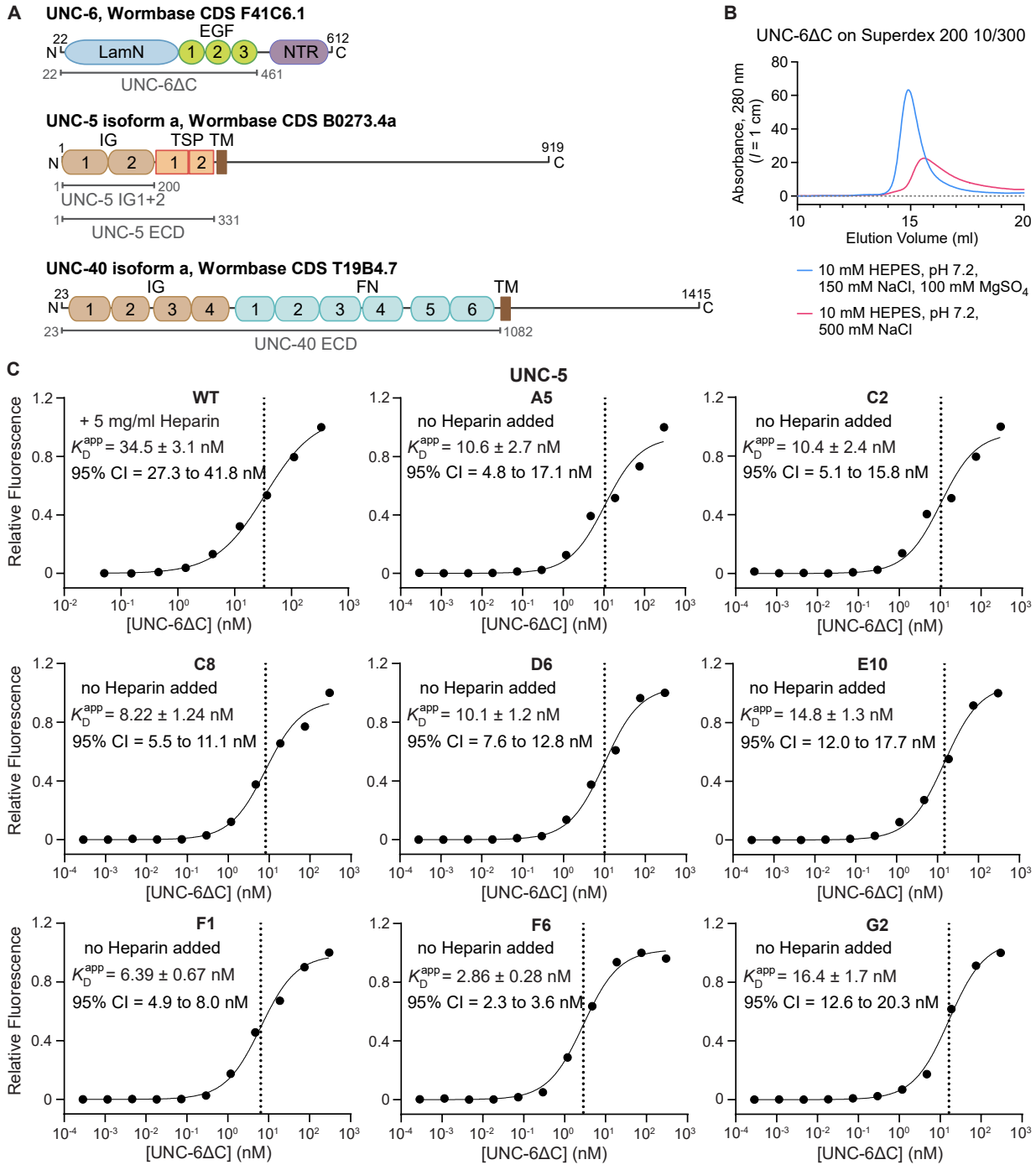

Figure 2.2. Binding isotherms for UNC-5 ECD-expressing yeast.

Continued on next page.

Figure 2.2 continued. A. Schematic for boundaries of constructs used for binding studies, crystallography, biophysics and directed evolution. **B.** Size-exclusion chromatograms of hexahistidine-tagged UNC-6ΔC run in HBS (red), HBS containing 500 mM NaCl (blue), and HBS-MS (green). The column is a Superdex 200 10/300 (GE Healthcare). 100 µg was loaded in both runs: The run with HBS-MS buffer recovered 89.8 µg as measured by the area under the peak (76.11 mAU×ml), while the run with high-NaCl HBS showed stronger signs of non-specific stickiness to the resin, allowing for 66.4 µg to be recovered (area = 56.25 mAU×ml). Abs-0.1% value (absorbance at 1 mg/ml) used for UNC-6ΔC is 0.845. AU stands for arbitrary unit. **C.** Binding isotherms for UNC-6ΔC to yeast expressing WT UNC-5 ECD in the presence of 5 µg/ml heparin and to eight yeast colonies expressing UNC-5 ECD variants without added heparin. Both standard errors of the non-linear fitting and the 95% confidence intervals (CI) for apparent dissociation constants are reported.

2.2.2 Directed evolution of heparin dependence of UNC-6–UNC-5 binding

We hypothesized that we can modulate UNC-5 dependence on heparin for UNC-6 binding using directed evolution. We created an UNC-5 ectodomain display library using random error-prone PCR and selected for UNC-6ΔC binding while decreasing heparin concentrations in the staining solution (**Figure 2.1C**). The third and final round of selections was performed in the absence of added heparin and therefore shows a slight reduction in binding compared to the previous round. We were able to evolve high-affinity UNC-6 binding as seen in titrations on yeast (**Figure 2.1D** and **Figure 2.2C**). Sequencing of eight clones from the third round of selection shows that every clone included either an N18K or an N188K mutation (**Figure 2.1D**). As these mutations increase net positive charge on UNC-5, we predicted that we had increased UNC-5 affinity to heparin, in addition to strengthening binding to UNC-6. Since we could observe strong UNC-6 binding with these mutants even in the absence of added heparin, binding might be supported by an endogenous, unknown GAG-like molecule on the yeast surface.

To confirm that the two mutations identified are the cause for increased UNC-6ΔC binding in yeast display experiments, we performed titrations of UNC-6ΔC binding to UNC-5 N18K/N188K ectodomain on yeast in the absence of added heparin (**Figure 2.1E**). Apparent

binding affinities of UNC-6ΔC to UNC-5 N18K and N188K-expressing yeast were relatively strong and in the nanomolar range, 8.2 and 16.4 nM, respectively.

2.2.3 UNC-5 binds heparin via a positively charged patch at the boundary of its IG1 and IG2 domains

To gain more insights into UNC-5 interactions with heparin and/or UNC-6, we set out to determine the structure of the *C. elegans* UNC-5 ectodomain. Crystallization was successful for a construct containing the two IG domains, which included both N18 (IG1) and N188 (IG2) identified in directed evolution experiments. Using these crystals, we determined the structure of the two-IG domain UNC-5 construct to 2.9 Å resolution (**Figure 2.3A**). The structures of the IG domains show no major differences to previously determined human Unc5A, rat Unc5D [79,80] and mouse Unc5B crystal structures [81], including a buried disulfide bond linking UNC-5 Cys37 (C strand) and Cys84 (F strand) in IG1 in addition to the canonical disulfide bond found in IG domains, and a short α-helix connecting E and F strands in IG1. Similarly, the IG2 domain is N-glycosylated at a remarkably conserved site, Asn178 (F strand), also observed in the rat Unc5D and mouse Unc5B structures; no glycosylation on IG1 is observed. We also had the opportunity to compare flexibility at the IG1-IG2 boundary: An alignment of our UNC-5 IG1+2 structure with three vertebrate UNC5 structures show wide variability of the angle between the IG1 and IG2 domains (**Figure 2.4A**). Flexibility at this position may be necessary for recognition by HS as well as protein ligands, since our directed evolution results indicate this region (containing Asn18 and Asn188) as a site of HS binding, and this is also the binding site for Latrophilins [80].

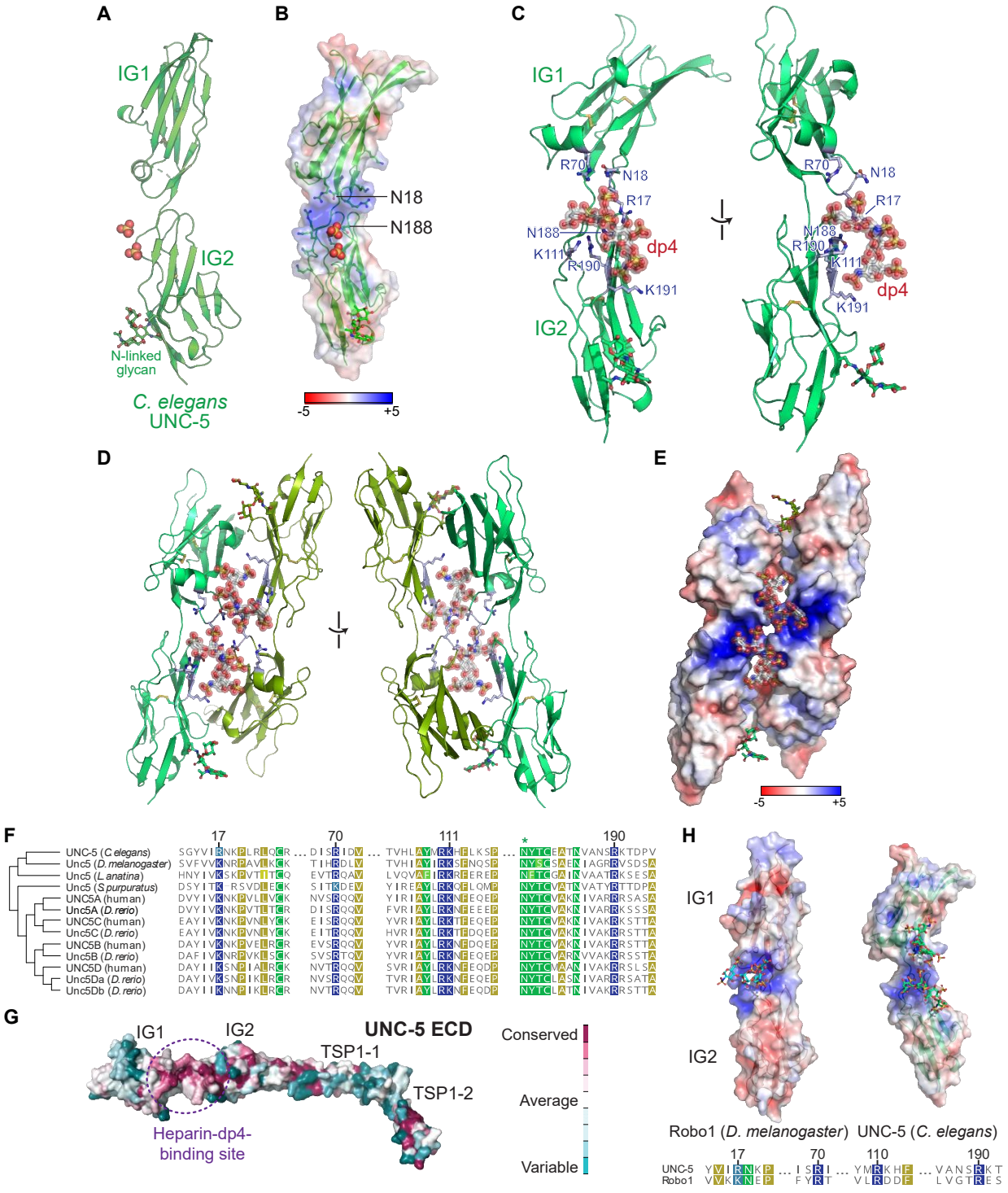

Figure 2.3. Crystal structures of UNC-5 IG1-2 highlight a positively charged surface used for heparan sulfate binding.

Continued on next page.

Figure 2.3 continued. A. UNC-5 IG1-2 structure with putative sulfates bound near the IG1-IG2 boundary. The conserved N-linked glycan at N178 is shown in ball-and-stick representation. **B.** Electrostatic potential surface for the UNC-5 IG1-2 structure, showing a positively charged surface at the IG1-IG2 boundary. The range of electrostatic potential used to color the surface is from -5 to +5 *kT*/*e*. The two Asn residues identified in directed evolution experiments are labeled. **C.** Crystal structure of the UNC-5 IG1-2 domains bound to the heparin tetrasaccharide (dp4); one alternate conformation is displayed. For a detailed view, see **Figure 2.4E-F**. **D.** The asymmetric unit of the UNC-5+dp4 crystal structure, showing a possible dimer created by a dp4 molecule, built as two alternate conformations into density (**Figure 2.4B-D**). The two alternate conformations overlap with two alternates of a dp4 molecule from the neighboring asymmetric unit, creating an intimate four-molecule UNC-5 entity, as seen in **Figure 2.4D**. **E.** Surface potential of the dimer shows a contiguous positive surface, which is used for binding to HS. **F.** The positively charged patch at the UNC-5 IG1-IG2 boundary is conserved. Alignment of protostome and deuterostome UNC-5 sequences show the positive charge at the IG1-IG2 boundary to be highly conserved. Sequence numbering above follows the *C. elegans* UNC-5 sequence. **G.** Surface conservation analysis by ConSurf of the full ectodomain of UNC-5 (using the AlphaFold2 model) shows the IG1-IG2 boundary to be largest conserved surface patch. **H.** *Top.* Side-by-side views of the *C. elegans* UNC-5 IG1-2+dp4 structure and fruit fly Robo1 IG1-2+dp8 structure (Protein Data Bank [PDB] ID: 2VRA; only a tetrasaccharide is visible), with surface electrostatic potentials. *Bottom.* Sequence alignment of the UNC-5 and Robo1 IG1-2 domain contacts, showing that the positively charged patch at the IG1-IG2 boundary are common to both receptors.

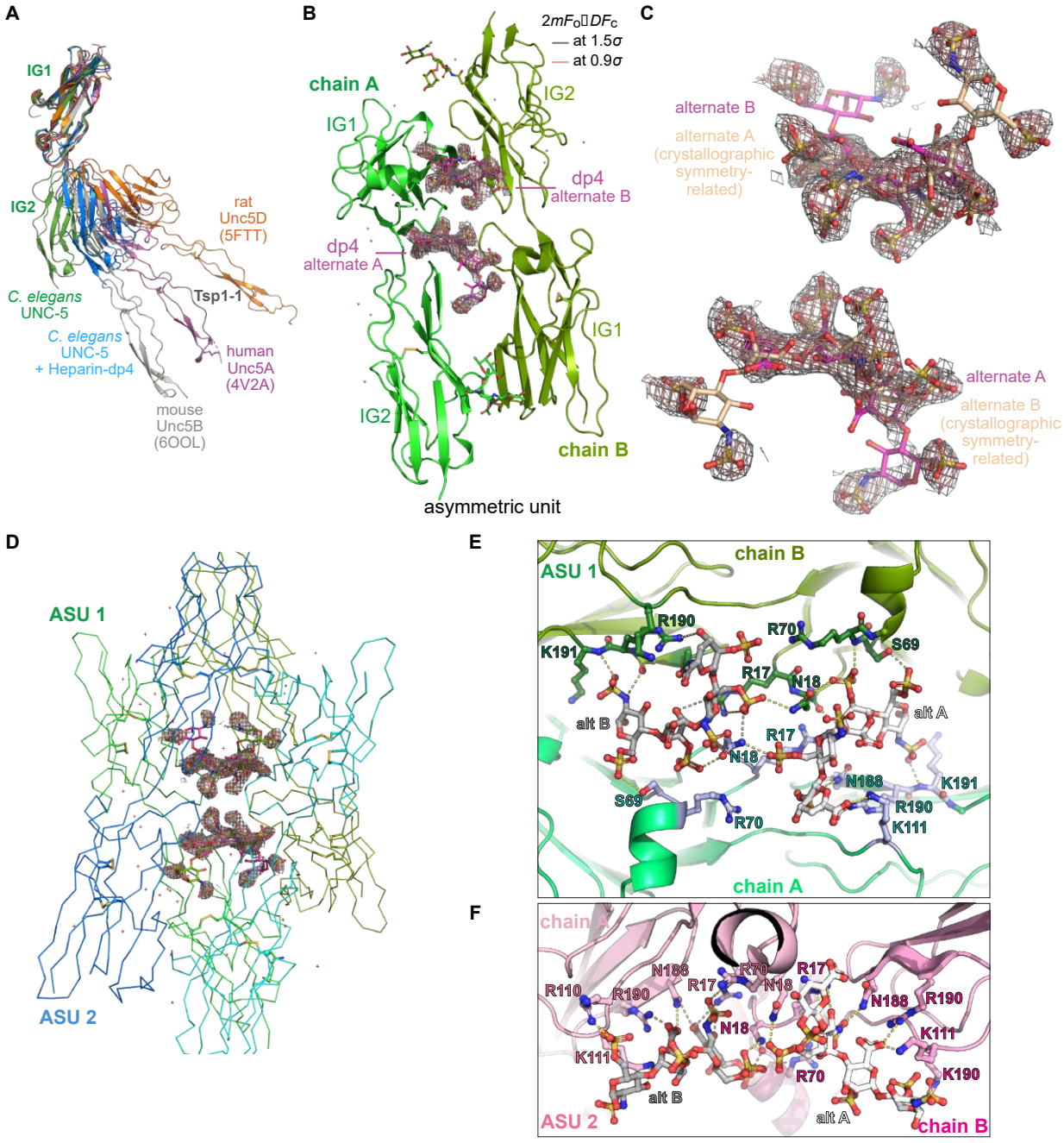

Figure 2.4. The asymmetric unit of UNC-5 IG1+2 with heparin-dp4 crystals.

Continued on next page.

Figure 2.4 continued. A. Superposition of reported UNC-5 structures in the literature and our UNC-5 IG1-2 structures, where the IG1 domains are overlayed, demonstrating wide flexibility of the IG1-IG2 boundary. **B.** The asymmetric unit of the UNC-5-dp4 crystals, with 2mFo-DFc density carved around the dp4 ligand. Heparin-dp4 was modeled as two alternate conformations in equivalent positions of the two UNC-5 chains related by non-crystallographic symmetry (light and dark green). **C.** Electron density for heparin-dp4 with dp4 from two neighboring asymmetric units shown (colored magenta and salmon), each with two alternate copies. Density is strongest at the electron-rich sulfates. **D.** Electron density for dp4 surrounded by four UNC-5 chains, contributed by two asymmetric units. **E.** Close look at non-covalent interactions between dp4 molecules in both alternate conformations (alt A [white] and alt B [gray]) to two chains of UNC-5 in one asymmetric unit (ASU 1). Yellow and orange dashed lines are for polar interactions at ≤3.5 Å and 3.5 to 4 Å, respectively. **F.** Interactions of the same molecules to two UNC-5 chains in the next asymmetric unit (ASU 2).

	C. elegans UNC-5 IG1+2	*C. elegans* UNC-5 IG1+2 with Heparin-dp4	*C. elegans* UNC-6ΔC
Data Collection			
Beamline	ALS 8.2.1	APS 23-ID-B	APS 24-ID-E
Wavelength (Å)	0.9795	1.0332	0.9792
Space Group	*C*222	$P6_122$	$P4_12_12$
Cell Dimensions			
a, *b*, *c* (Å)	41.282, 130.216, 97.549	69.46, 69.46, 424.99	70.243, 70.243, 287.353
α, *β*, *γ* (°)	90, 90, 90	90, 90, 120	90, 90, 90
Resolution (Å)	50-2.89 (3.07-2.89)*	50-2.11 (2.30-2.11)†	200-2.5
R_{sym} (%)	10.4 (85.5)	5.9 (166)	8.7 (216)
$<I>/<\sigma(I)>$	14.6 (1.9)	27.0 (2.0)	19.4 (1.3)
$CC_{1/2}$	0.997 (0.722)	0.999 (0.724)	0.999 (0.700)
Completeness (%) (spherical)	98.6 (92.8)	58.0 (12.8)†	98.8 (98.3)
(ellipsoidal)	N/A	94.4 (82.2)†	N/A
Redundancy	5.1 (4.3)	18.4 (14.8)	13.1 (13.7)
Refinement			
Resolution (Å)	50-2.89 (3.18-2.89)*	50-2.11 (2.20-2.11)	68.23-2.50 (2.60-2.50)
Reflections	6,109	21,299	25748
R_{cryst} (%)	24.59 (37.84)	24.02 (37.42)	22.00 (46.45)
R_{free} (%)**	28.51 (42.57)	27.23 (53.73)	25.88 (55.15)
Number of atoms			
Protein	1511	3090	3188
Ligand/Glycans	48	216	95
Water	0	18	31
Average B-factors (Å²)			
All	73.0	68.1	88.7
Protein	72.1	67.5	88.1
Ligand/Glycans	102.1	78.8	117.6
Solvent	N/A	52.6	67.3
R.m.s. deviations from ideality			
Bond Lengths (Å)	0.002	0.010	0.008
Bond Angles (°)	0.418	1.178	0.899
Ramachandran plot			
Favored (%)	97.42	95.71	95.57
Outliers (%)	0.00	0.00	0.00
Rotamer Outliers (%)	0.00	0.29	0.84
All-atom Clashscore‡	4.58	7.15	4.24

* The values in parentheses are for reflections in the highest resolution bin.

** 10% of reflections (613) for UNC-5 IG1+2**,** 5% of reflections (1,065) for UNC-5 IG1+2 with dp4, and 5% of reflections (1,297) for UNC-6ΔC were not used during refinement for cross validation purposes.

† Diffraction limits (Å) and corresponding principal axes of the ellipsoid fitted to the diffraction cut-off surface as direction cosines in the orthogonal basis (standard PDB convention), and in terms of reciprocal unit-cell vectors, are:

Diffraction limit #1:	2.817 Å	(1.0000, 0.0000, 0.0000)	(0.894 **a*** - 0.447 **b***)
Diffraction limit #2:	2.817 Å	(0.0000, 1.0000, 0.0000)	**b***
Diffraction limit #3:	1.944 Å	(0.0000, 0.0000, 1.0000)	**c***

Eigenvalues of overall anisotropy tensor on |F|s (Å^2) and corresponding eigenvectors of the overall anisotropy tensor as direction cosines in the orthogonal basis (standard PDB convention), and in terms of reciprocal unit-cell vectors:

Eigenvalue #1:	122.92	(1.0000, 0.0000, 0.0000)	(0.894 **a*** - 0.447 **b***)
Eigenvalue #2:	122.92	(0.0000, 1.0000, 0.0000)	**b***
Eigenvalue #3:	57.89	(0.0000, 0.0000, 1.0000)	**c***

‡ Clashscores were calculated by phenix.refine (PHENIX version 1.20).

Table 2.1. Data and refinement statistics for x-ray crystallography.

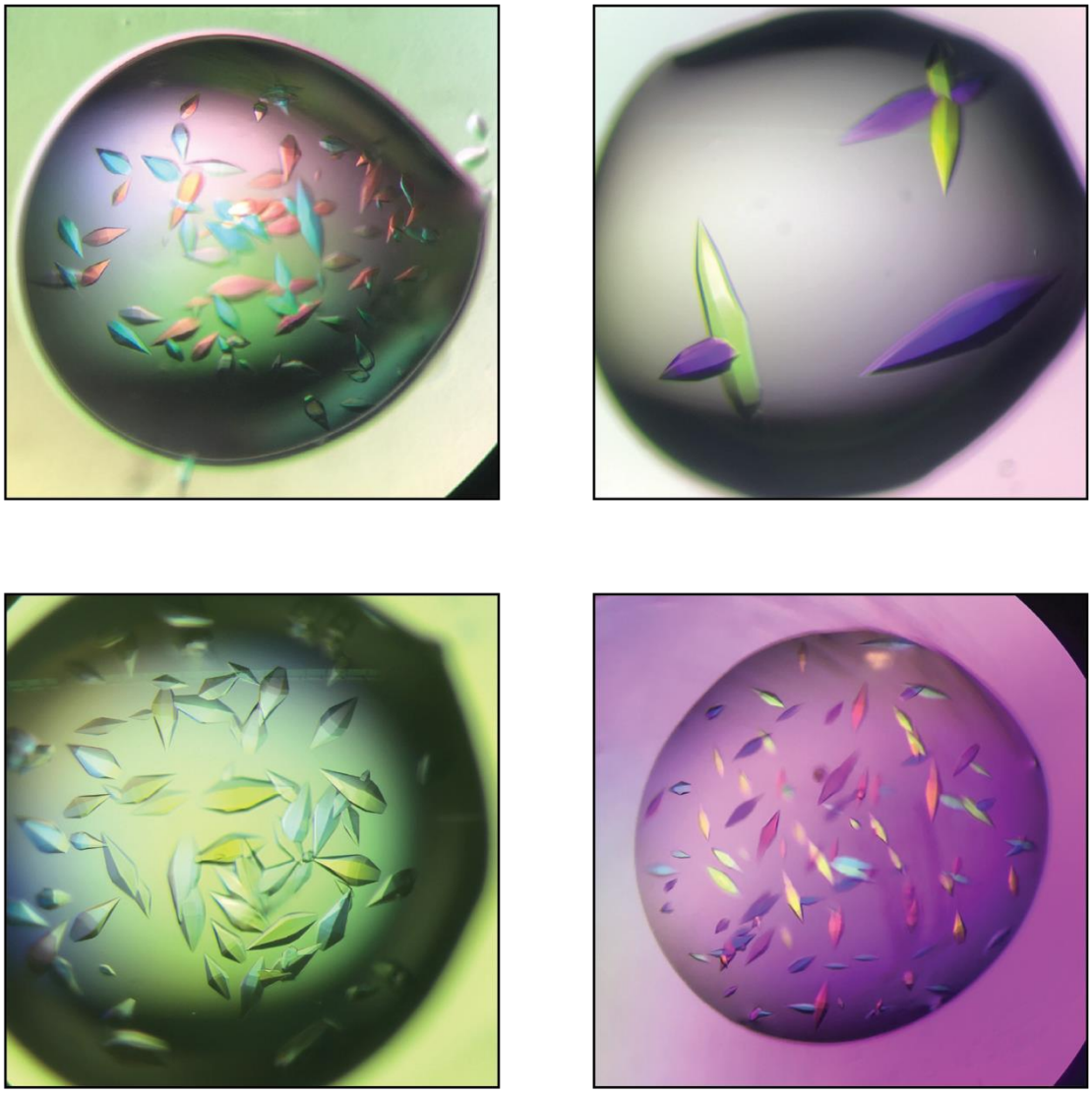

Figure 2.5. Crystallization droplets of UNC-5 IG1+2 with heparin-dp4.

Representative images of crystallization droplets. Coloring is due to the use of polarized light.

Interestingly, there was unexplained electron density surrounding the IG1-IG2 boundary (**Figure 2.4B-C**). Based on the presence of ammonium and lithium sulfate in the crystallization solution and the chemistry around the unexplained density, we believe that there may be two or more fully or partially occupied sulfate ions at this site. Surface electrostatic potential of our UNC-5 structure shows an intensely positive region at this domain boundary created by multiple

arginines and lysines (**Figure 2.3B**). Furthermore, the two N→K mutations selected in our directed evolution experiments fall in this region interspersed between the positively charged arginines and lysines. Overall, this site is a strong candidate for HS binding.

We next crystallized and determined the structure of UNC-5 IG1+2 domains in the presence of a short heparin oligomer limited to four saccharide units, dp4, in a different crystal form (**Figure 2.5**). We observed strong extra density resembling an oligosaccharide oligomer in the same region, surrounded by Arg 17, 70 and 190, Lys 111 and 191, and Asn 18 and 188 (**Figure 2.3C** and **Figure 2.4E-F**).

The UNC-5–heparin-dp4 crystals have an UNC-5 dimer in the asymmetric unit created by 1210 $Å^2$ of buried surface area, which appears to be held together partly by heparin interacting with both chains (**Figure 2.3D**). While the extra density for heparin is strong, there is some ambiguity in the exact orientation of the dp4 ligand, including the glycan residue register and direction: As our best interpretation of density, we chose to model dp4 in two alternate conformations in equivalent positions within this dimer, which then overlap with their alternate conformations from the neighboring asymmetric unit's dp4 molecules (**Figure 2.4C,E-F**). An intimate tetramer, held together by and surrounding heparin molecules, is observed upon investigation of neighboring asymmetric units, where protein-protein contacts bury 1310 $Å^2$ and 1120 $Å^2$ between UNC-5 chains related by crystallographic symmetry (**Figure 2.4D**). While these molecular interfaces may be physiological in the context of a heparin-mediated UNC-5 or UNC-6–UNC-5 oligomer, we do not yet have evidence to support such a model.

2.2.4 The IG–heparin interaction observed in the UNC-5–heparin complex may be a common feature of IG-superfamily receptors

Due to its sulfation and negative charge, heparin binding strongly favors positively charged surfaces on proteins. As a strongly positively charged protein, UNC-6 (pI = 8.7) binding to heparin is not surprising. However, UNC-5 ectodomain has a pI of 5.7, and a net predicted charge of −8 at pH 7. The heparin–UNC-5 interactions are a result of local charge at the IG1-IG2 boundary as observed in our crystal structure (**Figure 2.3E**). The positively charged amino acids that create the HS-binding site in nematode UNC-5 are conserved across all major bilaterian taxa (**Figure 2.3F** and **Figure 2.6**) and make up the major large patch of conserved surface in UNC-5 ectodomains (**Figure 2.3G**).

Since heparin has been implicated in binding to several neuronal adhesion and signaling receptors, including other IgSF proteins, we looked for structural clues in other IG-type receptors with heparin binding. Robo receptors, which are also repulsive guidance receptors, bind heparin using the same surface at their IG1-IG2 boundary (**Figure 2.3H**) [82], suggesting a conserved or convergent site for heparin interactions among IgSF neuronal receptors for heparin binding, although the exact binding poses of the heparin molecules may vary for different heparin-binding proteins.

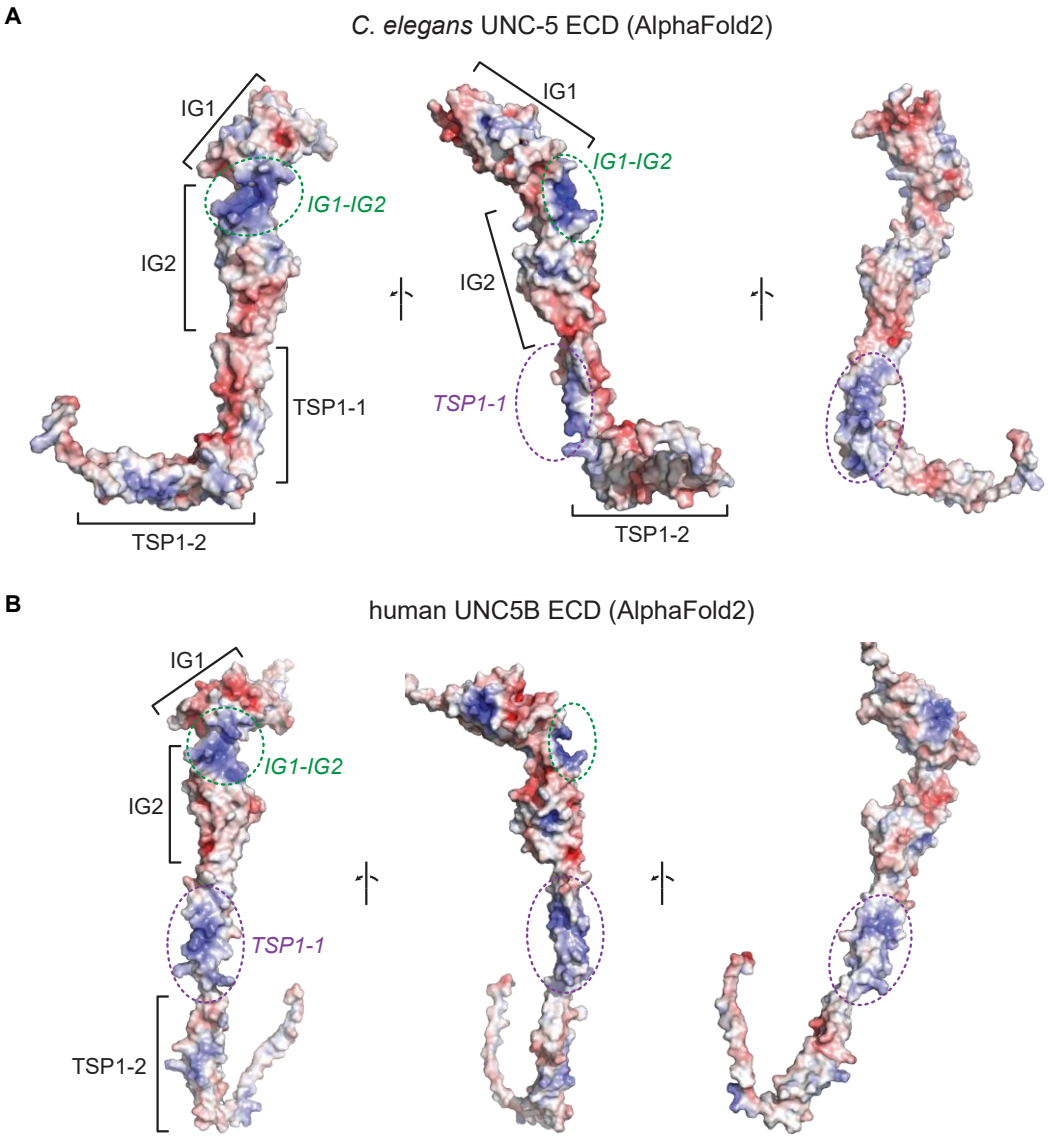

Figure 2.6. AlphaFold structural models for entire ectodomains of *C. elegans* UNC-5 and human UNC5B.

A, B. Electrostatic potential surfaces for *C. elegans* UNC-5 (**A**), and human UNC5B (**B**). Structural models for the entire ectodomains were taken from EBI's AlphaFold database. Both show positively charged surfaces on the IG1-IG2 boundary and on the first Tsp1 domain; however, the IG1-IG2 boundary is more conserved (**Figure 2.4G**).

2.2.5 Biochemical characterization of UNC-5 mutants selected by directed evolution and rational design

Through directed evolution and structural biology, we have identified a positively charged surface at the UNC-5 IG1-IG2 boundary, which interacts with heparin, and could be mutated to increase UNC-6 affinity. To confirm and extend these findings using orthogonal methods, we performed surface plasmon resonance (SPR) experiments with UNC-5 mutants for binding heparin and/or UNC-6. First, we showed that UNC-6–UNC-5 binding is weak with a K_D of ~46 μM as measured using biotinylated UNC-6ΔC captured on an SPR chip (**Figure 2.7A** and **Figure 2.8A**). The N18K and N188K mutations on UNC-5 improve binding to UNC-6, confirming the results of our directed evolution experiments (**Figure 2.7A** and **Figure 2.8A**). Next, we confirmed that UNC-5 binds heparin separately via SPR (**Figure 2.7C** and **Figure 2.8D**). The UNC-5 N18K and N188K mutations, which are at the heparin binding site according to our crystal structure, improve heparin binding as expected, with the double N→K UNC-5 mutant binding heparin with a 16-fold increase in affinity (K_D, 26 vs. 1.7 μM) (**Figure 2.7C** and **Figure 2.8D-E**). We also observed that UNC-6ΔC binds heparin with much higher affinity (K_D = 0.04 μM) (**Figure 2.7D** and **Figure 2.8F**).

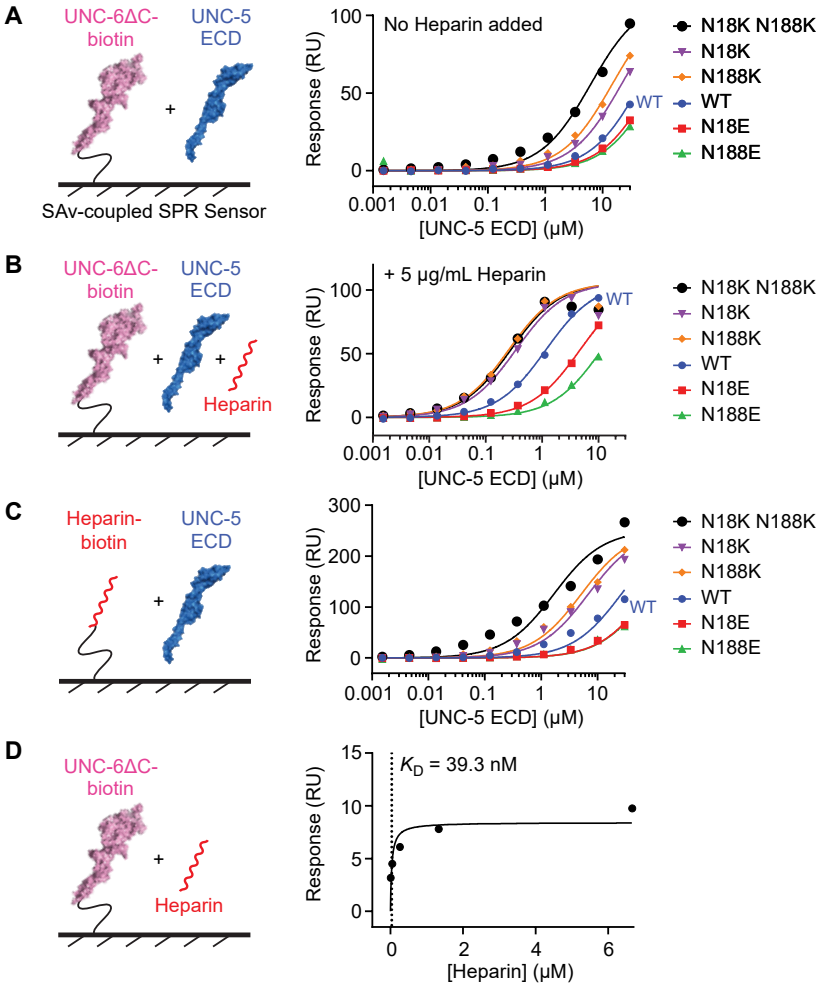

Figure 2.7. UNC-5 mutations at N18 and N188 modulate UNC-5 affinity to UNC-6 and heparin.

A, B. Experimental design and binding isotherms for SPR experiments testing the interaction of biotinylated WT UNC-6ΔC with UNC-5 ECD WT and mutants without added heparin (A), and in the presence of 5 μg/ml heparin (B), where all UNC-5 variants (including WT) were run on the same SPR chip channel containing UNC-6ΔC within one experiment. Since many variants have very weak binding by design, we used the maximum saturation response values fit to the highest-affinity variant within each experiment as a constraint for fitting the lower-affinity variants. **C.** Experimental design and binding isotherms for SPR experiments testing the interaction of biotinylated heparin with UNC-5 ECD WT and mutants, where all UNC-5 variants were run over a single heparin channel within one experiment. In all panels, N→K mutants increase affinity (left shift in the isotherms), while N→E decrease affinity. **D.** Experimental design and binding isotherm for SPR experiment testing the interaction of biotinylated WT UNC-6ΔC with heparin. We measured UNC-6ΔC–heparin affinity with UNC-6 captured on the chip, since soluble UNC-6ΔC can best be used with a buffer containing $MgSO_4$ (see **Figure 2.2B** and Methods), which partly interferes with heparin binding. All sensorgrams for **Figure 2.7** are shown in **Figure 2.8**, and K_D's are tabulated in **Table 2.2**.

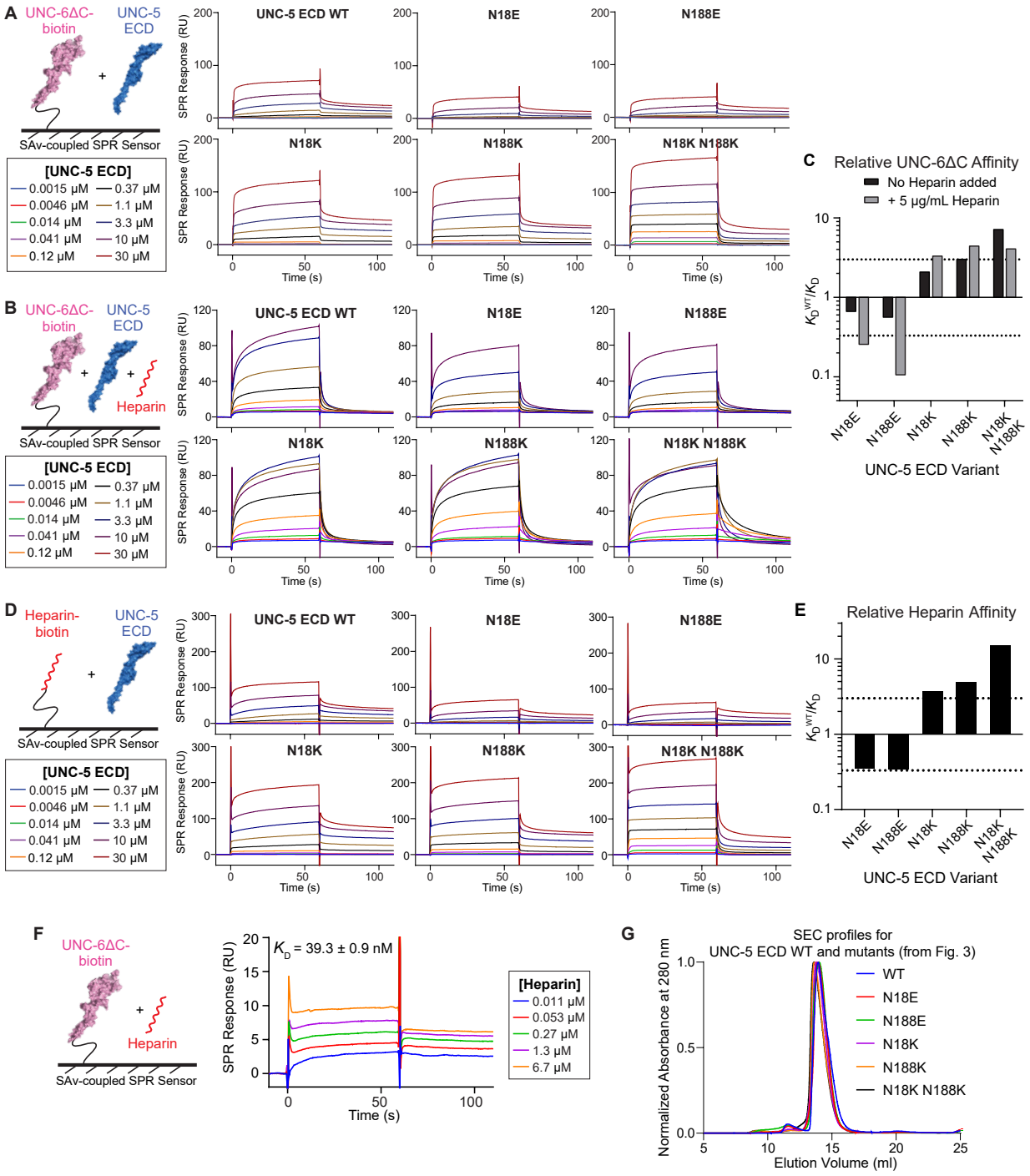

Figure 2.8. SPR sensorgrams for isotherms reported in Figure 2.7.

A,B,D,F. Same channel on the SPR chip was used within each panel, allowing for direct comparison of response values between mutants. **C,E.** Loss or gain of UNC-6ΔC (C) or heparin (E) affinity for N18/N118 mutants of UNC-5 ECD, summarized as ratios of WT K_D to mutant K_D. **G.** SEC profiles for wild-type and N18/N188 mutants of UNC-5 ECD measured during purification over a Superdex 200 10/300 column.

Experimental Design	UNC-5 ECD variant	K_D (μM)	Standard error of the fit (μM)	K_D^{WT}/K_D
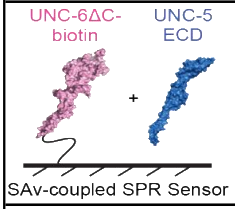	Wild-type	45.7*	1.4	1.00
	N18E	70.9*	1.5	0.645
	N188E	83.7*	7.5	0.546
	N18K	21.3*	1.0	2.15
	N188K	14.7*	0.8	3.12
	N18K N188K	6.20	0.56	7.38
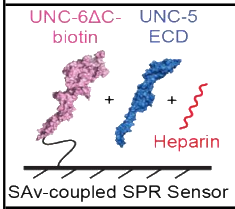	Wild-type	1.17	0.05	1.00
	N18E	4.70*	0.12	0.248
	N188E	11.3*	0.5	0.103
	N18K	0.341*	0.069	3.41
	N188K	0.255*	0.038	4.57
	N18K N188K	0.277*	0.053	4.21
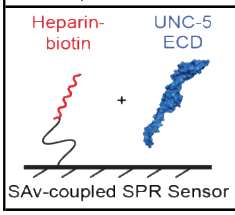	Wild-type	26.3*	3.6	1.00
	N18E	78.9*	4.7	0.334
	N188E	80.8*	6.6	0.326
	N18K	6.84*	0.78	3.85
	N188K	5.14*	0.54	5.12
	N18K N188K	1.68	0.36	15.7

Table 2.2. Summary of fitting of SPR sensorgrams in Figure 2.7, with standard error of the parameter reported by Prism (GraphPad).

We observed in our yeast display experiments that the UNC-5–UNC-6 affinity is significantly improved in the presence of heparin. We confirmed these results with SPR: UNC-5 binds UNC-6ΔC with a K_D of 1.2 μM in the presence of 5 μg/mL (0.31 μM) heparin, an improvement of 39-fold compared to UNC-5–UNC-6ΔC binding in the absence of heparin (**Figure 2.7B** and **Figure 2.8B**). At this heparin concentration (5 μg/mL), we expect that while UNC-6 molecules are in complex with heparin, free wild-type (WT) UNC-5 would be mostly unoccupied with heparin, and therefore the complex formation is unlikely to be a result of heparin chain simply recruiting UNC-5. As the two Asn's at the IG1-IG2 boundary can be mutated to positively charged Lys to improve UNC-5 affinity for both heparin and UNC-6, we expect that UNC-5 binding to UNC-6 in the presence of heparin should also be improved with

these mutations: UNC-5 ectodomains with N18K and N188K mutations bind UNC-6 more strongly in the presence of heparin (**Figure 2.7B** and **Figure 2.8B**).

Based on our yeast display and structural work, we were also able to create partial loss-of-function UNC-5 mutants by mutating the two Asn residues to Glu's. UNC-5 ectodomain with either N18E or N188E mutations show weaker binding to heparin (**Figure 2.7C** and **Figure 2.8D-E**), and weaker binding to UNC-6 in the presence or absence of heparin (**Figure 2.7A-B** and **Figure 2.8A-B**), with an affinity 4 to 10-fold worse than the wild-type UNC-6–UNC-5 interaction in the presence of heparin, and 1.6 to 1.8-fold worse in the absence of heparin (**Figure 2.8C**).

While the N→E mutants of UNC-5 have lower affinity for UNC-6 as expected, binding is not abolished due to the presence of extensive positive charge at the IG1-IG2 boundary of the UNC-5 ectodomain. Based on the crystal structure of the UNC-5–heparin complex, we designed four mutants of UNC-5, reversing charge at the heparin-binding site. Mutants contained a subset or all of the following amino acid substitutions: R17E, R70E, K11E, R190E, and R191E. All of the mutants showed a drastic reduction in heparin affinity; e.g., UNC-5 ectodomains with the double mutation R17E R70E lost heparin-binding affinity by >20-fold compared to WT (**Figure 2.9A,A'** and **Figure 2.10A,D**). Binding to UNC-6, in the absence or presence of heparin, is also affected with all mutants, but only slightly when heparin is absent (**Figure 2.9B** and **B', Figure 2.10B**), but to a much greater degree when heparin is present (**Figure 2.9C,C'** and **Figure 2.10C,E**): For example, UNC-5 R17E R70E binds UNC-6ΔC in the presence of 5 μg/mL heparin with a dissociation constant (K_D) ≥50 μM (**Figure 2.9C'**). The mutations to the UNC-5 ectodomain modified affinity to both heparin and UNC-6, suggesting that the heparin-binding site of UNC-5 is near the UNC-6-binding site as well. These results imply that UNC-5 binding to

heparin strongly facilitates UNC-6 binding, and that there are additional weak contacts between UNC-5 and UNC-6 that are heparin independent, in agreement with the observation that UNC-5 binds UNC-6 weakly in the complete absence of heparin.

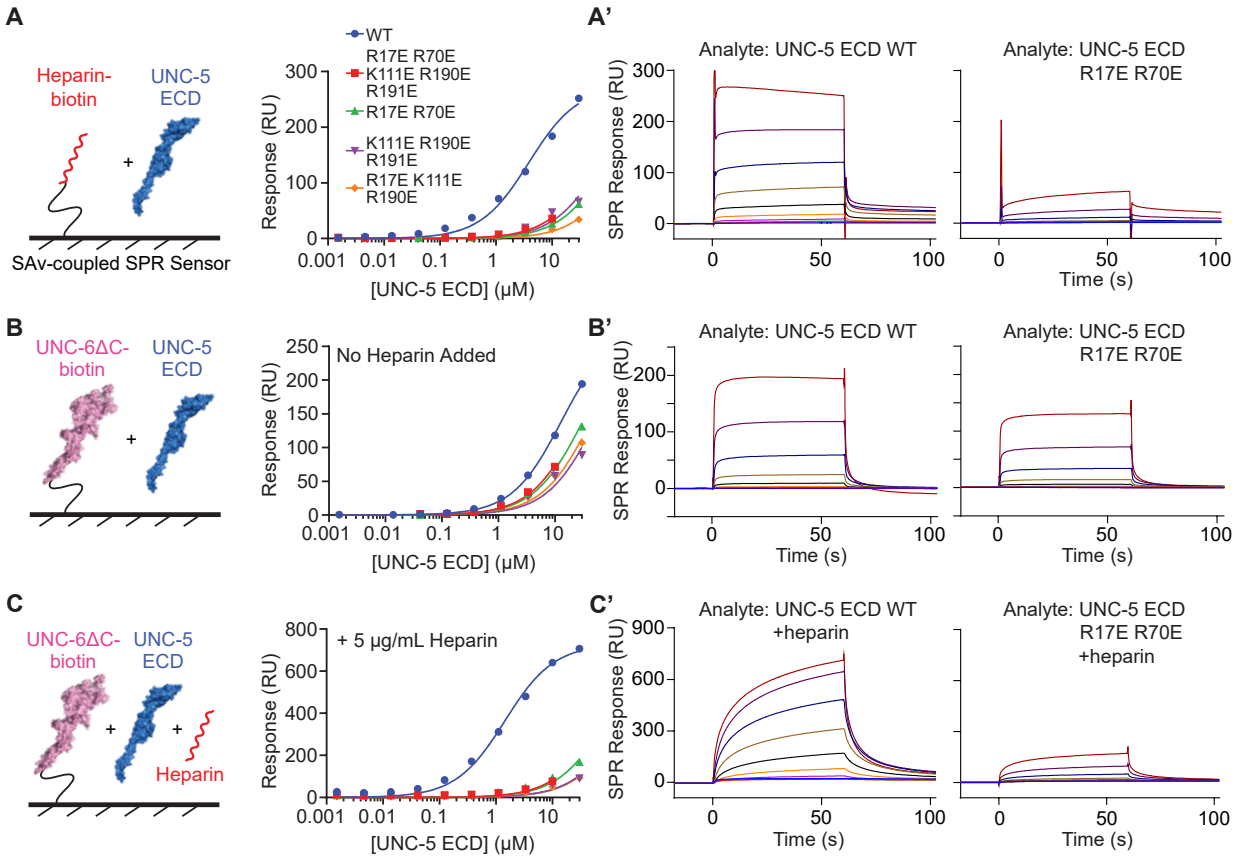

Figure 2.9. Loss of heparin binding by UNC-5 accompanies loss of UNC-6 binding.

A. Experimental design (left) and binding isotherms (middle) for SPR experiments testing the interaction of biotinylated heparin with UNC-5 ECD WT and mutants, where all UNC-5 variants (including WT) were run over the same SPR chip channel containing heparin within one experiment. UNC-5 ECD mutants contain a subset or all of the following amino acid substitutions designed to disrupt heparin binding: R17E, R70E, K11E, R190E, and R191E. Since mutants bind very weakly by design, we used the maximum saturation response values fit to the highest-affinity variant within each experiment as a constraint for fitting the lower-affinity variants. **A'.** SPR sensorgrams for WT UNC-5 and the R17E R70E mutant in A. See **Figure 2.10** for all variants tested. **B, C.** Experimental design (left) and binding isotherms (right) for SPR experiments testing the interaction of biotinylated WT UNC-6ΔC with UNC-5 ECD WT and mutants without heparin (B) and in the presence of 5 μg/ml heparin (C). WT and mutant series were run on a single UNC-6ΔC channel on the SPR chip during the same experiment. **B', C'.** SPR sensorgrams for WT UNC-5 and the R17E R70E mutant in B and C. See **Figure 2.10** for all variants tested. K_D's are tabulated in **Table 2.3**.

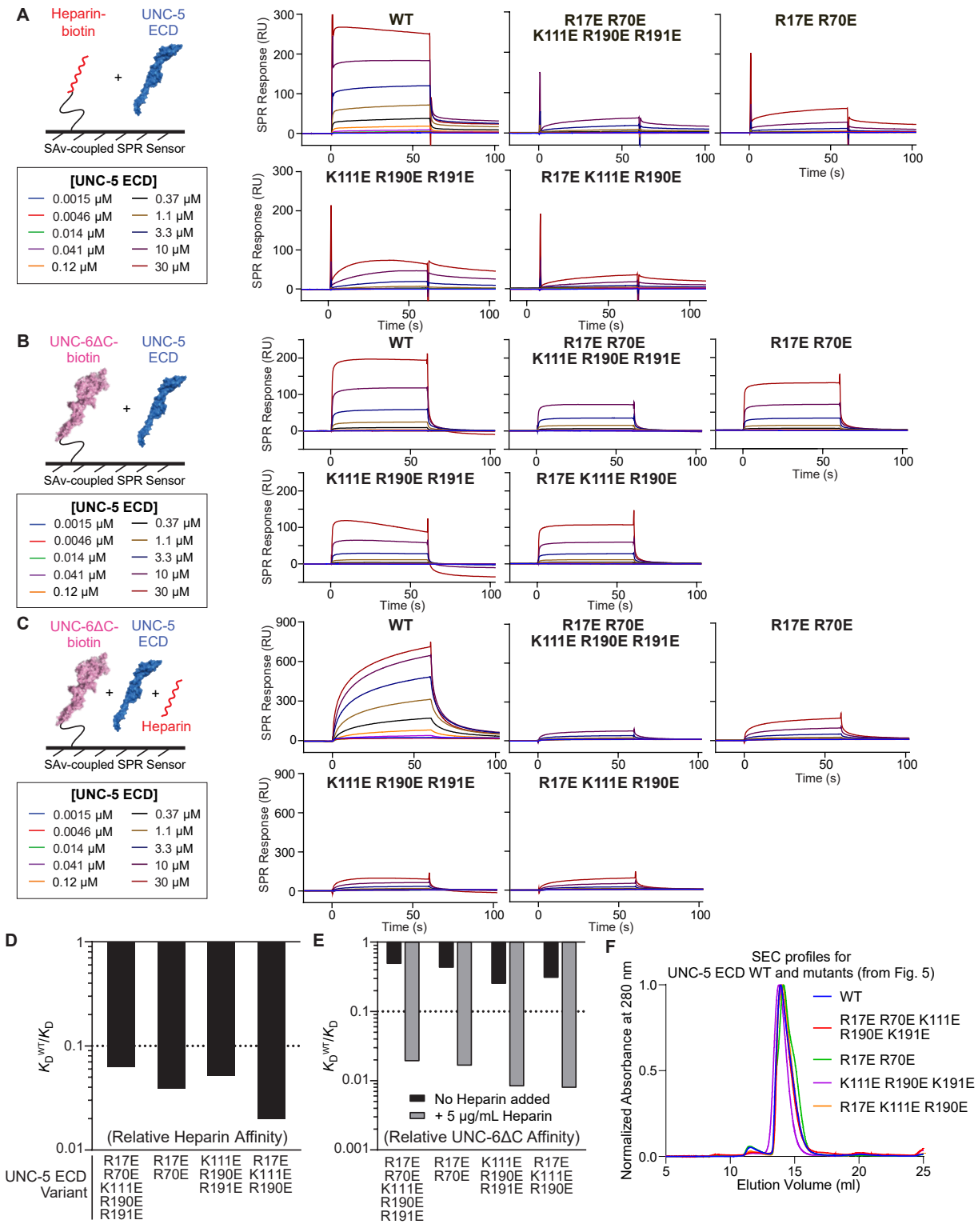

Figure 2.10. SPR sensorgrams for isotherms reported in Figure 2.9.

Continued on next page.

Figure 2.10 continued. A-C. Same channel on the SPR chip was used within each panel, allowing for direct comparison of response values between mutants. **D,E.** Loss of heparin (D) and UNC-6ΔC (E) affinity of UNC-5 ECD R/K-to-E mutants, summarized as ratios of WT K_D to mutant K_D. Larger bars indicate larger loss of affinity. **F.** SEC profiles for wild-type and mutant UNC-5 ECD in panels A-C during purification over a Superdex 200 10/300 column.

Experimental Design	UNC-5 ECD variant	K_D (μM)	Standard error of the fit (μM)	K_D^{WT}/K_D
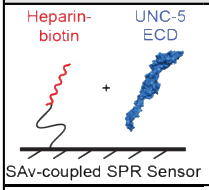	Wild-type	3.86	0.34	1.00
	R17E R70E K111E R190E R191E	62.3*	3.3	0.0620
	R17E R70E	100*	3	0.0385
	K111E R190E R191E	77.0*	8.8	0.0502
	R17E K111E R190E	197*	11	0.0196
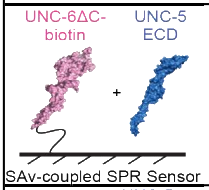	Wild-type	12.8	0.2	1.00
	R17E R70E K111E R190E R191E	27.1*	0.9	0.473
	R17E R70E	30.8*	1.1	0.416
	K111E R190E R191E	52.5*	5.1	0.244
	R17E K111E R190E	43.0*	2.1	0.298
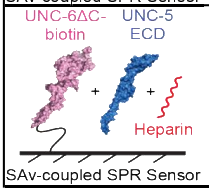	Wild-type	1.44	0.11	1.00
	R17E R70E K111E R190E R191E	77.6*	10.9	0.0186
	R17E R70E	89.6*	8.1	0.0161
	K111E R190E R191E	178*	25	0.00809
	R17E K111E R190E	187*	17	0.00768

Table 2.3. Summary of fitting of SPR sensorgrams in Figure 2.9, with standard error of the parameter reported by Prism (GraphPad).

2.2.6 Heparin binding creates a large and stable repulsive Netrin-Receptor complex

Since heparin can bind both UNC-6/Netrin and UNC-5, and increase their affinity to each other, we next asked the question if we can reconstitute a stable extracellular complex of UNC-6 and UNC-5. Over size-exclusion runs, we could not see a stable UNC-6ΔC–UNC-5 ECD complex without heparin (**Figure 2.11A**), which is expected due to their low affinity in the absence of heparin (**Figure 2.10B**). When heparin (from porcine intestinal mucosa, ~16 kDa) was added at a 1:1:1.5 UNC-6:UNC-5:heparin molar ratio, a large stable complex was observed (**Figure 2.11B**). The UNC-6–UNC-5–heparin complex peak elutes at 10.72 ml (~0.46 column volumes [CV]) on a Superose 6 10/300 column, not at the void volume (7.20 ml; ~0.31 CV) and

well within the separation range (up to 5 MDa). Sodium dodecyl-sulfate polyacrylamide gel electrophoresis (SDS-PAGE) analysis of the complex peak show a complex including a roughly 1:1 molar ratio of UNC-6:UNC-5 (**Figure 2.11B** and **Figure 2.12A**). In size-exclusions chromatography (SEC) runs, we have observed some UNC-5 and UNC-6 eluting much later than the complex peak: We observed this to be due to sulfate ions competing with heparin and preventing complex formation. We include magnesium sulfate in UNC-6ΔC preparations and in the SEC buffer to prevent non-specific interactions of UNC-6 (see Methods).

We also hypothesized that the formation of the UNC-6–UNC-5 complex and its size may depend on the heparin polymer size. In fact, repeating the experiment with shorter heparin fragments of result in smaller complexes or loss of the complex peak altogether on a SEC runs (**Figure 2.12B**).

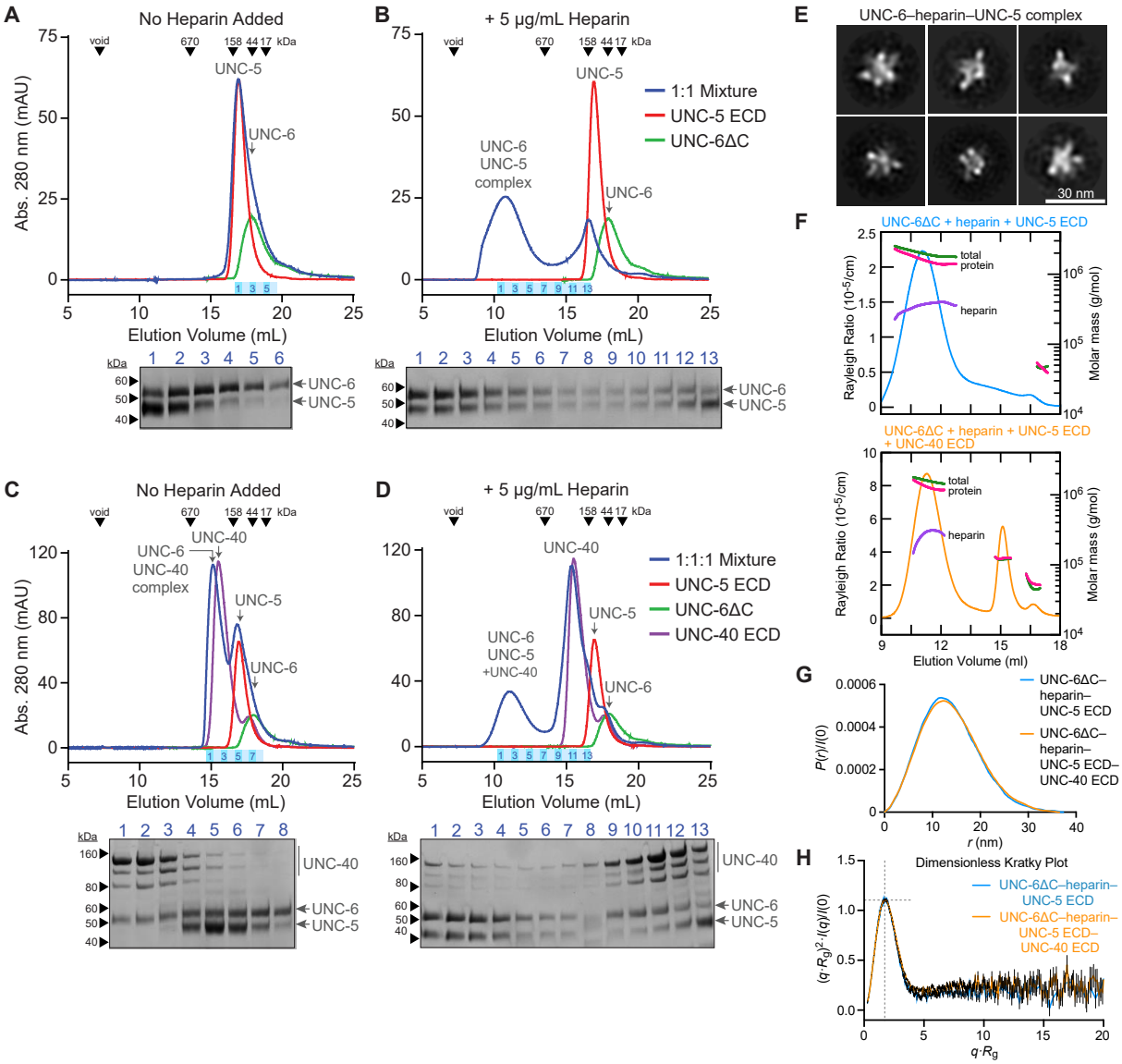

Figure 2.11. UNC-5 and UNC-6 form a large oligomeric complex in the presence of heparin.

Continued on next page.

Figure 2.11 continued. A, B. Size-exclusion chromatography of UNC-5 ECD and UNC-6ΔC. UNC-5 ECD (red), UNC-6ΔC (green), and a 1:1 molar ratio mixture (blue) were injected without added heparin (**A**) and with 5 µg/ml heparin (B) on a column equilibrated in HBS-MS and no additional heparin. Chromatograms in A-D show elution profiles measured by absorbance at 280 nm with a pathlength of 0.2 cm, using a Superose 6 Increase 10/300 column along with SDS-polyacrylamide gels of eluted fractions from the runs with mixtures (blue). Coomassie-stained bands are quantified in **Figure 2.12A**. **C, D.** Size-exclusion chromatography of UNC-5 ECD, UNC-6ΔC, and UNC-40 ECD. UNC-5 ECD (red), UNC-6ΔC (green), UNC-40 ECD (purple), and a 1:1:1 mixture (molar ratio, blue) were injected without heparin (**C**) and with 5 µg/ml heparin added (D) on a Superose 6 10/300 column equilibrated with HBS-MS. Coomassie-stained SDS-polyacrylamide gels for the mixture runs (blue) are placed under the chromatograms, and are quantified in **Figure 2.12A**. **E.** Selected class averages of particles from negative-stained electron microscopy images for the UNC-6–heparin–UNC-5 complex. For raw images, see **Figure 2.13A**. **F.** Molar mass measurements with conjugate analysis using SEC-MALS data for (top) UNC-6ΔC + heparin + UNC-5 ECD and (bottom) UNC-6ΔC + heparin + UNC-5 ECD + UNC-40 ECD. Blue and orange curves represent excess Rayleigh ratios, and green, magenta and orange curves are molar mass measurements for total, protein and conjugate (heparin) content, respectively. See **Table 2.4** for details. **G.** Pair distribution plots for SAXS data, showing a mostly globular shape for the UNC-6–heparin–UNC-5 complex (blue) and the UNC-6–heparin–UNC-5–UNC-40 complex (orange). **H.** Dimensionless Kratky plots for both complexes. Dashed lines mark ($\sqrt{3}$,3/*e*), the expected maximum for a globular, rigid molecule. Additional analysis of SAXS data is in **Figure 2.13** and **Table 2.5.**

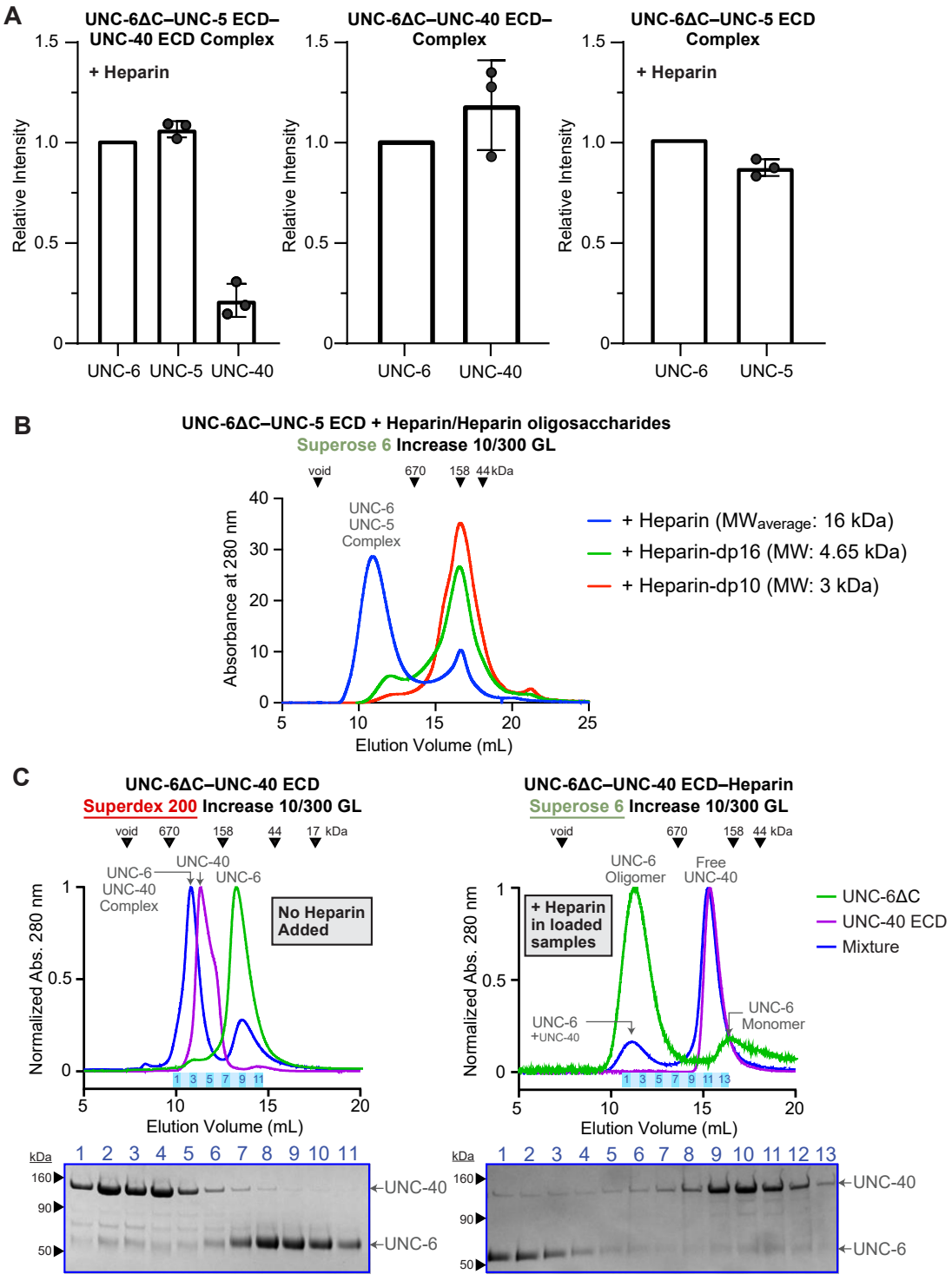

Figure 2.12. Longer heparin chains are more effective in UNC-5-UNC-6 complex formation.

Continued on next page.

Figure 2.12 continued. A. Coomassie blue-stained band intensities of purified UNC-6ΔC–UNC-5 ECD–UNC-40 ECD (**Figure 2.11B)**, UNC-6ΔC–UNC-40 ECD (**Figure 2.11C**), and UNC-6ΔC–UNC-5 ECD (**Figure 2.11D**) complexes were analyzed (n = 3 lanes in SDS-polyacrylamide gels). All complexes were purified in SEC after mixing proteins in equimolar ratios, and with excess heparin (1.5 molar ratio) for the first two complexes. Band intensities were quantified using Image Lab (Bio-Rad Laboratories) and analyzed in Prism (GraphPad). **B.** Long heparin chains are needed to create UNC-6–UNC-5 oligomers. Shorter heparin chains are less effective in complex formation, as assessed by SEC (Superose 6 Increase 10/300). **C.** (*Left*) SEC profiles for UNC-6ΔC, UNC-40 ECD, and 1.5:1 mixture of UNC-6ΔC:UNC-40 ECD ran on a Superdex 200 Increase 10/300 GL column. In the absence of heparin, most of the protein mixture forms an UNC-6ΔC–UNC-40 ECD complex and excess free UNC-6ΔC elutes later. (*Right*) SEC profiles for UNC-6ΔC, UNC-40 ECD, and 1:1:1.5 mixture of UNC-6ΔC:UNC-40 ECD:heparin ran on a Superose 6 10/300 GL column. When heparin is present in the protein mixture, the majority of UNC-6ΔC forms a high-MW oligomer with a substoichiometric amount UNC-40 ECD and excess free UNC-40 ECD elutes later. Please see that the two columns used on the left and right are different, since the complexes observed in the absence and presence of heparin are very different in size.

2.2.7 Presence of heparin and UNC-5 mostly excludes UNC-40 from an UNC-6 complex

It has been suggested that heparin binding might bias the binding of Netrins towards specific receptors [35]. If that is the case, we may expect heparin to weaken or break the otherwise stable UNC-6 complex with UNC-40/DCC. When UNC-6ΔC, UNC-5 and UNC-40 ECDs are mixed in the absence of heparin and applied to an SEC column, we could only observe this UNC-6–UNC-40 complex and free UNC-5 (**Figure 2.11C**). However, when heparin is included in the mixture, we observed a very large complex peak containing UNC-6 and UNC-5 with a largely substoichiometric UNC-40 content, and excess free UNC-40 eluting much later (**Figure 2.11D** and **Figure 2.12A**). This confirms that heparin and/or UNC-5 mostly competes with UNC-40 for UNC-6 binding. Since UNC-40 is also needed for some repulsive UNC-5-mediated functions [33,78,83], UNC-40 may contribute to repulsive signaling as part of a Netrin–UNC-5 complex, probably at a lower stoichiometric ratio to not initiate attractive signaling. Removing heparin from this SEC run with three proteins resulted in the loss of the MDa-sized complex peak, and formation of the attractive UNC-6–UNC-40 complex (**Figure 2.11C**).

Similarly, additional SEC runs where UNC-6ΔC and UNC-40 ECD are mixed and loaded show that including heparin in the injected samples results in breaking the UNC-6–UNC-40 complex, with nearly all UNC-40 eluting as free protein, while mostly-UNC-6 oligomers are formed (**Figure 2.12C**). This further suggests that heparin or HS may down-regulate formation of the attractive complex, while promoting the repulsive one.

2.2.8 Biophysical properties of the heparin-mediated UNC-6–UNC-5 oligomers

An important question relevant to UNC-5 signaling is whether (1) the heparin and UNC-6-mediated UNC-5 oligomers are an ordered and well-defined molecular species, or if (2) these oligomers are simply a result of UNC-6 and UNC-5 decorating the long, linear heparin chains. The two hypotheses may be distinguished based on methods that measure shape and flexibility. We first used negative-staining electron microscopy to visualize the UNC-5–heparin–UNC-6 complex (**Figure 2.11E** and **Figure 2.13A**). The images and class averages consistently show a large, globular complex, and not long or thin chains.

We also used multi-angle light scattering (MALS) and small-angle x-ray scattering (SAXS) to study these complexes in solution: Heparin, UNC-6ΔC, and UNC-5 ECD were mixed and injected onto an SEC column, and MALS and SAXS data were collected as the complex eluted. MALS data show that the complex is 1.5 to 2.0 MDa, and conjugate analysis of the complex peak indicate a significant (~19%) presence of heparin (**Figure 2.11F** and **Table 2.4**). The pair distribution ($P(r)$) plot and the molecular shape analysis from the SAXS data both indicate a strongly globular complex, and the dimensionless Kratky plot confirms a highly rigid molecular species (**Figure 2.11G**, **Figure 2.13B-F** and **Table 2.5**).

Given inherent flexibility of the heparin chain, the multi-domain nature of the proteins, including the flexible UNC-5 ectodomain (**Figure 2.4A**) and their elongated structures, this is

not expected, and indicates that the UNC-6–heparin–UNC-5 complex has a stable, ordered geometry and defined structure, which may be important for a signaling-competent conformation on the cell surface. The various mass and size measurements by MALS (**Figure 2.11F** and **Table 2.4**), SAXS (**Table 2.5**) and comparison of the particle dimensions in EM micrographs (**Figure 2.13A**) and the SAXS *P*(*r*) plots (**Figure 2.11G**) show good agreement between the methods used. We also added the UNC-40 ECD to our SEC-MALS-SAXS samples of UNC-6ΔC + UNC-5 ECD + heparin (**Figure 2.11F-G** and **Figure 2.13B-F**): The substoichiometric UNC-40 ECD did not significantly affect the shape, flexibility and structure of the UNC-5–heparin–UNC-6 complex; its physiological effects are likely contributed via its intracellular signaling motifs.

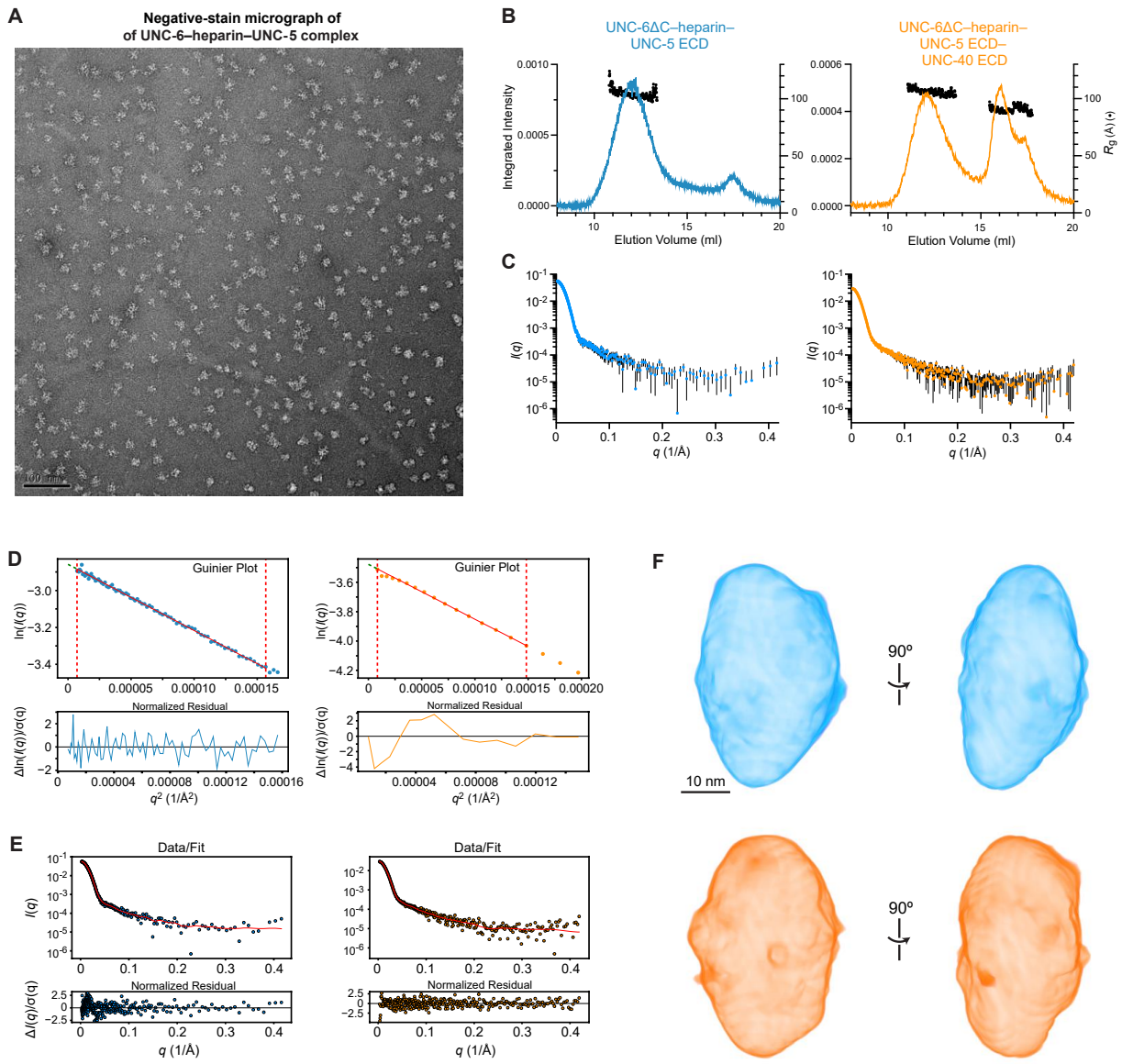

Figure 2.13. UNC-6–heparin–UNC-5 and UNC-6–heparin–UNC-5–UNC-40 complexes are globular and rigid.

A. Negative-stain EM micrograph of the UNC-6ΔC–heparin–UNC-5 ECD complex. **B.** Integrated intensity profiles of SEC runs for SEC-SAXS data collected for the UNC-6 + heparin + UNC-5 (blue) and UNC-6 + heparin + UNC-5 + UNC-40 samples (orange), with radius of gyration (R_g) overlayed on the peaks. A Superose 6 10/300 was used as the SEC column. **C.** Scattering intensity as a function of scattering angle (transformed as the momentum transfer, q) for the complex peaks. **D.** The linear Guinier plot and the normalized residuals to the Guinier fits for both complexes. **E.** The data fitting and residuals for the pair distribution plots in **Figure 2.11G** for the UNC-6–heparin–UNC-5 complex (blue, left) and the UNC-6–heparin–UNC-5–UNC-40 complex (orange, right). **F.** Volumes calculated for both complexes using DENSS.

	UNC-5 ECD + UNC-6ΔC + heparin	UNC-5 ECD + UNC-6ΔC + UNC-40 ECD + heparin
Experiment Type	SEC-MALS-SAXS	
Instrument	DAWN HELEOS with Optilab T-rEX at BioCAT (APS beamline 18-ID)	
Wavelength (nm)	663 (for light scattering) and 658 (for RI)	
Flow rate (ml/min)	0.6	
Chromatography column	Superose 6 10/300 Increase	
Buffer	10 mM HEPES pH 7.2, 150 mM NaCl, 100 mM $MgSO_4$	
Refractive index of the solvent (assumed)	1.321	
Temperature	25°C	
Software	ASTRA version 7 (Wyatt)	
Loading volume (µl)	450	300
Loading concentration (mg/ml)	0.89 (complex mixture)	1.09 (complex mixture)
dn/*dc**	0.188 for protein including N-glycans 0.133 for heparin	0.188 for protein including N-glycans 0.133 for heparin
Extinction coefficient at 280 nm	1.139 ml/(mg×cm)	1.145 ml/(mg×cm)
M_n**	1,980,000 (±0.12%) Glycoprotein: 1,605,000 Conjugate (Heparin): 375,000	1,590,000 (±0.11%) Glycoprotein: 1,304,000 Conjugate (Heparin): 286,000
M_w†	1,997,000 (±0.12%) Glycoprotein: 1,634,000 Conjugate (Heparin): 363,000	1,596,000 (±0.11%) Glycoprotein: 1,316,000 Conjugate (Heparin): 280,000

* *dn*/*dc* values are estimated based on predicted N-linked glycosylation content.
** Number-averaged molar mass.
† Weight-averaged molar mass.

Table 2.4. Data statistics and analysis for multi-angle light scattering experiments.

	UNC-5 ECD + UNC-6ΔC + heparin	UNC-5 ECD + UNC-6ΔC + UNC-40 ECD + heparin
Data Collection and Sample Details		
Experiment setup	SEC-MALS-SAXS	SEC-MALS-SAXS with co-flow during SAXS
Instrument	BioCAT facility at APS beamline 18-ID with Eiger2 XE 9M detector	
Wavelength (Å)	1.033	1.033
Camera length (m)	3.654	3.682
q-measurement range ($Å^{-1}$)	0.0027 to 0.42	0.0027 to 0.42
Exposure time (s)	0.25	0.5
Exposure period (s)	1.0	1.0
Flow rate (ml/min)	0.6	0.6
Chromatography column	Superose 6 10/300 Increase	
Buffer	10 mM HEPES pH 7.2, 150 mM NaCl, 100 mM $MgSO_4$	
Temperature	22°C	22°C
Software	BioXTAS RAW version 2.1.4, ATSAS 3.1.3	
Loading concentration (mg/ml)	0.89	3.0
Loading volume (µl)	450	300
Structural Parameters		
Guinier Analysis*		
$I(0)$ (cm^{-1})	0.0574 ± 0.00011	0.0309 ± 0.00005
R_g (Å)	103.72 ± 0.49	105.85 ± 0.25
q range ($Å^{-1}$)	0.00268 to 0.01252	0.00291 to 0.01218
$q_{min}R_g$ to $q_{max}R_g$	0.2778 to 1.2987	0.3075 to 1.2891
Coefficient of Correlation, R^2	0.9975	0.9958
$P(r)$ Analysis (from GNOM**)		
$I(0)$ (cm^{-1})	0.0577 ± 0.00011	0.0310 ± 0.00005
R_g (Å)	105.30 ± 0.06	106.60 ± 0.26
D_{max} (Å)	373	365
q range ($Å^{-1}$)	0.0027 to 0.4157	0.0029 to 0.419
χ^2	1.1127	0.8835
Molecular Weight Estimates		
Vc method***	2.48 MDa	2.33 MDa
Vp method†	1.33 MDa	1.77 MDa
Shape & Size method‡	1.08 MDa	1.07 MDa

* Performed in BioXTAS RAW (Hopkins, J.B. *et al*. (2017) *J Appl Crystallogr* **50**, 1545-1553).
** Svergun, D.I. (1992). *J Appl Crystallogr* **25**, 495-503.
*** Rambo, R.P. and Tainer, J.A. (2013). *Nature* **496**, 477-481. This method may not work well with mixed (protein with conjugate) samples.
† Piiadov, V., Ares de Araujo, E., Neto, M. O., Craievich, A. F., & Polikarpov, I. (2019). *Prot Sci* **28**, 454-463. This method may not work well with non-protein samples.
‡ Franke, D., Jeffries, C. M. & Svergun, D.I. (2018). *Biophys J* **114**, 2485-2492. This method may not work well with non-protein samples.

Table 2.5. Data statistics and analysis for small-angle X-ray scattering experiments.

2.2.9 Heparin-mediated UNC-6 oligomerization

We next investigated how the UNC-6–UNC-5 complex could oligomerize and hypothesized that this could be due to heparin-mediated oligomerization of UNC-6. To gain more insights into the UNC-6 structure, we were able to determine the structure of UNC-6ΔC, but not with heparin bound (**Figure 2.14A**). However, we observed an ordered sulfate ion at a highly positively charged site on the second EGF domain of UNC-6 (**Figure 2.14B**), close to where Netrin–UNC-5 binding was proposed based on antibody-blocking experiments [84]. The positive charge at this site is conserved in the monophyletic Netrin-1/3/5 family of proteins, but not in Netrins that separately evolved and are not known to mediate axon guidance (i.e. Netrin-4 and Netrin-G families) (**Figure 2.15A**) [78,85]. Finci et al. [78] has also observed putative sulfate ions in the human Netrin-1–DCC crystal structure at the second EGF domain, and proposed the positively charged surface on the EGF2 domain as a potential heparin-binding site.

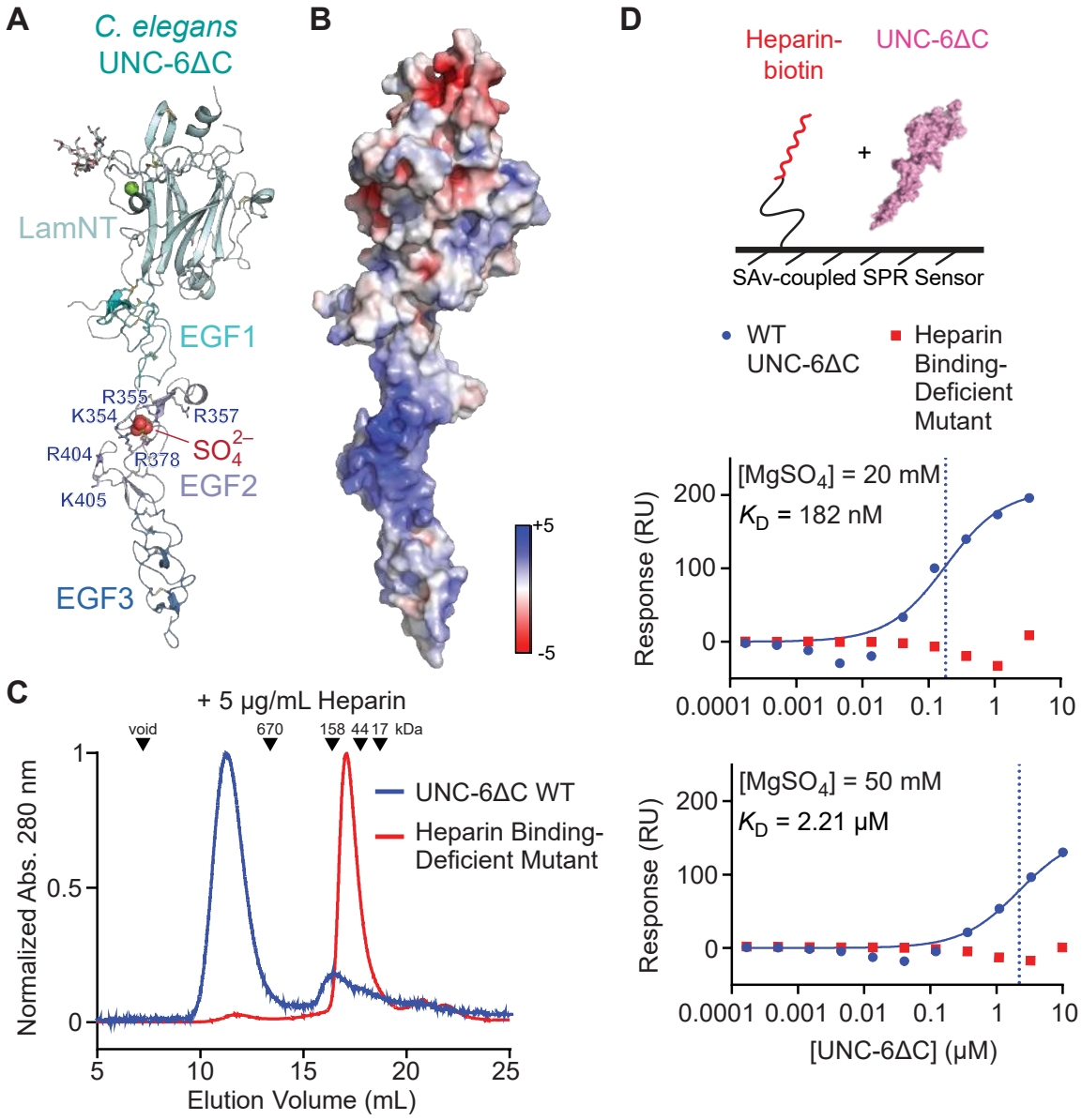

Figure 2.14. UNC-6 EGF2 is a heparin-binding site.

A, B. Our crystal structure (**A**) and electrostatic potential surface (**B**) of UNC-6ΔC. The range of electrostatic potential used to color the surface is from -5 to +5 *kT/e*. **C.** Size-exclusion chromatography of UNC-6ΔC WT (blue) and the heparin binding-deficient mutant (red) mixed with 5 µg/ml heparin. **D.** Binding isotherms for SPR experiments testing the interaction of biotinylated heparin with UNC-6ΔC WT (blue) and the heparin binding-deficient mutant (red) at two $MgSO_4$ concentrations to counter non-specific binding. Sensorgrams are shown in **Figure 2.15**.

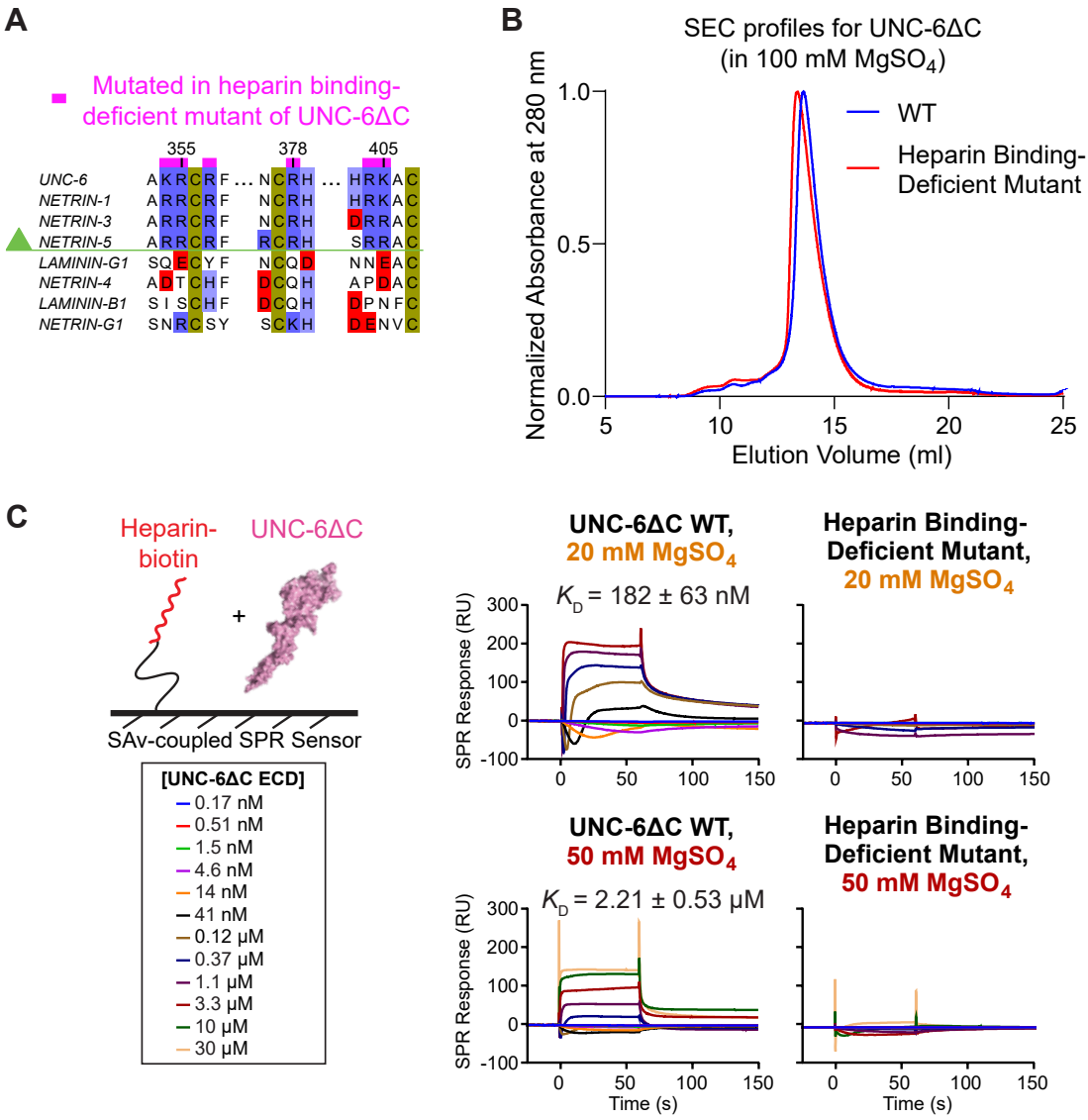

Figure 2.15. Heparin binding-deficient UNC-6ΔC mutant stability and SPR sensorgrams for isotherms reported in Figure 2.14.

A. Partial sequence alignment of UNC-6 and human Netrin homologs. UNC-6 and vertebrate Netrin-1, -3 and -5 evolved from a common ancestor, while Netrin-4 and Netrin-G1 have separate evolutionary origins. **B.** SEC profiles for wild-type and mutant UNC-6ΔC used in SPR experiments in **Figure 2.14** during purification over a Superdex 200 10/300 column. **C.** SPR sensorgrams for isotherms reported in **Figure 2.14**.

To test if the positively charged surface on EGF2 is the heparin-binding site outside the C-terminal NTR domain, we created and purified an UNC-6ΔC mutant where K354, R355, R357, R378, R404, and K405 were mutated to glutamate (**Figure 2.15B**). When WT UNC-6ΔC is run on an SEC column after being mixed with heparin at a 1:1.5 molar ratio, it runs as a large oligomer (**Figure 2.14C**). This engineered UNC-6ΔC mutant ("Heparin Binding-Deficient Mutant"), however, does not oligomerize when mixed with heparin. We also performed SPR experiments to measure heparin affinity for WT and mutant UNC-6ΔC, where biotinylated heparin was captured on an SPR chip, and soluble UNC-6ΔC was used as an analyte at a variety of $MgSO_4$ concentrations to counter non-specific binding (**Figure 2.14D** and **Figure 2.15C**). The heparin binding-deficient UNC-6ΔC mutant showed no binding, while we observed nM to μM affinity for WT UNC-6ΔC depending on the $MgSO_4$ concentration in SPR buffer, in agreement with our measurements in **Figure 2.7D**. As heparin can still bind and oligomerize WT UNC-6ΔC even in the presence of 100 mM SO_4^{2-} in SEC column running buffer, UNC-6ΔC is clearly a potent heparin-binding protein. Our results show that the positively charged site on the EGF2 domain is a heparin-binding site, which also helps oligomerize UNC-6 in the presence of heparin. Given these data, the likely explanation for the formation of large UNC-6–UNC-5–heparin complexes is heparin-mediated UNC-6 oligomerization.

2.2.10 Heparin-binding activity of UNC-5 is necessary for UNC-6-controlled dorsal migration of cells during development

To reveal if a functional Netrin–UNC-5 complex depends on the ability of UNC-5 to interact with heparin, we engineered one of our heparin binding-deficient UNC-5 mutants, R17E R70E, in *C. elegans*. Early studies have identified a requirement for UNC-6–UNC-5 signaling in dorsal guidance of both distal tip cells and motor axons. The mobile distal tip cell is the leading

cell of the developing gonad that migrates along the ventral side of the animal before turning dorsally in hermaphrodites. These cells continue to migrate to the dorsal-most region of the animal before turning again to continue migration along the anterior-posterior axis (**Figure 2.16A**) [86]. The migration route of the distal tip cells establishes the U-shaped morphology of the gonads in the adult hermaphrodite [87]. The dorsal migration requires both *unc-6* and *unc-5* [33], which is consistent with a repulsive action against a ventral source of UNC-6/Netrin [88,89]. Additionally, the HSPG LON-2/Glypican modifies UNC-6–UNC-5 signaling in the migrating distal tip cells [43]. We observed that in *unc-5(R17E R70E)* animals the majority of distal tip cells either do not turn dorsally or fail to migrate the full length of the dorsal-ventral body axis (**Figure 2.16B-C**). We compared the phenotype from these animals with mutant strains *unc-6(ev400)* and *unc-5(e53)*, previously identified as null mutants for dorsal migration-related functions [33]. The failed distal tip cell migrations of *unc-5(R17E R70E)* mutants are indistinguishable from the defects observed in null *unc-6* and *unc-5* mutant animals (**Figure 2.16C**). These results indicate that Netrin-dependent UNC-5 function requires the heparin-binding activity of UNC-5 during distal tip cell migration, as this is likely necessary for a stable, oligomeric and functional UNC-6–UNC-5 complex. They also offer a possible mechanism for how the requirement for GAGs in distal tip cell migration arises [90,91].

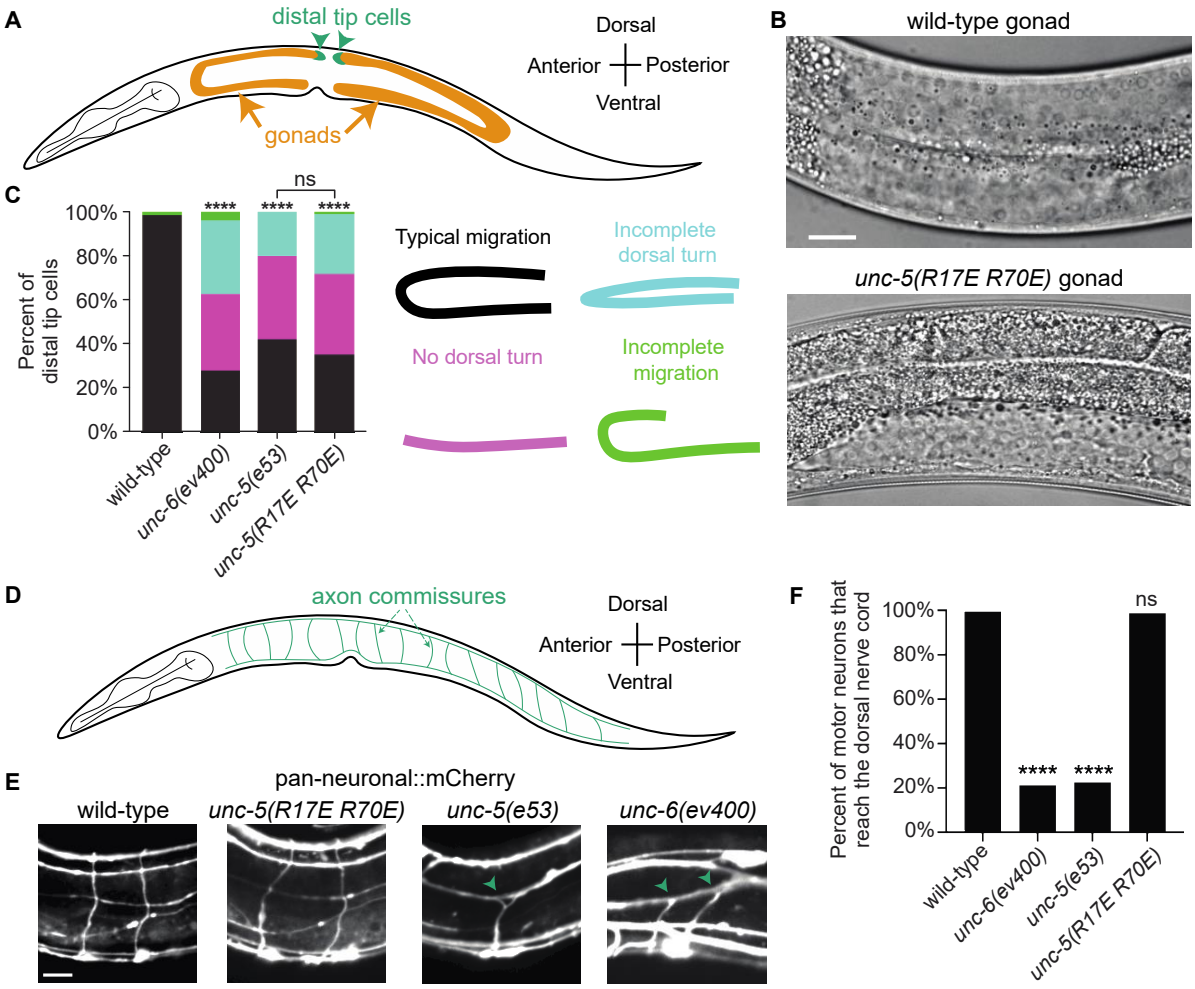

Figure 2.16. Heparin binding is required for UNC-5-mediated cell migration (from Ev Nichols and Dr. Kang Shen).

A. Cartoon drawing of the *C. elegans* gonad. Gonad morphology (orange) is established by the migration of the distal tip cell (green). **B.** Differential interference contrast (DIC) images of gonad morphology in wild-type and *unc-5(R17E R70E)* animals. Scale bar is 10 µm. **C.** Quantification of distal tip cell migration phenotypes in wild-type (*n*=68 animals), *unc-6(ev400)* (*n*=78 animals), *unc-5(e53)* (*n*=85 animals), and *unc-5(R17E R70E)* (*n*=96 animals) worms. Both *ev400* and *e53* are null alleles. Various phenotypes are observed: typical distal tip cell migration (black), a failed dorsal turn (magenta), a partial dorsal turn (blue), and incomplete longitudinal migration (green). **D.** Cartoon of the *C. elegans* motor axon commissures. Commissural axons migrate dorsally from the ventral nerve cord. **E.** Confocal images of motor axon commissures in L2 *prab-3::mCherry* transgenic animals. Green arrowheads denote axons that fail to complete their dorsal longitudinal navigation. Scale bar is 10 µm. **F.** Percent of motor neurons in wild-type (*n*=13 animals, 184 axons), *unc-6(ev400)* (*n*=13 animals, 170 axons), *unc-5(e53)* (*n*=13 animals, 209 axons), and *unc-5(R17E R70E)* (*n*=13 animals, 171 axons) L2 animals that reach the dorsal nerve cord. Motor neurons in *unc-5(R17E R70E)* animals are able to navigate to the dorsal nerve cord. Panels C and F use two-sided Fisher's exact tests. **** denotes a p-value < 0.0001. Data from this figure is from Ev Nichols and Dr. Kang Shen from Stanford University.

Given the conserved role of UNC-5–UNC-6 signaling in axon repulsion, we next investigated whether UNC-5's interaction with heparin is necessary for growth cone guidance. We studied the circumferential axon guidance known to be mediated by UNC-5 and UNC-6, where ventrally localized UNC-6 repels UNC-5 expressing neuronal commissures towards the dorsal side of the animal [33]. We found that the *unc-5(R17E R70E)* mutants animals showed normal axon guidance, suggesting that the UNC-5-heparin interaction is dispensable for the commissure axon guidance (**Figure 2.16D-F**). Consistent with the lack of morphological deficit of axon structures, these mutant animals also did not exhibit *uncoordinated* movement phenotype. Together these data indicate that UNC-5–UNC-6–HS interactions dictate some repulsive guidance *in vivo* and that neurons may have compensatory mechanisms to overcome abrogated UNC-5–UNC-6–HS binding.

2.2.11 Disrupting UNC-5–UNC-6 protein contacts results in defects in repulsive axon guidance in C. elegans

Since no high-resolution structure of an UNC-5–UNC-6/Netrin complex has been determined, we tested structure predictions using the recently released *Alphafold-multimer* (version 2.3.0) via the Colabfold implementation [92,93]. We obtained a complex model with a strong interface predicted template modeling score (ipTM) of 0.79 [92,94], indicating a likely correct interface prediction (**Figure 2.17A-C**). In the predicted model, the multiple UNC-6 domains makes contacts with UNC-5 IG2 (**Figure 2.18A**), which is known to mediate this complex [76,84,95]. Furthermore, the predicted model positions the positively charged heparin-binding surfaces of both proteins next to each other creating a composite heparin-binding site (**Figure 2.18B**), and is therefore in strong agreement with our model where an HS chain would strengthen a weak UNC-5–UNC-6 complex. To test the validity of the predicted model and

create variants of UNC-5 that break UNC-5–UNC-6 protein-protein contacts, we tested mutations at this interface. UNC-5 mutants I159A S162A D163A, I167A S169A, and T127A Q129A could not effectively form complexes with UNC-6ΔC in the presence of heparin compared to WT UNC-5 when tested using SEC runs (**Figure 2.18C**), although UNC-6ΔC oligomers can still form.

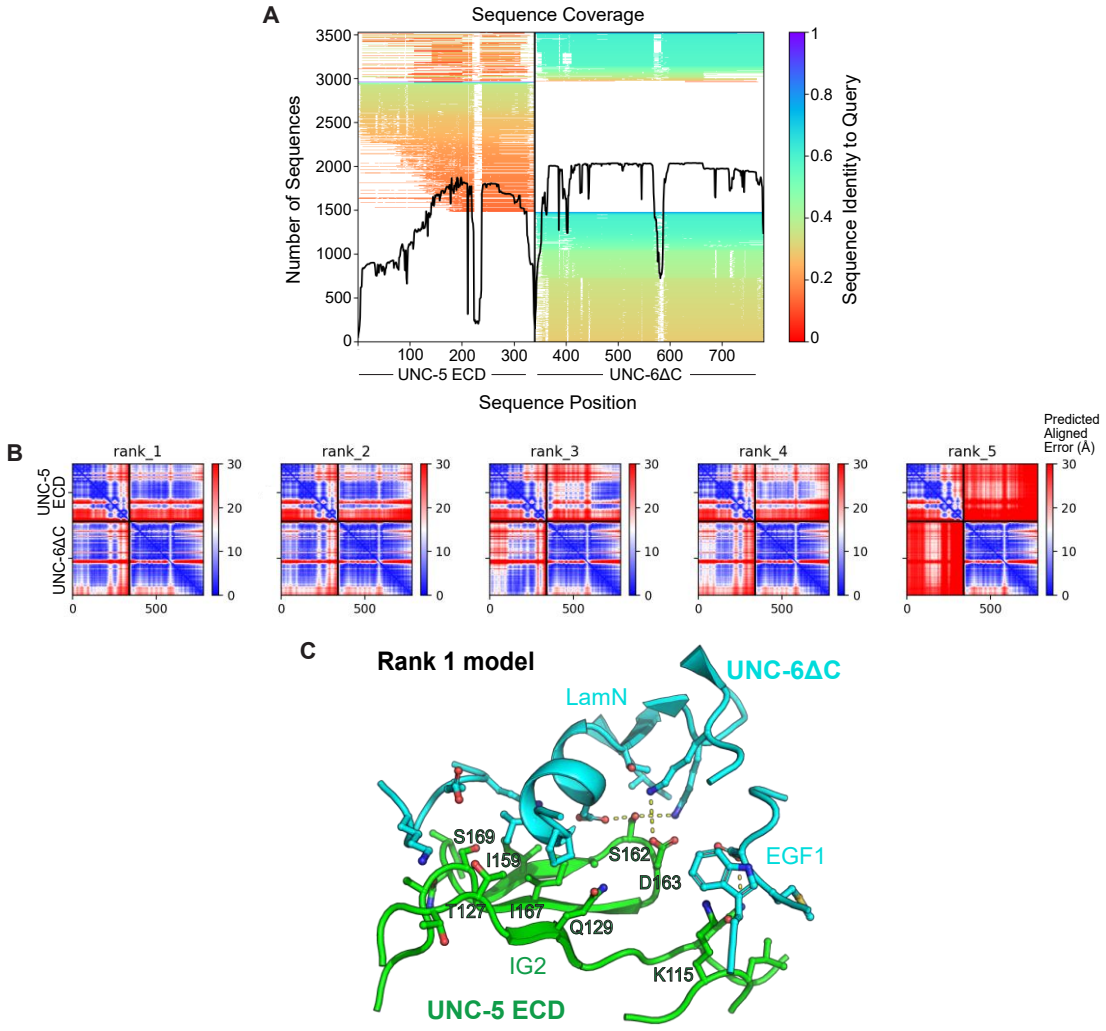

Figure 2.17. Models of the UNC-5-UNC-6 complex predicted by Alphafold.

A. Statistics for the sequence alignment used in the Alphafold prediction for the UNC-5 ECD–UNC-6ΔC complex, including the number of sequences and sequence identity to query across the UNC-5 ECD and UNC-6ΔC sequences. **B.** Predicted Aligned Error values for five models predicted by Alphafold. The best ranked (on the left) was used in designing interface mutants. **C.** UNC-6–UNC-5 interface as predicted by Alphafold (rank 1).

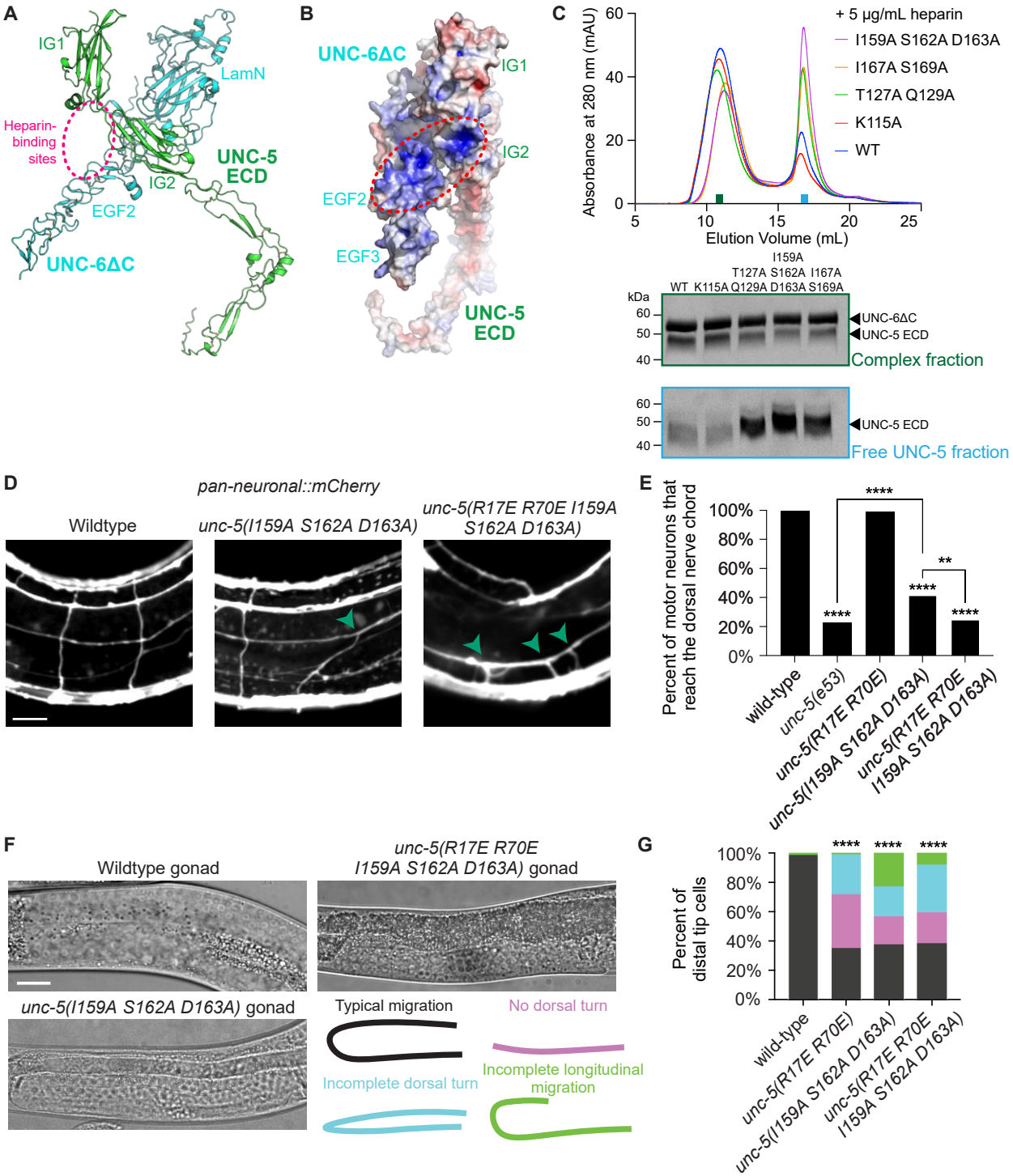

Figure 2.18. Breaking UNC-6 contacts of UNC-5 results in cell migration and axon guidance phenotypes (panels D-G are from Ev Nichols and Dr. Kang Shen).

Continued on next page.

Figure 2.18 continued. A. Highest-ranked Alphafold-multimer predicted model for UNC-6ΔC bound to UNC-5 ECD. See **Figure 2.17** for details. **B.** Electrostatic potential surface for the complex in rotated view, highlighting the contiguous positively charged surfaces we showed to bind heparin. **C.** SEC runs (Superose 6 Increase 10/300, in HBS-MS) for UNC-6ΔC and heparin mixed with WT and mutant UNC-5. The mutants are designed at the Alphafold-predicted protein-protein contacts (see also **Figure 2.1C**). The SEC fractions analyzed with SDS-PAGE are labeled with green and blue rectangles. **D.** Confocal images of motor axon commissures in L2 *prab-3::mCherry* transgenic animals. Green arrowheads denote axons that fail to complete their dorsal longitudinal navigation. Scale bar is 10 µm. **E.** Percent of motor neurons in wild-type (*n*=13 animals, 184 axons), *unc-5(e53)* (*n*=13 animals, 209 axons), *unc-5(R17E R70E)* (*n*=13 animals, 171 axons), *unc-5(I159A S162A D163A)* (*n*=13 animals, 188 axons), and *unc-5(R17E R70E I159A S162A D163A)* (*n*=13 animals, 170 axons) L2 animals. Loss of the UNC-5–HS interaction enhances motor axon dorsal migration defects in animals with disrupted UNC-5–UNC-6 binding. **F.** DIC images of gonad morphology in wild-type, *unc-5(I159A S162A D163A), and unc-5(R17E R70E I159A S162A D163A)* animals. Scale bar is 10 µm. **G.** Quantification of distal tip cell migration phenotypes in wild-type (*n*=68 animals), *unc-5(R17E R70E)* (*n*=96 animals), *unc-5(I159A S162A D163A)* (*n*=79 animals), and *unc-5(R17E R70E I159A S162A D163A)* (*n*=62 animals) worms. Various phenotypes are observed: typical distal tip cell migration (black), a failed dorsal turn (magenta), a partial dorsal turn (blue), and incomplete longitudinal migration (green). Panels E and G use two-sided Fisher's exact tests. **** denotes a p-value < 0.0001. ** denotes a p-value < 0.01. Panels D-G are from Ev Nichols and Dr. Kang Shen from Stanford University.

Next, we tested if the protein-protein contacts within the UNC-5–UNC-6 complex are required for repulsive guidance *in vivo*. We engineered the UNC-5 mutation I159A S162A D163A into *C. elegans* using clustered regularly interspaced short palindromic repeats(CRISPR)/CRISPR-associated protein 9 (Cas9). Mutant larvae displayed a mild *uncoordinated* phenotype, matched by a partial defect in repulsive axon guidance in circumferential neurons that is weaker than the phenotype of *unc-5* null animals (**Figure 2.18D-E**). These mutants also had gonad morphology defects similar to the heparin binding-deficient mutants of UNC-5 (**Figure 2.18F-G**), despite the heparin-binding site being intact. Interestingly, the severity of the *unc* phenotype in these mutants decreases with age, suggesting the axon guidance deficits were ameliorated as development progresses. When we generated *unc-5* animals with UNC-6 non-binding and heparin non-binding mutations combined (R17E R70E I159A S162A D162A), they showed a strong *uncoordinated* phenotype in larvae and adults, as

well as the distal tip cell migration defect (**Figure 2.18F-G**), indistinguishable from null *unc-5* animals. Circumferential motor axon guidance defects were observed in the combined mutant larvae at levels comparable to null *unc-5* animals (**Figure 2.18D-E**). Further, these mutants demonstrated enhanced commissural axon guidance defects compared to mutant *unc-5* animals with only UNC-6 non-binding mutations. These results show that the UNC-5–UNC-6 complex formed by weak protein-protein contacts is partially necessary for the axon guidance function of this complex *in vivo*, but heparin-binding provides an additive guidance function in UNC-5-mediated axon and cell migrations.

2.2.12 Mapping mammalian Netrin–Receptor binding sites

Structural studies on Netrins and its receptors have previously focused on mammalian orthologs. To extend our findings to vertebrate Netrins and its receptors and build on earlier structural findings, we next used structure-guided mutagenesis to study DCC and UNC5 binding sites on human Netrin-1. Two crystal structures of soluble mammalian Netrin-1ΔC constructs (previously named Netrin-1s) in complex with different truncation constructs of DCC provide a composite view with three netrin-DCC binding sites [77,78], termed here sites 1, 2, and 3, from the N-to-C termini of Netrin (**Figure 2.19A**). We created a series of human Netrin-1s constructs with point-mutant combinations so that only one intact binding site remained per construct (**Figure 2.19B-C**): To eliminate DCC binding to site 1, a point mutation was introduced in the LamN domain (S148R). Binding to the other two sites on Netrin-1 was abolished using mutations previously identified to be effective in axon guidance studies [78]: DCC binding to site 2 was abolished with a double mutant (R348D R351D) in the EGF2 domain and binding to site 3 was abolished with a single point mutant in the EGF3 domain (Q445A). The resulting biotinylated Netrin constructs were used in an AVEXIS (Avidity-based Extracellular Interaction Screening)

assay [96], where Netrin was bound to a streptavidin surface to measure binding to human draxin, or with ectodomains, domain-specific truncations, or splice variants of human DCC and UNC5B, fused with β-lactamase and cartilage oligomeric matrix protein (COMP) pentamerization domains (**Figure 2.19D**).

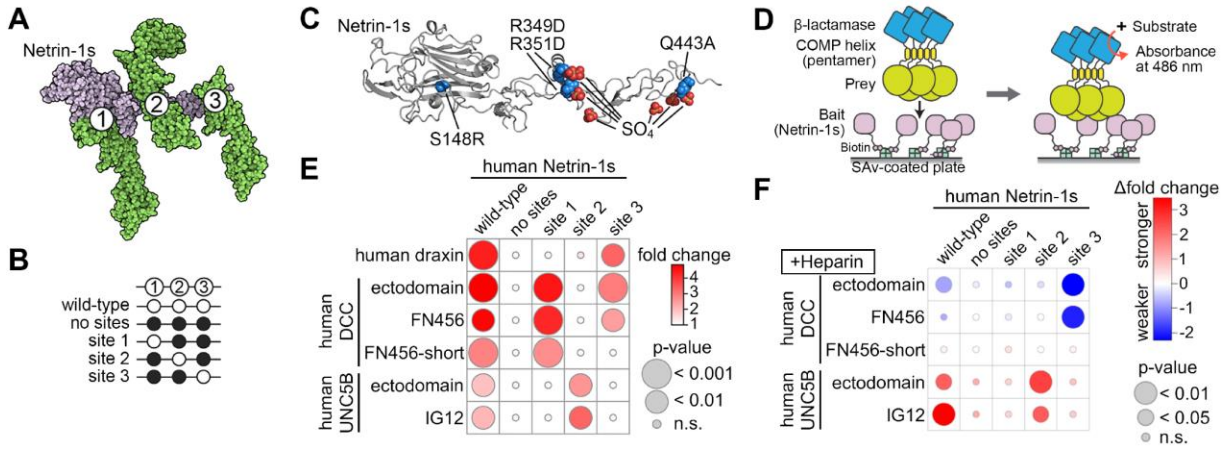

Figure 2.19: Heparin enhances human UNC5B binding and suppresses DCC binding to Netrin-1 (from Dr. Rob Meijers and Dr. Robert Smock).

A. Composite binding model of Netrin-1s (grey) with DCC (green) from available crystal structures reveals three binding sites [77,78]. **B.** Design of Netrin mutants for which only one binding site is left intact (open circles) by mutating the remaining two binding sites (filled circles). **C.** Mutations implemented (blue spheres) in Netrin-1s (gray cartoon). Clusters of sulfate ions are depicted at sites 2 and 3 (red spheres). **D.** Design of the AVEXIS assay. **E.** Site-specific binding pattern of Netrin to draxin, DCC and UNC5B in an AVEXIS assay using HEK293 secreted proteins. DCC bound within its FN456 domain to netrin in series of intensity at site 1 > site 3 > site 2 (n.s., not significant in the dynamic range of this assay), whereas UNC5B bound within its IG1+2 domains to Netrin at only site 2. A short DCC splice variant with 20-residue linker deletion between FN4 and FN5 abolishes binding specifically at site 3, while draxin binds predominantly at site 3. Fold-change in binding signal is calculated relative to background signals of HEK293 media. **F.** AVEXIS molecular assembly assay as performed in E, with the addition of 1 mg/ml of naturally heterogenous heparin. Δfold-change is the difference in fold-change of binding signals over background upon addition of HS. Data is from Dr. Rob Meijers and Dr. Robert Smock.

The binding assay showed that the Netrin-1s mutant with zero intact sites (which has four point mutations in total) abolishes binding to DCC, UNC5B and draxin, whereas the wild-type Netrin-1s construct shows binding to all three proteins (**Figure 2.19E**). The binding pattern of Netrin-1s with the DCC ectodomain occurred with relative intensities so that site 1 > site 3 > site 2, indicating that the DCC binding site to the Netrin LamN domain is the strongest as previously observed [77] (**Figure 2.19E**). As expected from prior studies [77,78], the same binding pattern was seen whether the full ectodomain of DCC was used, or a truncated version covering domains FN4, FN5 and FN6 (FN456) as used in the crystal structures. In addition, we tested Netrin binding for the splice variant of DCC that deletes a linker region between domains FN4 and FN5 ("FN456-short") that is the transiently dominant form of DCC during development of the mouse brain and neural tube, a feature which also appears conserved in humans [97–99]. In our assay, this short splice variant of DCC abolishes binding specifically at site 3 (**Figure 2.19E**). This agrees with the net reduced binding function of wild-type proteins in cell-based assays [100] and indicates specific alterations in the mechanism of Netrin-DCC assembly for the splice variant. In keeping with past findings, draxin bound Netrin only at site 3 [101], while UNC5B bound only at site 2 using its IG1+2 domains [76,84] in agreement with our *C. elegans* UNC-5–UNC-6 binding data above. Together, these binding data indicate that we have obtained the full structural scope of Netrin–DCC binding, and that Netrin site 1 binds strongly to DCC and may not be in competition with draxin or UNC5, whereas sites 2 and 3 are hotspots for variable interactions.

2.2.13 Heparin switches Netrin-Receptor selection at specific binding sites

We showed above that nematode UNC-6ΔC and UNC-5 interact strongly in the presence of heparin, and the UNC-5 and heparin compete with UNC-40/DCC binding to UNC-6/Netrin. To test the hypothesis that GAGs may also play a direct and targeted role in mammalian Netrin-

Receptor selection [39], we investigated binding patterns between the site-specific Netrin-1 mutant series and the receptors DCC and UNC5B using AVEXIS. At 1 mg/ml concentrations, heparin produced striking changes to Netrin-Receptor binding patterns (**Figure 2.19F**). Whereas DCC binding was weakened and nearly abolished at site 3, UNC5B binding was greatly strengthened at site 2. Site 1 was unaffected, in agreement with an absence of sulfate ion clusters at this site in Netrin structures, indicating no HS binding (**Figure 2.19C**). Thus, binding in competitive netrin-receptor assemblies highlights a substantial equilibrium shift and switch in preference for UNC5B inclusion when HS is a cofactor.

2.3 Discussion

The molecular environment of UNC-5-expressing neurites and cells controls their growth and migrations. In this study, we showed that GAGs regulate Netrin–UNC-5 interactions and the processes controlled by them. We deciphered the set of interactions needed to create the Netrin–heparin–UNC-5–UNC-40 complex and show that disrupting interactions between UNC-5 and GAGs causes morphological defects during development.

First, we demonstrated experimentally that UNC-5 is a heparin-binding protein. Our structural and biophysical results implicate the boundary of the IG1 and IG2 domains of UNC-5 in its interactions with HS, and possibly with UNC-6/Netrin, as UNC-5 mutations that break HS and HS-mediated UNC-6 binding also cause small, but consistent, loss of binding to UNC-6 in the absence of heparin. These findings are supported by previous results showing that the IG domains are necessary and sufficient for binding between human Netrin-1 and UNC5C [76,95] and mouse Netrin-1 and UNC5H2 [84].

We present a model of an UNC-6–heparin–UNC-5 complex that is very large yet well-ordered. For this, we demonstrated that the EGF2 domain of UNC-6/Netrin is a heparin-binding site, and heparin can oligomerize UNC-6 through this secondary interaction site, even in the absence of its C-terminal NTR domain, which was identified as the primary heparin interaction site previously [48]. Our findings on the EGF2 domain are compatible with previous biochemical studies, which had implicated the Netrin EGF2 domain in Netrin–UNC-5 interactions [84,95], and EGF2 as a potential HS-binding site was recognized [78] but had not been shown. Our work also suggests that multiple domains of UNC-6 (LamN, EGF1 and EGF2) may be involved in protein-protein contacts with UNC-5, which explains previous observations that repulsive guidance activity of UNC-5, and binding to Netrin may be mediated by many domains of UNC-6 [95,102].

It is reasonable to assume that the length of the linear heparin/HS chains help determine the size of the MDa-sized UNC-6 oligomers and the UNC-6–UNC-5 complex, and our small-angle x-ray scattering data also strongly point to a globular and rigid complex. Considering the flexibility of linear heparin chains but also the direct protein-protein contacts between UNC-6 and UNC-5 (which we could break with specific mutations), we propose that such a rigid and large complex must form via a combination of protein-protein and protein-glycan contacts. This composite model of interactions to form Netrin–UNC-5 complexes is appealing, as the specificity of binding would best be provided by protein-protein (UNC-6–UNC-5) contacts, even when interactions with heparin/HS provide much of the binding energy for the formation of the UNC-6–UNC-5 complex.

While we favor a model where UNC-6–UNC-5 contacts provide specificity for turning on UNC-5-mediated repulsive signaling, it is possible that sulfation domains within the HS chain, as well as additional interactions with the polypeptide chain of an HSPG, can regulate

UNC-5 actions and contribute to specificity *in vivo*. This last possibility may be true for an attractive Netrin receptor, *C. elegans* UNC-40/DCC, which was shown to interact with the polypeptide chain of the HSPG LON-2/glypican [43].

Since heparin and HS molecules are long, linear chains of sulfated glycans, one such molecule can usually bind more than one protein ligand. However, as we are adding a molar equivalent or excess heparin to UNC-6 or UNC-5+UNC-6 in our experiments, we had expected a majority of UNC-6–heparin or UNC-6–UNC-5–heparin complexes to include one or two protein chains bound to one heparin molecule, rather than very large complexes in the MDa size range. Our observations, therefore, suggest that UNC-6 alone or the UNC-6–UNC-5 complex can oligomerize on heparin chains in a cooperative manner, which further supports the model that protein-protein contacts within UNC-6–UNC-6 and UNC-6–UNC-5 oligomers are crucial to support large oligomer formation, in addition to necessary protein contacts with heparin. Netrins present a binding hub, due to their multi-functional sites 2 and 3. We previously showed that draxin remodels Netrin-receptor assembly to elicit distinct cellular behaviors [103], and demonstrate here that this concept could be further generalized with other netrin "cofactors", such as HS. Our results support the hypothesis that GAGs play a more direct and targeted role in Netrin-Receptor selection that is reminiscent of the variable roles of HS and various GAGs in other neuronal receptor signaling mechanisms [39]. It is also possible that a specific HS moiety may bind more potently than other segments along the chain, and length of an HS chain increases the probability of its occurrence.

We also attempted to reconstitute the UNC-6–UNC-5–UNC-40 complex, which had been observed before in pull-down experiments [83], but not successfully at scale. We observed that heparin can inhibit interactions between nematode and mammalian UNC-6/Netrin and UNC-

40/DCC. When we mixed UNC-5, UNC-6, UNC-40 and heparin, we observed UNC-40 on the large oligomer, but only at a largely substoichiometric ratio, probably mediated by UNC-6–UNC-40 interactions using site 1 on UNC-6, which is free of heparin and UNC-5 contacts. This observation supports the hypothesis that UNC-5 and/or heparin might at least partly compete for UNC-40/DCC binding on UNC-6/Netrin [35], which has functional consequences: Repulsive signaling may require UNC-40/DCC to not strongly cluster, which would otherwise lead to attractive signaling, but still be present in a complex with highly clustered UNC-5 molecules for a repulsive outcome. The competition model, where UNC-5 and heparin displace UNC-40/DCC from UNC-6/Netrin, was previously proposed in a functional setting, where UNC-5 outcompeting DCC on site 2 on Netrin results in axon repulsion, in agreement with our model [78].

In addition to structural insights, we were able to use the molecular reagents we engineered, i.e. UNC-5 variants, to directly ask the following functional question: Is the UNC-5–heparin interaction we discovered necessary for the *in vivo* functions UNC-5 performs, especially those that are UNC-6-dependent? We created animals with the heparin non-binding mutation UNC-5 R17E R70E, which has lost its UNC-6ΔC affinity by >40-fold in the presence of heparin, but only ~2-fold in the absence of heparin, compared to wild-type UNC-5. These animals displayed gonadal morphology defects comparable to *unc-5* and *unc-6* null animals [33], supporting our *in vitro* results and structural data on identifying the UNC-5–heparin interaction site and the functional importance of this interaction.

Previous studies have reported that cell migration defects, including several mesodermal cells, such as the distal tip cells in the gonad, are accompanied by dorsal axon guidance phenotypes in *unc-5* and *unc-6* mutant animals [33]. We have observed that when UNC-5 is no longer able to interact with HS but retains its weak UNC-6 affinity, the two phenotypes can be

separated: Distal tip cell migration is fully altered as in null *unc-5* or *unc-6* animals, while axon guidance towards the dorsal nerve chord is not affected. This observation may be explained by several mechanisms: (1) UNC-5-mediated cell migrations may depend on the higher affinity of HS-mediated UNC-6–UNC-5 interactions while a weaker affinity in the absence of HS is sufficient for axon guidance functions as a result of different dosage dependence in the two systems, or (2) the presence of HSPGs and HS-mediated oligomerization of the UNC-6–UNC-5 complex is necessary for signaling during distal tip cell migrations. It is speculative but possible that HSPG interactions allow for haptotactic responses where UNC-6/Netrin is immobilized on an HSPG substrate, which could then be required during distal tip cell migration.

We also engineered UNC-5 to bind heparin with higher affinity than wild-type: It would be interesting to see if higher HS affinity would allow this UNC-5 variant (N18K N118K) to respond to UNC-6 at lower doses or at lower-density tracks of HSPGs, resulting in premature dorsal cell migrations *in vivo*. Recent transcriptomic analyses of *C. elegans* neurons have revealed low, but detectable, levels of *unc-5* transcript in neurons which do not rely on UNC-5 signaling for proper axon outgrowth [104]. As such, *in vivo* mutations that increase HS affinity may also phenocopy axon migration defects after UNC-5 overexpression in touch receptor neurons. In these neurons, ectopic expression of UNC-5 was shown to reroute axons toward the dorsal region of the animal [88].

Furthermore, we were able to characterize direct UNC-6–UNC-5 contacts using an Alphafold-predicted model. When we broke both UNC-6 and heparin/HS contacts of UNC-5, we could reproduce a full cell migration and axon guidance phenotype as observed in *unc-5* or *unc-6* null animals.

During the review of our manuscript, two articles were released that complement our findings on the roles of proteoglycans and GAGs in Netrin and/or UNC-5 function. Meier *et al*. [105] observed that vertebrate Netrins oligomerize with heparin through interactions with their EGF2 domains, similar to our findings with UNC-6, and breaking this interaction in the nematode model results in the DTC migration phenotype as we have shown for UNC-5. Akkermans et al. [36] showed that mouse UNC5D can form oligomers with a glypican, but without contacting the HS chain. These studies further highlight the need to study neurite and cell migration within the context of surrounding proteoglycans and other relevant co-factors *in vivo*.

Lastly, our biochemical and structural findings are also in line with the large body of available functional data, beyond our own *in vivo* results. It was observed that milder phenotypes of *unc*-5 partial loss-of-function (LOF) mutants are sensitized in the background of glypican and syndecan mutations, and the repulsive guidance and cell migration actions of UNC-5 depend on LON-2/glypican, functionally linking HSPGs with UNC-5 function [41,43]. The UNC-6 EGF2 domain was identified as essential to UNC-5-mediated functions, as the deletion of the EGF2 domain results in complete loss of repulsive guidance and migration functions [33,102], and R→A mutations on the EGF2 domain causes Netrin-1 to lose its UNC5-mediated anti-apoptopic effect [84]. Finally, mutants designed to misfold the IG1 domain of UNC-5 show distal tip cell migration phenotypes and axon guidance effects, although some of the other domain disruptions had similar effects [37]. Our work here establishes a model that provides molecular explanations for the extensive Netrin literature, while enabling future studies using engineered molecules and structural models we have generated, and may serve as a stepping stone towards an atomic-resolution structure of the complete repulsive signaling complex.

2.4 Methods

2.4.1 Protein Expression and Purification for C. elegans Proteins

All *C. elegans* proteins were expressed using the baculoviral expression system and the lepidopteran High Five cell line in Insect-XPRESS (Lonza, cat. no. BELN12-730Q). Baculoviruses were produced using homologous recombination in insect cells by co-transfection with linearized baculoviral DNA and the transfer vector pAcGP67A (BD Biosciences), which carries an N-terminal gp64 signal peptide for secretion. All proteins were tagged C-terminally with a hexahistidine tag for purification. When indicated, some constructs were tagged C-terminally with a BirA recognition sequence (GLNDIFEAQKIEWHE), for facile enzymatic biotinylation, followed by a hexahistidine tag. Biotinylation was performed using the BirA ligase reaction kit (Avidity, cat. no. BirA500).

UNC-5, UNC-6 and UNC-40 constructs of various lengths were purified first with Ni-nitriloacetic acid (NTA) metal-affinity chromatography (QIAGEN, cat. no. 30210) from conditioned media, followed by SEC with either Superose 6 Increase 10/300 (GE Healthcare, cat. no. 29-0915-96) or Superdex 200 Increase 10/300 columns (GE Healthcare, cat. no. 28-9909-44). UNC-5 and UNC-40 are purified in 10 mM HEPES pH 7.2 and 150 mM NaCl (HEPES-buffered saline, HBS), while UNC-6ΔC may exhibit aggregation and stickiness to chromatography resin, as recently recognized by Krahn *et al*.[106] HEPES is N-2-hydroxyethylpiperazine-N'-2-ethanesulfonic acid. We tested numerous buffer conditions in SEC experiments, and observed that UNC-6ΔC (A22-P461) is soluble in a buffer with 500 mM NaCl, and shows excellent SEC elution profiles and complete protein recovery when in 10 mM HEPES pH 7.2, 150 mM NaCl, 100 mM $MgSO_4$ (HBS-MS), presumably as magnesium acting as a chaotrope and sulfate interacting with the heparin-binding site(s) (**Figure 2.2B**).

2.4.2 Yeast Surface Display

All yeast clones and libraries were made using electrically competent EBY100 yeast (Thermo Fisher, cat. no. 83900) [107]. UNC-5 ECD, containing 2 IG and 2 Tsp1 domains, was displayed on yeast via fusion of the C-terminus of UNC-5 ECD to the N-terminus of Aga2. A Myc-tag was included on the C-terminus of UNC-5 for quantification of fusion protein expression via staining with an Alexa Fluor 488-coupled anti-myc (Thermo Fisher, cat. no. MA1-980-A488). To test binding to UNC-6 of yeast displaying UNC-5, an UNC-6 construct lacking the C-terminal NTR domain, known to cause aggregation, and containing a BirA biotin ligase recognition sequence was expressed and purified (UNC-6ΔC). A yeast staining reagent was created by biotinylating UNC-6ΔC and incubating it with Alexa Fluor 647 (Thermo Fisher, cat. no. A20347)-coupled streptavidin.

The UNC-5 ECD display library was created using random error-prone mutagenesis. Separation of yeast populations was done via magnetic-activated cell sorting (Miltenyi Biotec, cat. no. 130-091-051) using either streptavidin (Miltenyi Biotec, cat. no. 130-048-101) or anti-Alexa Fluor 647 microbeads (Miltenyi Biotec, cat. no. 130-091-395). Progress during selections was assessed by UNC-6ΔC binding and monitored using flow cytometry on a BD Accuri C6 flow cytometer.

The yeast library underwent three rounds of selection, performed in decreasing concentrations of heparin from porcine intestinal mucosa (Sigma-Aldrich Heparin Grade I-A, cat. no. H3149). The first round was performed with streptavidin microbeads in 400 nM UNC-6ΔC monomers and 4 μg/ml heparin. The second round was performed with anti-Alexa Fluor 647 microbeads in 125 nM UNC-6ΔC monomers and 0.062 μg/ml heparin. The third round was performed the same as the second round, excluding heparin.

Individual yeast clones (96 total) were isolated after the third selection round. These clones were tested for ability to bind UNC-6ΔC. Of the 96 clones, 8 higher affinity clones were chosen for further analysis. Binding affinities to UNC-6ΔC on yeast without added heparin were measured and the DNA sequence of UNC-5 ECD was sequenced for each clone.
Apparent affinities from protein binding experiments on yeast were measured by plotting control-subtracted mean fluorescence intensities (MFI) on binding isotherms using a one-site, specific binding model in Prism version 9 (GraphPad).

2.4.3 Protein Crystallization

A construct containing the first two IG domains of *C. elegans* UNC-5 with a C-terminal hexahistidine tag was purified as described above and concentrated to 25 mg/ml in HBS. Crystals were grown with the sitting-drop vapor diffusion method, and using microseeding to improve single crystal growth in the crystallant 1.25 M $(NH_4)_2SO_4$, 0.1 M Tris pH 8.5, 0.2 M Li_2SO_4 at 22ºC. Cryoprotection was achieved using a cryoprotectant supplemented with 30% Glycerol by flash-freezing in liquid nitrogen.

UNC-5 IG1-2 with the short heparin fragment dp4 (Iduron, cat. no. HO04; molecular weight, ~1.2 kDa) was crystallized after mixing purified protein with dp4 at a 1:3 molar ratio. Crystallization was achieved with 20 mg/ml UNC-5 using vapor diffusion with the hanging-drop method with the crystallant 4% (v/v) Pentaerythritol ethoxylate (3/4 EO/OH), 0.1 M sodium acetate pH 4.6, 16% (w/v) PEG 8000, 0.2 M NaCl at 22ºC. Crystals were cryoprotected in 0.1 M sodium acetate pH 4.8, 16% PEG 8000, 0.2 M NaCl, 25% ethylene glycol, 60 µg/ml dp4 by flash-freezing in liquid nitrogen.

UNC-6ΔC with a C-terminal hexahistidine tag was purified over Superdex200 10/300 after being mixed with heparin-dp16 (Iduron, cat. no. HO16; molecular weight, ~4.65 kDa) at a

1:1.5 molar ratio in the HBS-MS buffer. Protein was concentrated to 12 mg/ml; we could not check if any dp16 was carried over during purification and concentration. Crystallization was achieved using hanging-drop vapor diffusion with 0.1 M Tris, pH 8.0, 10% (w/v) Polyethylene glycol 8,000 at 22ºC. Crystals were cryoprotected with 0.1 M Tris pH 8, 10% PEG 8,000, 30% glycerol and 0.12 mg/ml dp16. We did not observe any electron density for any heparin-like molecules, as crystal packing appears to be blocking much of our predicted HS-binding site, except for an ordered putative sulfate ion (present at 100 mM in the protein buffer).

2.4.4 Structure Determination by X-ray Crystallography

Crystallographic data were indexed, merged, and scaled using the *XDS* package [108]. Molecular replacement was performed with *PHASER* [109] in the *PHENIX* package [110]. UNC-5 IG1+2 structure was solved using the structure of the human Unc5A ectodomain [79] with domains 1 and 2 as separate molecular replacement models (PDB ID: 4V2A) after homology modeling for the *C. elegans* sequences with *MODELLER* [111]. The structure with heparin-dp4 was determined using our UNC-5 IG1+2 structure as the molecular replacement model. UNC-6ΔC structure was solved using the AlphaFold model as the molecular replacement model [112]. The program *phenix.refine* was used to refine the model structure in reciprocal space [113], and *COOT* was used for model building and correction in real space [114]. Model building and refinement was guided by *MOLPROBITY* tools within *PHENIX* for checking chemical geometry [115].

The diffraction data for the UNC-5 IG1+2 with Heparin-dp4 crystals were highly anisotropic (See **Table 2.1** for details). This dataset was reduced using the XDS package, and then ellipsoidically truncated and anisotropically corrected using the STARANISO server [116]. STARANISO-corrected structure factors were used during refinement.

During model building for our UNC-6 structure, we came across density corresponding to a metal ion previously identified as calcium in other Netrin structures. Since our protein was dissolved in 100 mM $MgSO_4$, it is possible that the calcium ion may or may not have been replaced a magnesium ion during purification; the resolution of the structure does not allow for a definitive identification.

For analysis of sequence and structural features, we heavily used the APBS plugin in PyMOL for electrostatic potential surface calculations [117], and ConSurf for calculating sequence conservation [118]. Isoelectric points and extinction coefficients were calculated using the Protparam server [119].

2.4.5 Surface Plasmon Resonance

A Biacore T200 (GE Healthcare) at 22ºC was used to measure the binding affinities by the equilibrium method, as kinetics of binding was too fast to measure in most occasions. Biotinylated UNC-6ΔC or heparin (Millipore Sigma, cat. no. 375054) was captured on a streptavidin-coated sensor chip (Cytiva, cat. no. 29104992). Analytes for biotinylated UNC-6ΔC included UNC-5 ECD (with and without 5 μg/ml heparin) and heparin. Analytes for biotinylated heparin included UNC-5 ECD and UNC-6ΔC. The running buffer for all SPR experiments was 10 mM HEPES pH 7.2, 150 mM NaCl, 0.05% Tween20, 0.1% bovine serum albumin (BSA), supplemented with either 20 or 50 mM $MgSO_4$ when UNC-6ΔC was an analyte to reduce nonspecific binding. A regeneration step was performed after each injection using 10 mM HEPES pH 7.2, 150 mM NaCl, 0.05% Tween20, 100 mM $MgSO_4$. Titration series were performed once for each mutant/variant, each time with nine to ten measurement points.

Using Biacore evaluation software, the K_D was calculated by fitting the equilibrium data with a 1:1 binding model, whenever binding was observed to nearly saturate. Supplemental

Tables list the K_D values, and the standard error of the fit. With mutants that had very low affinities, saturation of the sensor surface was practically impossible. The SPR experiments were performed by running wild-type and point mutants on the same SPR channel within the same titration series, where we observed no significant loss of activity (i.e. binding response to same analyte) over many runs. This has allowed us to use R_{max} values (SPR response at saturation) from the highest affinity variant as constraints for approximate K_D predictions for weak mutants in Prism (GraphPad version 9). Due to the inability to reach near saturation values, the calculated K_D values at >50 μM should be considered not accurate.

2.4.6 Negative-Staining Electron Microscopy

UNC-5 ECD and UNC-6ΔC were expressed and purified as described above. The proteins were mixed at a 1:1 molar ratio in the presence of 5 μg/mL heparin (~16 kDa) to facilitate complex formation. The protein mixture was then run over a SEC column, Superose 6 Increase 10/300 (GE Healthcare, cat. no. 29-0915-96) in HBS-MS. A fraction from the complex peak was diluted to 8 μg/mL and used for grid preparation. The UNC-6-heparin-UNC-5 sample was pipetted onto 400 mesh carbon-coated copper grids (Electron Microscopy Sciences, CF400-CU) and excess solution was blotted. The sample was stained twice with 1% (weight/volume) uranyl acetate and allowed to fully dry.

The negative-stain grid was imaged at room temperature with a FEI Tecnai F30 electron microscope at 300 kV at the Advanced Electron Microscopy Facility in University of Chicago. A total of 25 images were recorded at 49,000x magnification. From those images, 7812 particles were picked manually with a final pixel size of 3.12 Å. RELION-3.0.8 was used for all image processing [120].

2.4.7 Multi-Angle Light Scattering and Small-angle X-ray Scattering

MALS and SAXS data were collected at the APS beamline 18-ID using a Superose 6 10/300 column on the SEC-MALS-SAXS setup. The protein samples were prepared by mixing UNC-6ΔC, UNC-5 ECD and UNC-40 ECD at molar equal ratios with heparin at 1.5-times the molar equivalent. No heparin was present in the running buffers. Detailed experimental conditions and analysis parameters are listed in **Table 2.4** for MALS and in **Table 2.5** for SAXS. MALS data were collected on a DAWN HELIOS II MALS equipment, with Optilab T-rEX dRI detector (Wyatt Technology). For the UNC-6ΔC–heparin–UNC-5 ECD–UNC-40 ECD complex, we used a with a sheath co-flow strategy (buffer: HBS) to remedy radiation damage [121]. SAXS data were processed in BioXTAS RAW version 2.1.4 [122], using tools from the ATSAS package, version 3.1.3 [123]. For the UNC-6–heparin–UNC-5 data, we used evolving factor analysis (EFA) deconvolution as implemented in RAW to extract scattering from the complex and not the isolated components as a precaution [124]. However, analysis of frames corresponding to just those collected for the major peak gave similar results to those we report using EFA in **Table 2.5**.

2.4.8 Generation of Mutant C. elegans with CRISPR/Cas9 and Phenotypic Analysis of Animals

C. elegans were grown at 20°C on nematode growth media (NGM) plates and fed with Escherichia coli according to standard procedures (79). N2 Bristol was used as the wildtype reference strain. The following additional strains were used in this study: wyIs371 V (TV12310), unc-6(ev400) X; wyIs371 V (TV28935), unc-5(e53) IV; wyIs371 V (TV12715), unc-5(wy1796) VI; wyIs371 V (TV28567), unc-5(I59A S162A D163A) VI; wyIs371 V, and unc-5(R17E R70E I59A S162A D163A) VI; wyIs371 V.

Base pair mutations in unc-5 were generated by microinjections of CRISPR/Cas9 protein complexes in N2 Bristol animals. Genome editing using CRISPR-Cas9 was carried out by

standard protocols (80). Cas9 protein and tracRNA (IDT) were injected at a concentration of 1.525 µM each. crRNAs (IDT) were injected at a concentration of 1.525 µM. Single-stranded DNA repair templates were ordered as oligomers (ThermoFisher) and injected at 6.67 µM. pRF6(rol-6(su1006)) was used as a co-injection marker and selected against after confirmation of a successful genome edit. Confirmation of genome edits was performed by sequencing of F2 animals. The R17E and R70E edits were generated sequentially. The R17E mutation was generated with the following crRNA sequence: CUUAUUUUCAAUGACAUAAC. The R70E mutation was generated with the following crRNA sequence: GAAUCGACGUAGACACAUC. The I159A, S162A, and D163A mutations were generated using the following crRNA sequence: UUAGACUUCCAUCAGAUGCU.

C. elegans hermaphrodites in the late L4 and young adult stages were screened for gonad morphology and distal tip cell migration. Animals were anesthetized using 6 mM Levamisole (Sigma-Aldrich) in M9 buffer and mounted on 4% agarose pads. DIC images were captured using an inverted Zeiss Axio Observer Z1 microscope equipped with a Yokogawa CSU-W1 spinning-disk unit and a Prime 95B Scientific CMOS camera (Photometrics). Slidebook software (3i) was used to control imaging. A water-immersion C-Apochromat 40x 0.9 NA objective was used for all imaging. The same protocol was used on hermaphrodite worms in the L2 stage to screen for motor axon guidance. All images were processed using ImageJ/Fiji (National Institutes of Health) (81).

2.4.9 Expression and Purification of Human Proteins

Our Human Netrin-1s construct comprised residues 25-453, lacking the native N-terminal signal peptide and the C-terminal NTR domain, to enhance expression and solubility. Human draxin was full-length. Human DCC ectodomain was C-terminally truncated at the single-pass

transmembrane segment. Human DCC FN456 (containing Fibronectin type III domain 4 to 6) comprised residues 719-1098, and the shortened splice variant had an internal deletion of residues 819-838. Human UNC5B ectodomain was C-terminally truncated at the single-pass transmembrane segment, and UNC5B IG12 (IG domains 1 and 2) comprised residues 46-246. Mutations were introduced by Quikchange site-directed mutagenesis.

2.4.10 Molecular Assembly Assays (AVEXIS)

Netrin-1s was subcloned with C-terminal fusion to CD4 and a biotinylation target sequence (bait vector) [125]. Other constructs were subcloned with C-terminal fusion to CD4, COMP and β-lactamase (prey vector)[125]. Avexis assays were performed as previously described [126,127]. Briefly, HEK293F cells were used for transient expression, biotinylation of bait protein and secretion into media. Target protein levels were normalized, bait protein was incubated and washed on streptavidin-coated plates (ThermoFisher 436014), prey protein was incubated and washed along with any additives (heparin in **Figure 2.19**) and prey β-lactamase activity was measured by absorbance at 486 nm with nitrocerfin as substrate (EMD Millipore 484400). Experiments were repeated at least three times and included independent sample preparations. Commercial preparations were used for heparin (porcine intestinal mucosa, Sigma H3393). Raw absorbance readings were converted to a fold-change ratio, i.e. experimental absorbance values were divided by the background absorbance values obtained when using HEK293 secretion media in the absence of netrin-1s expression. With additives in AVEXIS (specifically, heparin in **Figure 2.19**), Δfold-change was calculated as the difference in fold-change ratios ± additives. Statistics were performed with a Student's *t*-test.

CHAPTER 3: BEATEN PATHS AND SIDESTEPS

3.1 Introduction

The development of the neuromuscular system is dependent on a microscopic landscape controlled by hundreds of cell-surface and secreted proteins (CSSPs). Neurons rely on CSSPs to guide their movements, trigger cell adhesion, form synaptic connections, and innervate muscles. Uncovering the biochemical mechanisms of CSSPs is crucial to understanding the development of the nervous system and related neurodevelopmental disorders.

Beats and Sides make up two families of CSSPs, with 14 and 8 members, respectively. These proteins control axon branching and muscle innervation in *D. melanogaster*. Improper regulation of these proteins leads to the failure of axons to correctly navigate to their targets. Highly specific Beat-Side interactions are vital for the optic lobe of developing brains and the formation of synaptic connections within the CNS. Although recent studies have uncovered which protein domains are essential for successful Beat-Side binding, it is unknown how these proteins achieve binding specificity with select partners. Understanding these selectivity mechanisms will provide a biochemical window into the complex combinatorial system used by CSSPs to act as signaling receptors and guidance cues.

Here, we chose to work with *D. melanogaster* Beat and Sides, since they have clear axonal guidance phenotypes and come with mutational and functional data. To study the Beat-Side binding interface, we determined the crystal structure of Beat-Vc IG1+2 bound to Side-VI IG1. The first IG domains of both proteins bind, supported by mutational analysis of the Beat-Vc–Side-VI interface with ECIA. To determine if the binding interface was conserved, we modeled the interface onto another Beat-Side pair, Beat-Ia–Side-I, using AlphaFold to predict a Beat-Ia–Side-I structure and sequence alignments to identify key amino acid residues. The predicted

Beat-Ia IG1– Side-I IG1 structure is similar to the crystal structure of Beat-Vc IG1+2–Side-VI IG1 and amino acid residues at the interface are mostly conserved between the two Beat-Side pairs. Mutations to the conserved residues at the Beat-Ia–Side-I interface disrupted binding, detected through ECIA, suggesting the binding interface is conserved.

3.2 Results

3.2.1 The first IG domains of Side-VI and Beat-Vc bind

To gain insight into how Beats and Sides interact, we aimed to determine the crystal structure of a Beat-Side pair from *D. melanogaster*. We successfully crystallized the extracellular region of Beat-Vc, containing 2 IG domains, bound to the first IG domain of Side-VI to 3.9 Å resolution, the first known structure of a Beat-Side pair (**Figure 3.1A**). The structure revealed two potential binding interfaces. Site 1 is between Beat-Vc IG1 and Side-VI IG1 and site 2 is between Beat-Vc IG2 and Side-IG1 (**Figure 3.1B-C**). To investigate if one or both interfaces were physiologically relevant, I engineered single amino acid substitutions to break binding at the contact sites and used ECIA to screen mutations for elimination or reduction of binding. All but one mutation (Beat-Vc R121A) in contact site 1 eliminate binding while mutations in contact site 2 largely do not impact binding (**Figure 3.1D**). Therefore, site 1 is most likely the binding interface while site 2 is a crystal artifact.

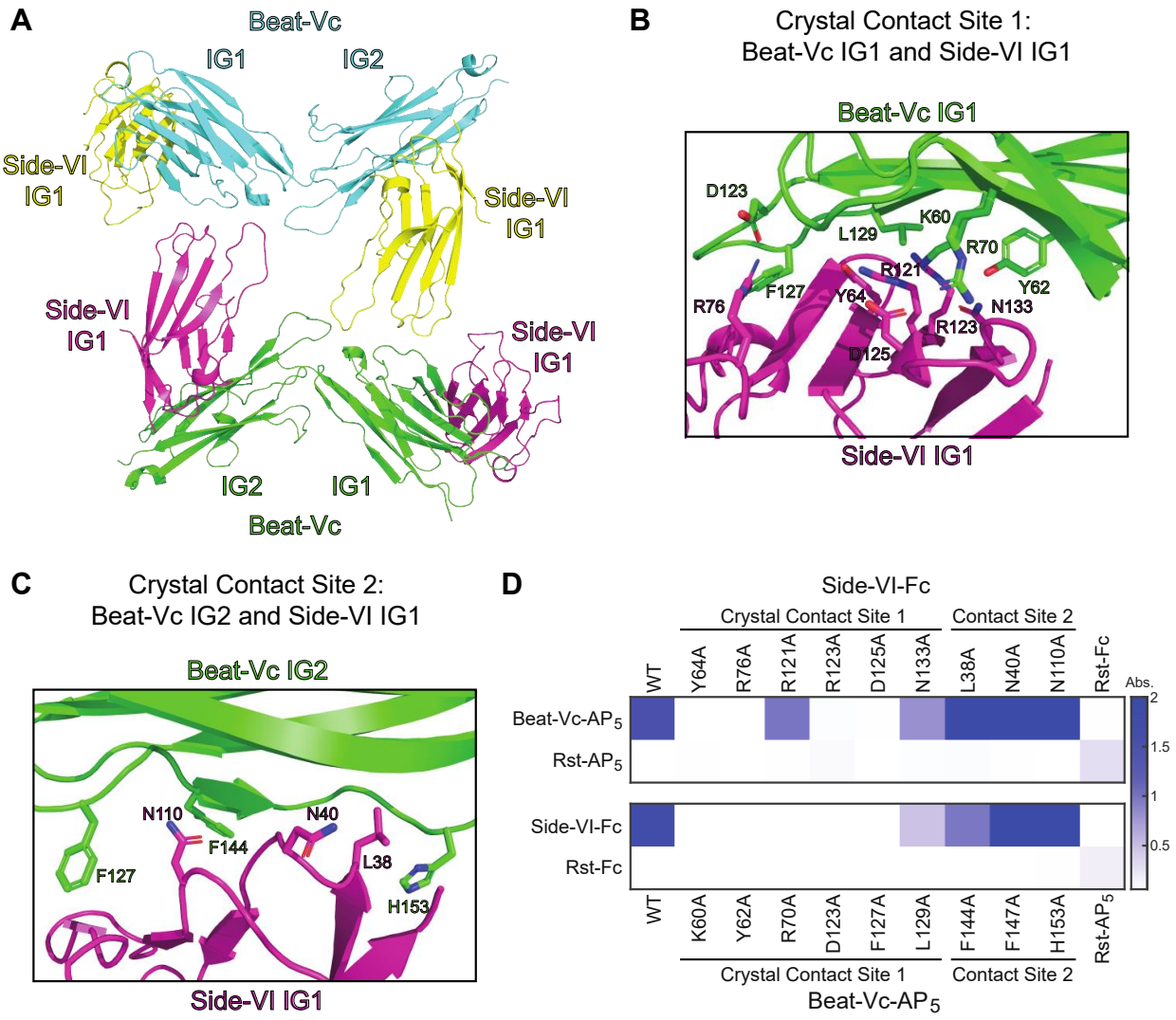

Figure 3.1. Crystal structure of the extracellular region of Beat-Vc and IG1 of Side-VI reveals a binding interface (panels A-C contain data from Dr. Engin Özkan and and Dr. Agnieszka Olechwier).

A. Crystal structure of two molecules of Beat-Vc ECD and four molecules of Side-VI IG1. **B,C.** Close look at crystal contact sites. Site 1 (C) is between Beat-Vc IG1 and Side-VI IG1 and site 2 (D) is between Beat-Vc IG2 and Side-IG1. **D.** ECIA measurements of mutations designed to break the binding interfaces at both crystal contact sites on Beat-Vc and Side-VI. Panels A-C contain data from a crystal structure determined by Dr. Engin Özkan and Dr. Agnieszka Olechwier.

3.2.2 The Beat-Side binding interface is conserved

Structural information is currently limited to the Beat-VcSide-VI pair. To test if the binding interface is conserved between different Beat-Side pairs, we engineered amino acid substitutions that disrupted Beat-Vc–Side-VI binding onto Beat-Ia–Side-I. Beat-Ia–Side-I binding is relatively weak with a K_D of ~3 μM as measured using biotinylated Side-I captured on an SPR chip (**Figure 3.2A-B**). Despite affinity in the micromolar range, the Beat-Ia–Side-I complex is stable and can be isolated using SEC (**Figure 3.2C**). In addition, Beat-Ia–Side-I binding can be observed with BPIA[64] and ECIA[63].

Using *Alphafold-multimer* (version 2.3.0) via the Colabfold implementation, we obtained a model for the Beat-Ia–Side-I complex[92,93]. The predicted Beat-Ia–Side-I structure is similar to our Beat-Vc–Side-VI crystal structure, with the same binding interface between the first IG domains (**Figure 3.3A**). Residues that play a role in binding are largely conserved (**Figure 3.3B**). Only one residue, Side-VI F129 and Side-I Y64, is not conserved. We again used ECIA to screen for the binding of mutant Beat-Ia and Side-I constructs containing 1-3 amino acid substitutions (**Figure 3.3C**). In addition to Beat-Ia, Side-I also interacts with Beat-Ic, -IIa, and -IIb[63,64]. These Beats were included in the ECIA to determine if Side-I mutations affect binding to other Beat partners. ECIA revealed that Beat-Ia and Side-I mutants eliminated or reduced binding to each other. The majority of Side-I mutants retain their ability to bind Beat-IIa and -IIb. Side-I R190A R192A D194A triple mutant shows a reduction in binding to Beat-IIa and -IIb, although not as significant as the loss of binding to Beat-Ia (**Figure 3.3C**). Beat-Ic–Side-I binding was not measurable on the ECIA, a result consistent with previously published efforts[63]. These results suggest that the Beat-Side binding interface is conserved and determines the specificity to its binding partner.

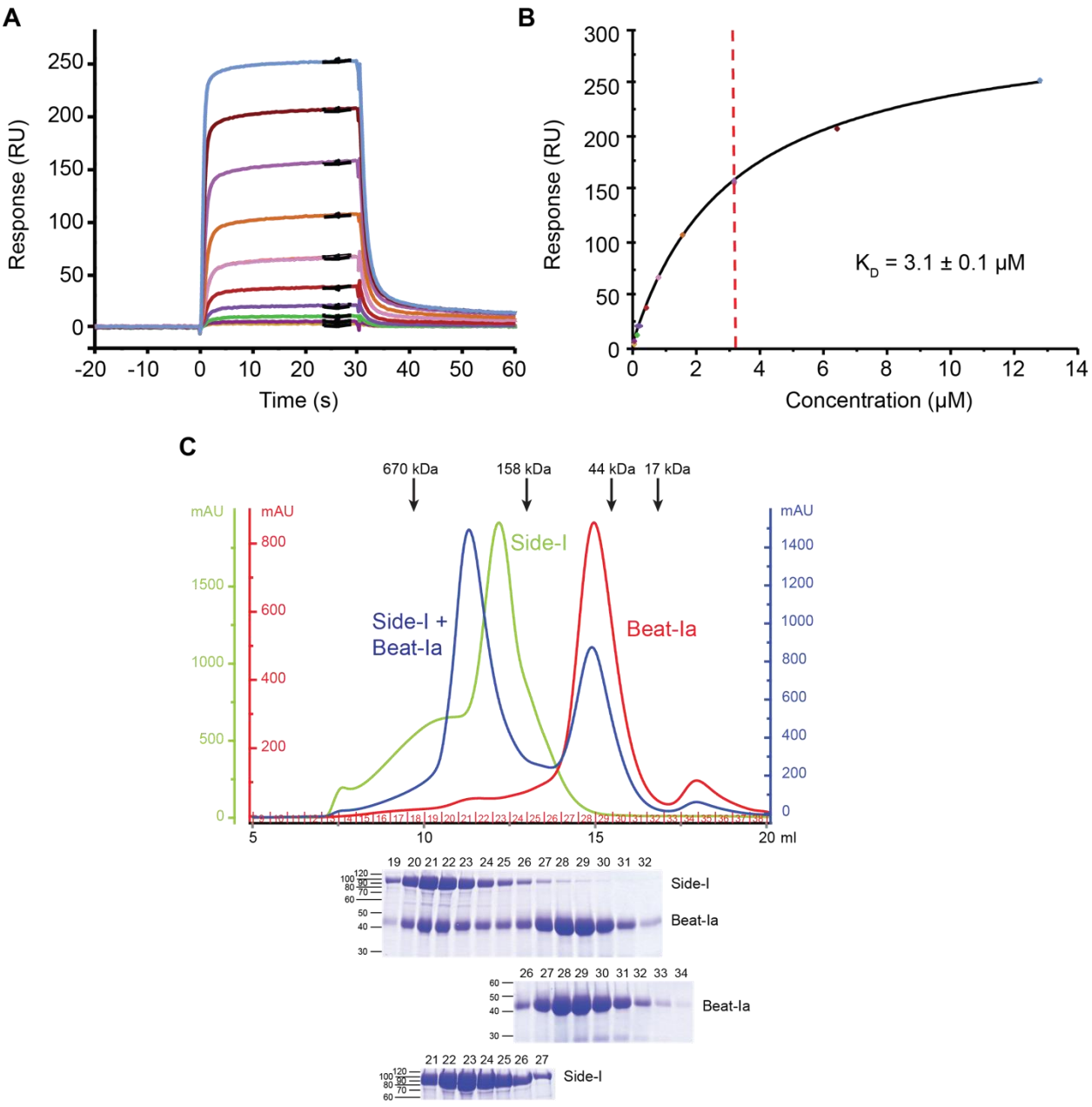

Figure 3.2. Beat-Ia and Side-I form a stable complex (data from Dr. Engin Özkan).

A,B. Sensograms (A) and binding isotherms (B) for SPR experiments testing the interaction of Beat-Ia and biotinylated Side-I. **C.** Size-exclusion chromatography of Beat-Ia and Side-I. Beat-Ia (red), Side-I (green), and a mixture of Beat-Ia and Side-I (blue) were injected on a Superdex 200 10/300 column equilibrated with 10 mM HEPES pH 7.2, 500 mM NaCl, and 10% glycerol. Coomassie-stained SDS-polyacrylamide gels for the individual and mixture runs are placed under the chromatograms.

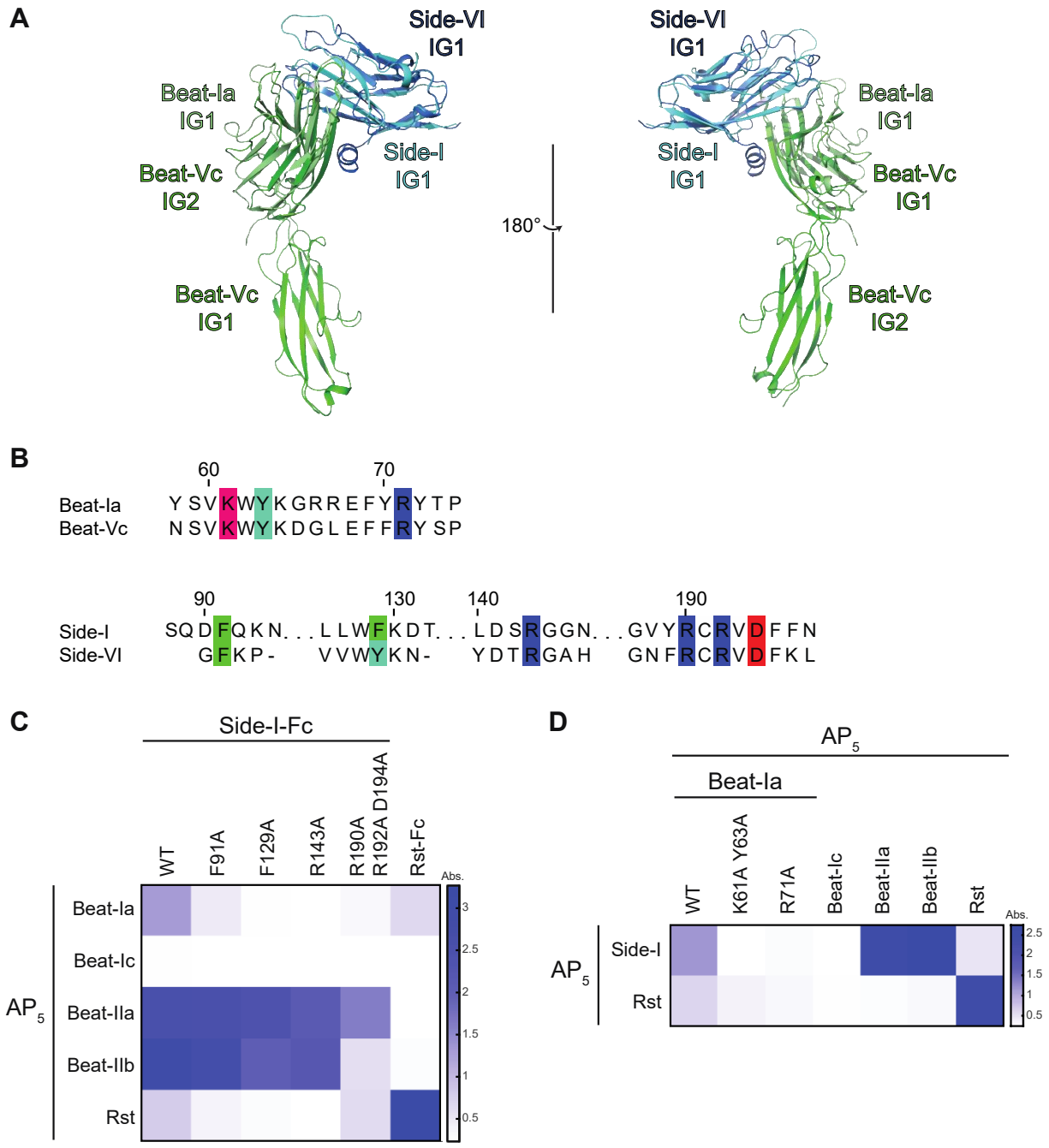

Figure 3.3. The binding interface between Beats and Sides is conserved (panel A contains data from Dr. Engin Özkan and Dr. Agnieszka Olechwier).

Continued on next page.

Figure 3.3 continued. A. Superposition of the crystal structure of Beat-Vc ECD (dark green) and Side-VI IG1 (dark blue) and the AlphaFold structure of Beat-Ia IG1 (light green) and Side-I IG1 (light blue). **B.** Sequence alignments of Beat-Vc and -Ia and Side-VI and -I. Highlighted residues are from crystal contact site 1. Only one residue, Side-VI F129 and Side-I Y64, is not conserved. **C.** ECIA measurements of interactions between Side-I with mutations to crystal contact site 1 and Beat-Ia, Beat-Ic, Beat-IIa, and Beat-IIb. **D.** ECIA measurements of interactions between Beat-Ia with mutations to crystal contact site 1, Beat-Ic, Beat-IIa, and Beat-IIb and Side-I. In C and D, Rst acts as both a negative and positive control. Rst does not bind to Beats and Sides but binds strongly to itself. Panel A contains data from a crystal structure determined by Dr. Engin Özkan and Dr. Agnieszka Olechwier.

3.3 Discussion

In *D. melanogaster,* Beat-expressing motor neurons are directed towards Side-expressing sensory neurons and muscle cells. In *beat* and *side* mutant animals, motor axons fail to branch off at designated choice points, remaining fasciculated or stalling, and do not progress into the periphery. The functions of Beats and Sides in axon guidance have been incompletely documented, partially due to the lack of structural information. In this study, we determined how Beats and Sides bind with each other and show that their binding interface is conserved.

We determined the crystal structure of Beat-Vc IG1+2 bound to Side-VI IG1. The first IG domains of both proteins bind, supported by mutational analysis of the Beat-Vc–Side-VI interface with ECIA. The interaction is consistent with other cell surface proteins such as (1) defective proboscis extension response proteins (Dprs) and Dpr-interacting proteins (DIPs), (2) synaptogenesis abnormal-1 and -2 proteins (SYG-1 and -2), and (3) junctional adhesion molecule–like protein (JAML) and coxsackievirus and adenovirus receptor (CAR)[128–131]. The prevalence of this type of interaction, specifically in members of the IgSF, suggests it was evolutionarily selected for to aid synapse formation. The binding interface between Beat-Vc and Side-VI contains numerous polar amino acid residues, in contrast to Dpr-DIP interfaces that are hydrophobic and rely on shape complementarity[128]. Salt bridges or hydrogen bonds likely play a

role in Beat-Side complex formation. In *D. melanogaster,* neither Beat-IaΔIG1 and Side nor Beat-Ia and SideΔIG1 localized together, suggesting the first domains are crucial for binding[73]. Our crystal structure does not contain the full extracellular region of Side-VI. It is possible that other Side-VI domains besides IG1, IG2-5 and FN3, bind to Beat-Vc *in vivo* or play a physiologically relevant role, such as oligomerization.

We modeled the binding interface onto another Beat-Side pair, Beat-Ia-Side-I, using sequence alignments to identify important amino acid residues and AlphaFold to predict a Beat-Ia-Side-I structure to ascertain whether the binding contact was conserved. The predicted Beat-Ia IG1- Side-I IG1 structure resembles the Beat-Vc IG1+2-Side-VI IG1 crystal structure, and the majority of the amino acid residues at the interface are the same for the two Beat-Side pairs. Only one residue, Side-VI F129 and Side-I Y64, is not conserved. Changes to the conserved residues at the Beat-Ia-Side-I interface disrupted binding, indicating the conservation of the binding interface. While Side-I mutants eliminated or reduced binding to Beat-Ia, they predominantly retained their ability to bind Beat-IIa and -IIb; Beat-Ic-binding was not detectable using ECIA even for wild-type Side-I. It is possible that the difference in ECIA signal strength of Side-I binding to Beat-Ia versus Beat-IIa and -IIb biases the assay.

Our work here provides molecular and structural details of Beat-Side complexes, enabling future studies using engineered Beats and Sides *in vivo* to observe defects in axon guidance.

3.4 Methods

3.4.1 Protein Expression and Purification for Size Exclusion Chromatography and Surface Plasmon Resonance

D. melanogaster proteins were expressed using the baculoviral expression system and the lepidopteran High Five cell line in Insect-XPRESS (Lonza, cat. no. BELN12-730Q). Baculoviruses were produced using homologous recombination in insect cells by co-transfection with linearized baculoviral DNA and the transfer vector pAcGP67A (BD Biosciences), which carries an N-terminal gp64 signal peptide for secretion. All proteins were tagged C-terminally with a hexahistidine tag for purification. When indicated, some constructs were tagged C-terminally with a BirA recognition sequence (GLNDIFEAQKIEWHE), for facile enzymatic biotinylation, followed by a hexahistidine tag. Biotinylation was performed using the BirA ligase reaction kit (Avidity, cat. no. BirA500).

Proteins were purified first with Ni-NTA metal-affinity chromatography (QIAGEN, cat. no. 30210) from conditioned media, followed by SEC with Superdex 200 Increase 10/300 columns (GE Healthcare, cat. no. 28-9909-44). The buffer components were 10 mM HEPES pH 7.2, 500 mM NaCl, and 10% glycerol. The high concentration of NaCl and addition of glycerol was used to improve protein quality by limiting aggregation of Side constructs. Sides exhibit disulfide-linked aggregates. Rerunning the non-aggregated portion using SEC reduces aggregation significantly in the sample. The co-infection of Side-I and Beat-Ia did not show aggregation of Side-I, suggesting Beat-Ia helps stabilize Side-I. In addition, this buffer improved the yield of Beat constructs. Beats did not exhibit any aggregation, although their expression tended to be poor. In some cases, protease inhibitor cocktail and/or phenylmethylsulfonyl fluoride (PMSF) were included as well to prevent degradation.

3.4.2 Surface Plasmon Resonance

SPR experiments were conducted by Dr. Engin Özkan. A Biacore T200 (GE Healthcare) at 22ºC was used to measure the binding affinities. Biotinylated Side was captured on a streptavidin-coated sensor chip (Cytiva, cat. no. 29104992) and the analyte was Beat-Ia. The running buffer components were 10 mM HEPES pH 7.2, 500 mM NaCl, and 10% glycerol. Titration series contained 10 measurement points. Using Biacore evaluation software, the K_D was calculated by fitting the equilibrium data with a 1:1 binding model.

3.4.3 Protein Crystallization and Structure Determination by X-ray Crystallography

Constructs of *D. melanogaster* Beat-Vc IG1+2 and *D. melanogaster* Side-VI IG1 were used for the crystal structure shown in **Figure 3.1A-C** and **Figure 3.3A**. Dr. Agnieszka Olechwier performed protein purification, crystal optimization, and X-ray diffraction data collection. Dr. Engin Özkan and Dr. Agnieszka Olechwier solved and refined the crystal structure.

3.4.4 Protein Expression for Extracellular Interactome Assay

Proteins were expressed in Drosophila Schneider 2 (S2) cells in Schneider's medium (Thermo Fisher, cat. no. 21720001) supplemented with 10% Fetal Bovine Serum, 50 units/ml Penicillin, 50 µg/ml Streptomycin, and 2 mM L-Glutamine. Transfections were performed with Cellfectin II Reagent (Thermo Fisher, cat. no. 10362100), following the manufacturer's protocol. When applicable, protein expressed was induced with 0.8 mM $CuSO_4$ 12-18 hours after cells were transfected. Proteins were collected 3-4 days after transfection by centrifuging samples at 2,000 rpm for 5 minutes and collecting the supernatants.

3.4.5 Extracellular Interactome Assay

Protein A-coated plates were washed with Phosphate-Buffered Saline (PBS) with 0.1% Tween20 (PBST). To capture bait proteins, 100 µl of medium with secreted Fc-tagged bait proteins was added to each well for overnight incubation while shaking at 4°C. Plates were blocked with PBS with 1% BSA. Blocking was performed at room temperature for 3 hours while shaking. Plates were then washed with PBS with 1 mM $CaCl_2$, 1 mM $MgCl_2$, and 0.1% BSA. Next, for prey binding, 100 µl of medium with secreted AP-tagged prey proteins was added to each well and incubated at room temperature for 3 hours while shaking. Another wash with PBS with 1 mM $CaCl_2$, 1 mM $MgCl_2$, and 0.1% BSA was performed. Lastly, 100 µl of BluePhos Phosphatase Substrate (Seracare, cat. no. 5120-0059) was added to each well. To assess bait-prey binding, absorbance at 650 nm was measured with a BioTek Synergy H1 Plate Reader and plates were imaged with an Epson scanner. The absorbance readings were analyzed in MATLAB (MathWorks).

CHAPTER 4: CONCLUSIONS AND FUTURE DIRECTIONS

4.1 Future directions in Netrin–Receptor structural biology

Structural knowledge is currently limited to the mammalian homologs of the UNC-40-UNC-6 complex[132–134], but structural and mechanistic models on how UNC-5–UNC-6 and UNC-6–heparin–UNC-5 complexes form and signal are sorely lacking. Elucidating the interaction between these two proteins is also crucial due to the pathophysiological relevance of the complex, playing key roles in tumorigenesis and tissue morphogenesis. With this knowledge, improved anti-netrin-1or anti-UNC5 antibodies can be designed to block the interaction of Netrin with UNC-5, therefore manipulating neuronal circuitry and cell survival; this creation would be a powerful therapeutic agent.

Previous efforts to structurally examine the complex of the UNC-5 receptor and its ligand UNC-6 have been unsuccessful. Attempts for high-resolution structural data of the UNC-5–UNC-6 and UNC-6–heparin–UNC-5 complexes are limited to separate structures of UNC-5[36] (**Figure 2.3A-E**, **Figure 2.4B-F**) and UNC-6[84,105,106] (**Figure 2.14A-B**), with or without a GAG, HSPG, or heparin mimic bound. The low affinity between the two proteins, dissociation constant in micromolar range determined through SPR (**Figure 2.7A**), impedes the ability to use both x-ray crystallography and cryogenic electron microscopy (cryo-EM).

The interaction between UNC-6 and its receptors is facilitated by multivalent heparin molecules[135]. However, structural biology of the ternary UNC-6–heparin–UNC-5 complex is complicated by the conformational and chemical heterogeneity of heparin. Heparin does not have a consensus binding sequence, making predictions of protein interactions difficult. To date, less than a hundred protein-heparin complexes have been solved, representing a fraction of known protein-heparin complexes[136,137]. The lack of known protein-heparin structures is

paradoxical considering the diverse and numerous proteins within the ECM that require heparin for function and regulation[138]. As more heparin-binding proteins are discovered, characterization of the molecular and structural properties of these proteins is a growing need.

We present a model of an UNC-6–heparin–UNC-5 complex that is very large yet well-ordered. Negative-staining electron microscopy (**Figure 2.11E** and **Figure 2.13A**) and SAXS (**Figure 2.11G**, **Figure 2.13B-F** and **Table 2.5**) show a large, globular complex, and not long or thin chains. Given inherent flexibility of the heparin chain, the multi-domain nature of the proteins, including the flexible UNC-5 ectodomain (**Figure 2.4A**) and their elongated structures, this is not expected, and indicates that the UNC-6–heparin–UNC-5 complex has a stable, ordered geometry and defined structure, which may be important for a signaling-competent conformation on the cell surface.

The negative stained images of the ternary complex showed a relatively monodisperse sample with no signs of aggregation (**Figure 2.13A**). A monodisperse sample is critical for image processing as size and conformational variation leads to poor particle alignment and averaging[139]. The 2D class averages of the negative stain, showing a large complex of unknown oligomeric state, using the RELION computer program (**Figure 2.11E**)[140]. Overall, the negative stain data indicated sample quality was sufficient to move onto more labor intensive cryo-EM screening. Cryo-EM can produce high resolution structures that are not accessible with negative staining. Due to the chemical and conformational heterogeneity of heparin, I chose to use cryo-EM over crystallography since it is a single-particle method that can potentially distinguish among heterogeneous particles. The ternary complex was frozen on carbon-copper grids using a FEI Vitrobot, a plunge-freezing device, and imaged using a Titan Krios microscope. The screen revealed vitreous ice, an important result since non-vitreous, crystalline ice formation would

compromise the integrity of the sample, leading to poor image quality[141]. As seen in the negative stain, the sample is monodisperse. Particles appear fully imbedded in ice and evenly distributed.

Using this preliminary data, I collected a full cryo-EM dataset at the National Cryo-EM Facility, funded through the National Institutes of Health's National Cancer Institute, and at the University of Chicago's state-of-the-art cryo-EM facility. Heparin complicates structural determination due to its heterogeneity; to combat this, I purified the ternary complex with low and ultra-low molecular weight heparins (~2-5 kDa) to use in place of the unfractionated heparin (from porcine mucosa, ~16 kDa) used in the negative-stain and cryo-EM screen. These smaller heparins are more homogenous than unfractionated heparin. There are published protein-heparin structures using a similar approach[142,143], including our crystal structure of UNC-5-dp4 (**Figure 2.3C-E**, **Figure 2.4B-F)**.

Cryo-EM datasets of UNC-6–dp10–UNC-5 (dp10 MW = 3 kDa) and UNC-6–dp16–UNC-5 (dp16 MW = 4.65 kDa) complexes did not yield meaningful 2D or 3D class averages. SEC runs revealed shorter heparin chains are less effective in complex formation compared to unfractionated heparin, although small complex peaks can be isolated (**Figure 2.12B**). Unfractionated heparin from porcine mucosa is approximately 50-60 saccharides in length. Most likely, a heparin oligomer of intermediate size is needed for effective complex formation while providing a more homogenous sample. The ideal heparin oligomer would be long enough to bridge UNC-5 and UNC-6 with little to no overhang. Finding this heparin oligomer will take a methodical approach of testing numerous heparin length for complex formation over SEC and negative-stain or cryo-EM screening. Another option is to use a larger than necessary heparin oligomer and treat the resulting UNC-6–heparin–UNC-5 complex after purification with a

heparin lyase enzyme, also called heparinase[144]. Furthermore, a homogenous UNC-6–heparin oligomer–UNC-5 sample could be used for X-ray crystallography.

UNC-6–UNC-5 and UNC-6 crystals can also be soaked with a heparin oligomer solution, In this strategy, protein crystals are briefly placed in a solution of ligand, allowing the ligand to move through channels between protein molecules. Soaking takes place for hours to days in order to ensure ligand binding saturation. Cocrystallization tends to be more reliable in capturing correct binding interfaces compared to crystal soaking; however, crystal soaking is easier and less time consuming[145]. To date, I have not successfully produced UNC-6–UNC-5 crystals; an additive screen may be beneficial in this case. Soaking crystals requires ligand molecules small enough to maneuver through the channels[145]. Attempts to soak UNC-5 crystals with heparin oligomers and heparin mimics, such as sucrose octasulfate, did not yield well-diffracting crystals. The length of soaking time may need to be increased.

4.2 Molecular dissection of Beat-Side complexes and function: Prospective Outlook

Only Beat-Ia, -Ic, -IV and -Va/b/c interactions have been studied with their respective Side-binding partners by a quantitative method such as SPR. The affinities of the small number of Beat-Side pairs investigated range in strength. The affinities differ by ~100-fold: Beat-Ic and Side-III have a K_D of 63 μM, and Beat-Va and Side-VI have a K_D of 0.76 μM[64]. It is poorly understood why different Beat-Side pairs have strong or weak binding affinities and what the consequence *in vivo* for the binding affinity strength is. Other CSSP interactomes formed by paralogs also exhibit a range of affinities, such as Dprs and DIPs[63,128]. In *C. elegans*, we showed how a ~26-fold reduction in UNC-5-heparin binding (**Figure 2.9A**, **Figure 2.10A**, **Table 2.3**) affected distal tip cell migration and axon guidance. Netrin-dependent UNC-5 function requires the heparin-binding activity of UNC-5 during distal tip cell migration, as this is likely necessary for a stable, oligomeric, and functional UNC-6–UNC-5 complex (**Figure 2.16A-C**). However, UNC-5-mediated guidance of axon commissures is not dependent on the UNC-5-heparin interaction (**Figure 2.16D-F**). These findings collectively suggest that UNC-5-UNC-6-HS interactions control some repulsive guidance *in vivo* and that neurons may have compensatory mechanisms to compensate for reduced UNC-5-UNC-6-HS binding. This work demonstrates that physiological outcomes in organisms are significantly influenced by the varying affinities that CSSPs exhibit. The differences in their affinities for binding partners or substrates impact the specificity and strength of molecular interactions, ultimately dictating biological processes.

Despite efforts to deorphanize the Beat-Side interactome through ECIA and BPIA, a third of the network lacks known binding partners. Plus, few affinity measurements of Beat-Side pairs have been conducted. To screen for binding partners and obtain the range of affinities in the Beat-Side interactome, SPR of all Beats against all Sides should be performed. To mimic

physiological conditions, the constructs should contain the full extracellular region of the proteins, and BirA recognition sequences should be added on the C-terminus for SPR ligands, where the transmembrane region is located natively. To aid an SPR experiment of this scale, Beats and Sides can be frozen ahead of time in a buffer of 10 mM HEPES pH 7.2, 500 mM NaCl, and 10% glycerol. Once affinities for Beat-Side pairs are measured, variants with complete loss, partial loss, or improved affinity can be engineered. Decreasing affinity is a fairly straightforward process and can be achieved by utilizing the existing Beat-Vc–Side-VI structure and sequence alignments. Increasing affinity is more challenging and might require the use of directed evolution, such as yeast surface display. These mutants can then be used in *D. melanogaster* to observe the effects on axon fasciculation and pathfinding.

Based on unpublished SEC and MALS data, Side-I runs as both a monomer and a dimer. *In vivo*, dimeric Side-I could lead to the dimerization of its Beat binding partners, Beat-Ia, Ic, IIa, and IIb. Oligomerization of Beat-Side complexes could play a critical role in branching and axon growth. SEC profiles of the Beat-Ia–Side-I complex looked gaussian-shaped and well-defined, but MALS data was difficult to parse. Side-I aggregates significantly and has different oligomeric states, undergoing a monomer-dimer equilibrium. The addition of Beat-Ia only further complicated matters. This experiment was performed with the ECD of Side-I. To determine which domain of Side-I is responsible for dimerization, Side-I can be truncated to varying lengths. Truncation might also prevent excessive disulfide-mediated aggregation if cysteines are removed. Dimerization of Side-I can be assessed over SEC and confirmed through a method for molecular size determination, like analytical ultracentrifugation or MALS. Side-I truncations can also be tested to determine if their affinity to Beat-Ia is retained, either through SPR binding affinity measurements or Beat-Ia–Side-I complex formation over SEC. A Side-I

construct that cannot dimerize but has wild-type affinity to Beat-Ia can be tested *in vivo* for axon guidance defects. Another approach is to crystallize a Side by itself to see the dimerization interface.

Beat-Ia and Side-I amino acid substitutions could affect binding to unidentified ligands. ECIA is performed with conditioned cell media and does not use pure protein samples. Therefore, other binding partners may be present in this assay. To address this concern, an ionic pair of Beat-Ia and Side-I mutants may be designed at the binding interface, such as aspartic acid and arginine. In this experiment, single Beat-Ia or Side-I mutants should not rescue the axon guidance phenotype in vivo and should reduce binding using ECIA. The double mutant, on the other hand, should exhibit wild-type axon guidance and ECIA signal, rescuing the defect and showing that the phenotype was caused by loss of Beat-Ia–Side-I binding.

BIBLIOGRAPHY

1. Comer, J. D., Alvarez, S., Butler, S. J. & Kaltschmidt, J. A. Commissural axon guidance in the developing spinal cord: from Cajal to the present day. *Neural Development* **14**, 9 (2019).

2. Esslinger, C. *et al.* Neural mechanisms of a genome-wide supported psychosis variant. *Science* **324**, 605 (2009).

3. Supekar, K. *et al.* Brain hyperconnectivity in children with autism and its links to social deficits. *Cell Rep* **5**, 738–747 (2013).

4. Khan, S. *et al.* Local and long-range functional connectivity is reduced in concert in autism spectrum disorders. *Proc Natl Acad Sci U S A* **110**, 3107–3112 (2013).

5. Hickman, R. A., O'Shea, S. A., Mehler, M. F. & Chung, W. K. Neurogenetic disorders across the lifespan: from aberrant development to degeneration. *Nat Rev Neurol* **18**, 117–124 (2022).

6. Calhoun, V. D. *et al.* Exploring the Psychosis Functional Connectome: Aberrant Intrinsic Networks in Schizophrenia and Bipolar Disorder. *Front Psychiatry* **2**, 75 (2012).

7. Mitchell, K. J. The genetics of neurodevelopmental disease. *Curr Opin Neurobiol* **21**, 197–203 (2011).

8. Travis, J. Wiring the Nervous System. *Science* **266**, 568–570 (1994).

9. Ramón y Cajal, S. La rétine des vertébrés. *La Cellule* 121–255 (1892).

10. Sperry, R. W. Chemoaffinity in the orderly growth of nerve fiber patterns and connections. *Proc Natl Acad Sci U S A* **50**, 703–710 (1963).

11. Hedgecock, E. M., Culotti, J. G. & Hall, D. H. The unc-5, unc-6, and unc-40 genes guide circumferential migrations of pioneer axons and mesodermal cells on the epidermis in C. elegans. *Neuron* **4**, 61–85 (1990).

12. Boyer, N. P. & Gupton, S. L. Revisiting Netrin-1: One Who Guides (Axons). *Front Cell Neurosci* **12**, 221 (2018).

13. Vulliemoz, S., Raineteau, O. & Jabaudon, D. Reaching beyond the midline: why are human brains cross wired? *The Lancet Neurology* **4**, 87–99 (2005).

14. Thomas, J. B. Axon guidance: Crossing the midline. *Current Biology* **8**, R102–R104 (1998).

15. Kolodkin, A. L. & Tessier-Lavigne, M. Mechanisms and molecules of neuronal wiring: a primer. *Cold Spring Harb Perspect Biol* **3**, (2011).

16. Zang, Y., Chaudhari, K. & Bashaw, G. J. New insights into the molecular mechanisms of axon guidance receptor regulation and signaling. *Curr Top Dev Biol* **142**, 147–196 (2021).

17. Cortés, E., Pak, J. S. & Özkan, E. Structure and evolution of neuronal wiring receptors and ligands. *Dev Dyn* **252**, 27–60 (2023).

18. Luo, L. *Principles of Neurobiology*. (Garland Science, Taylor & Francis Group, 2015).

19. Stoeckli, E. Where does axon guidance lead us? *F1000Res* **6**, 78 (2017).

20. de Ramon Francàs, G., Zuñiga, N. R. & Stoeckli, E. T. The spinal cord shows the way – How axons navigate intermediate targets. *Developmental Biology* **432**, 43–52 (2017).

21. Neuhaus-Follini, A. & Bashaw, G. J. Crossing the embryonic midline: molecular mechanisms regulating axon responsiveness at an intermediate target. *Wiley Interdiscip Rev Dev Biol* **4**, 377–389 (2015).

22. Kennedy, T. E. Cellular mechanisms of netrin function: Long-range and short-range actions. *Biochem. Cell Biol.* **78**, 569–575 (2000).

23. Ko, S. Y., Dass, C. R. & Nurgali, K. Netrin-1 in the developing enteric nervous system and colorectal cancer. *Trends Mol Med* **18**, 544–554 (2012).

24. Brisset, M., Grandin, M., Bernet, A., Mehlen, P. & Hollande, F. Dependence receptors: new targets for cancer therapy. *EMBO Mol Med* **13**, e14495 (2021).

25. Ramkhelawon, B. *et al.* Netrin-1 promotes adipose tissue macrophage retention and insulin resistance in obesity. *Nat Med* **20**, 377–384 (2014).

26. Serafini, T. *et al.* The netrins define a family of axon outgrowth-promoting proteins homologous to *C. elegans* UNC-6. *Cell* **78**, 409–424 (1994).

27. Rajasekharan, S. & Kennedy, T. E. The netrin protein family. *Genome Biol* **10**, 239–239 (2009).

28. Feinstein, J. & Ramkhelawon, B. Netrins & Semaphorins: Novel regulators of the immune response. *Biochimica et Biophysica Acta (BBA) - Molecular Basis of Disease* **1863**, 3183–3189 (2017).

29. Sun, K. L. W., Correia, J. P. & Kennedy, T. E. Netrins: versatile extracellular cues with diverse functions. *Development* **138**, 2153 (2011).

30. Ly, A. *et al.* DSCAM is a netrin receptor that collaborates with DCC in mediating turning responses to netrin-1. *Cell* **133**, 1241–1254 (2008).

31. Liu, G. *et al.* DSCAM functions as a netrin receptor in commissural axon pathfinding. *Proceedings of the National Academy of Sciences* **106**, 2951–2956 (2009).

32. Purohit, A. A. *et al.* Down syndrome cell adhesion molecule (DSCAM) associates with uncoordinated-5C (UNC5C) in netrin-1-mediated growth cone collapse. *J Biol Chem* **287**, 27126–27138 (2012).

33. Hedgecock, E. M., Culotti, J. G. & Hall, D. H. The *unc-5*, *unc-6*, and *unc-40* genes guide circumferential migrations of pioneer axons and mesodermal cells on the epidermis in C. elegans. *Neuron* **4**, 61–85 (1990).

34. Finci, L., Zhang, Y., Meijers, R. & Wang, J.-H. Signaling mechanism of the netrin-1 receptor DCC in axon guidance. *Prog Biophys Mol Biol* **118**, 153–160 (2015).

35. Meijers, R., Smock, R. G., Zhang, Y. & Wang, J.-H. Netrin Synergizes Signaling and Adhesion through DCC. *Trends Biochem Sci* **45**, 6–12 (2020).

36. Akkermans, O. *et al.* GPC3-Unc5 receptor complex structure and role in cell migration. *Cell* **185**, 3931-3949.e26 (2022).

37. Killeen, M. *et al.* UNC-5 function requires phosphorylation of cytoplasmic tyrosine 482, but its UNC-40-independent functions also require a region between the ZU-5 and death domains. *Dev Biol* **251**, 348–366 (2002).

38. Agarwala, K. L., Nakamura, S., Tsutsumi, Y. & Yamakawa, K. Down syndrome cell adhesion molecule DSCAM mediates homophilic intercellular adhesion. *Molecular Brain Research* **79**, 118–126 (2000).

39. Smock, R. G. & Meijers, R. Roles of glycosaminoglycans as regulators of ligand/receptor complexes. *Open Biol* **8**, (2018).

40. Matsumoto, Y., Irie, F., Inatani, M., Tessier-Lavigne, M. & Yamaguchi, Y. Netrin-1/DCC signaling in commissural axon guidance requires cell-autonomous expression of heparan sulfate. *J Neurosci* **27**, 4342–4350 (2007).

41. Gysi, S., Rhiner, C., Flibotte, S., Moerman, D. G. & Hengartner, M. O. A network of HSPG core proteins and HS modifying enzymes regulates netrin-dependent guidance of D-type motor neurons in *Caenorhabditis elegans*. *PLoS One* **8**, e74908 (2013).

42. Merz, D. C., Alves, G., Kawano, T., Zheng, H. & Culotti, J. G. UNC-52/perlecan affects gonadal leader cell migrations in *C. elegans* hermaphrodites through alterations in growth factor signaling. *Dev Biol* **256**, 173–186 (2003).

43. Blanchette, C. R., Perrat, P. N., Thackeray, A. & Bénard, C. Y. Glypican Is a Modulator of Netrin-Mediated Axon Guidance. *PLoS Biol* **13**, e1002183 (2015).

44. Brankatschk, M. & Dickson, B. J. Netrins guide *Drosophila* commissural axons at short range. *Nat Neurosci* **9**, 188–194 (2006).

45. Moore, S. W., Biais, N. & Sheetz, M. P. Traction on immobilized netrin-1 is sufficient to reorient axons. *Science* **325**, 166 (2009).

46. Varadarajan, S. G. *et al.* Netrin1 Produced by Neural Progenitors, Not Floor Plate Cells, Is Required for Axon Guidance in the Spinal Cord. *Neuron* **94**, 790-799.e3 (2017).

47. Moore, S. W., Zhang, X., Lynch, C. D. & Sheetz, M. P. Netrin-1 attracts axons through FAK-dependent mechanotransduction. *J Neurosci* **32**, 11574–11585 (2012).

48. Kappler, J. *et al.* Glycosaminoglycan-binding properties and secondary structure of the C-terminus of netrin-1. *Biochem Biophys Res Commun* **271**, 287–291 (2000).

49. Lim, Y. S., Mallapur, S., Kao, G., Ren, X. C. & Wadsworth, W. G. Netrin UNC-6 and the regulation of branching and extension of motoneuron axons from the ventral nerve cord of Caenorhabditis elegans. *J Neurosci* **19**, 7048–7056 (1999).

50. Keino-Masu, K. *et al.* Deleted in Colorectal Cancer (DCC) encodes a netrin receptor. *Cell* **87**, 175–185 (1996).

51. Leonardo, E. D. *et al.* Vertebrate homologues of *C. elegans* UNC-5 are candidate netrin receptors. *Nature* **386**, 833–838 (1997).

52. Hussain, S.-A. *et al.* A molecular mechanism for the heparan sulfate dependence of slit-robo signaling. *J Biol Chem* **281**, 39693–39698 (2006).

53. Fox, A. N. & Zinn, K. The heparan sulfate proteoglycan syndecan is an in vivo ligand for the *Drosophila* LAR receptor tyrosine phosphatase. *Curr Biol* **15**, 1701–1711 (2005).

54. Johnson, K. G. *et al.* The HSPGs Syndecan and Dallylike bind the receptor phosphatase LAR and exert distinct effects on synaptic development. *Neuron* **49**, 517–531 (2006).

55. Shipp, E. L. & Hsieh-Wilson, L. C. Profiling the sulfation specificities of glycosaminoglycan interactions with growth factors and chemotactic proteins using microarrays. *Chem Biol* **14**, 195–208 (2007).

56. Soendenbroe, C., Andersen, J. L. & Mackey, A. L. Muscle-nerve communication and the molecular assessment of human skeletal muscle denervation with aging. *American Journal of Physiology-Cell Physiology* **321**, C317–C329 (2021).

57. Slater, C. R. The Structure of Human Neuromuscular Junctions: Some Unanswered Molecular Questions. *Int J Mol Sci* **18**, 2183 (2017).

58. Wojtowicz, W. M. *et al.* A Human IgSF Cell-Surface Interactome Reveals a Complex Network of Protein-Protein Interactions. *Cell* **182**, 1027-1043.e17 (2020).

59. Liu, W. & Chakkalakal, J. V. The Composition, Development, and Regeneration of Neuromuscular Junctions. *Curr Top Dev Biol* **126**, 99–124 (2018).

60. Rodríguez Cruz, P. M., Cossins, J., Beeson, D. & Vincent, A. The Neuromuscular Junction in Health and Disease: Molecular Mechanisms Governing Synaptic Formation and Homeostasis. *Front Mol Neurosci* **13**, 610964 (2020).

61. van der Merwe, P. A. & Barclay, A. N. Transient intercellular adhesion: the importance of weak protein-protein interactions. *Trends Biochem Sci* **19**, 354–358 (1994).

62. Bushell, K. M., Söllner, C., Schuster-Boeckler, B., Bateman, A. & Wright, G. J. Large-scale screening for novel low-affinity extracellular protein interactions. *Genome Res* **18**, 622–630 (2008).

63. Özkan, E. *et al.* An Extracellular Interactome of Immunoglobulin and LRR Proteins Reveals Receptor-Ligand Networks. *Cell* **154**, 228–239 (2013).

64. Li, H. *et al.* Deconstruction of the beaten Path-Sidestep interaction network provides insights into neuromuscular system development. *eLife* **6**, e28111 (2017).

65. Bonanomi, D. & Pfaff, S. L. Motor Axon Pathfinding. *Cold Spring Harb Perspect Biol* **2**, a001735 (2010).

66. Pittman, A. J., Law, M.-Y. & Chien, C.-B. Pathfinding in a large vertebrate axon tract: isotypic interactions guide retinotectal axons at multiple choice points. *Development* **135**, 2865–2871 (2008).

67. Sink, H., Rehm, E. J., Richstone, L., Bulls, Y. M. & Goodman, C. S. sidestep Encodes a Target-Derived Attractant Essential for Motor Axon Guidance in Drosophila. *Cell* **105**, 57–67 (2001).

68. Van Vactor, D., Sink, H., Fambrough, D., Tsoo, R. & Goodman, C. S. Genes that control neuromuscular specificity in Drosophila. *Cell* **73**, 1137–1153 (1993).

69. Pipes, G. C. T., Lin, Q., Riley, S. E. & Goodman, C. S. The Beat generation: a multigene family encoding IgSF proteins related to the Beat axon guidance molecule in Drosophila. *Development* **128**, 4545–4552 (2001).

70. Vogel, C., Teichmann, S. A. & Chothia, C. The immunoglobulin superfamily in Drosophila melanogaster and Caenorhabditis elegans and the evolution of complexity. *Development* **130**, 6317–6328 (2003).

71. Mushegian, A. R. The Drosophila Beat protein is related to adhesion proteins that contain immunoglobulin domains. *Current Biology* **7**, R336–R338 (1997).

72. Bazan, J. F. & Goodman, C. S. Modular structure of the Drosophila Beat protein. *Current Biology* **7**, R338–R339 (1997).

73. Heymann, C. *et al.* Molecular insights into the axon guidance molecules Sidestep and Beaten path. *Frontiers in Physiology* **13**, (2022).

74. Fambrough, D. & Goodman, C. S. The Drosophila beaten path Gene Encodes a Novel Secreted Protein That Regulates Defasciculation at Motor Axon Choice Points. *Cell* **87**, 1049–1058 (1996).

75. Siebert, M., Banovic, D., Goellner, B. & Aberle, H. Drosophila motor axons recognize and follow a Sidestep-labeled substrate pathway to reach their target fields. *Genes Dev* **23**, 1052–1062 (2009).

76. Geisbrecht, B. V., Dowd, K. A., Barfield, R. W., Longo, P. A. & Leahy, D. J. Netrin binds discrete subdomains of DCC and UNC5 and mediates interactions between DCC and heparin. *J Biol Chem* **278**, 32561–32568 (2003).

77. Xu, K. *et al.* Neural migration. Structures of netrin-1 bound to two receptors provide insight into its axon guidance mechanism. *Science* **344**, 1275–1279 (2014).

78. Finci, L. I. *et al.* The crystal structure of netrin-1 in complex with DCC reveals the bifunctionality of netrin-1 as a guidance cue. *Neuron* **83**, 839–849 (2014).

79. Seiradake, E. *et al.* FLRT structure: balancing repulsion and cell adhesion in cortical and vascular development. *Neuron* **84**, 370–385 (2014).

80. Jackson, V. A. *et al.* Super-complexes of adhesion GPCRs and neural guidance receptors. *Nat Commun* **7**, 11184 (2016).

81. Stetefeld, J., McDougall, M. D., Loewen, P. C., Moya, A. & Meier, M. RCSB PDB - 6OOL: Structural elucidation of the Ectodomain of mouse UNC5H2. (2020) doi:10.2210/pdb6OOL/pdb.

82. Fukuhara, N., Howitt, J. A., Hussain, S.-A. & Hohenester, E. Structural and functional analysis of slit and heparin binding to immunoglobulin-like domains 1 and 2 of *Drosophila* Robo. *J Biol Chem* **283**, 16226–16234 (2008).

83. Hong, K. *et al.* A ligand-gated association between cytoplasmic domains of UNC5 and DCC family receptors converts netrin-induced growth cone attraction to repulsion. *Cell* **97**, 927–941 (1999).

84. Grandin, M. *et al.* Structural Decoding of the Netrin-1/UNC5 Interaction and its Therapeutical Implications in Cancers. *Cancer Cell* **29**, 173–185 (2016).

85. Leclère, L. & Rentzsch, F. Repeated evolution of identical domain architecture in metazoan netrin domain-containing proteins. *Genome Biol Evol* **4**, 883–899 (2012).

86. Hedgecock, E. M., Culotti, J. G., Hall, D. H. & Stern, B. D. Genetics of cell and axon migrations in *Caenorhabditis elegans*. *Development* **100**, 365–382 (1987).

87. Kimble, J. E. & White, J. G. On the control of germ cell development in *Caenorhabditis elegans*. *Dev Biol* **81**, 208–219 (1981).

88. Hamelin, M., Zhou, Y., Su, M. W., Scott, I. M. & Culotti, J. G. Expression of the UNC-5 guidance receptor in the touch neurons of *C. elegans* steers their axons dorsally. *Nature* **364**, 327–330 (1993).

89. Wadsworth, W. G., Bhatt, H. & Hedgecock, E. M. Neuroglia and pioneer neurons express UNC-6 to provide global and local netrin cues for guiding migrations in C. elegans. *Neuron* **16**, 35–46 (1996).

90. Kinnunen, T. *et al.* Heparan 2-O-sulfotransferase, hst-2, is essential for normal cell migration in Caenorhabditis elegans. *Proc Natl Acad Sci U S A* **102**, 1507–1512 (2005).

91. Suzuki, N., Toyoda, H., Sano, M. & Nishiwaki, K. Chondroitin acts in the guidance of gonadal distal tip cells in C. elegans. *Dev Biol* **300**, 635–646 (2006).

92. Evans, R. *et al.* Protein complex prediction with AlphaFold-Multimer. 2021.10.04.463034 Preprint at https://doi.org/10.1101/2021.10.04.463034 (2022).

93. Mirdita, M. *et al.* ColabFold: making protein folding accessible to all. *Nat Methods* **19**, 679–682 (2022).

94. Yin, R., Feng, B. Y., Varshney, A. & Pierce, B. G. Benchmarking AlphaFold for protein complex modeling reveals accuracy determinants. *Protein Sci* **31**, e4379 (2022).

95. Kruger, R. P., Lee, J., Li, W. & Guan, K.-L. Mapping netrin receptor binding reveals domains of Unc5 regulating its tyrosine phosphorylation. *J Neurosci* **24**, 10826–10834 (2004).

96. Bushell, K. M., Söllner, C., Schuster-Boeckler, B., Bateman, A. & Wright, G. J. Large-scale screening for novel low-affinity extracellular protein interactions. *Genome Res* **18**, 622–630 (2008).

97. Reale, M. A. *et al.* Expression and alternative splicing of the deleted in colorectal cancer (DCC) gene in normal and malignant tissues. *Cancer Res* **54**, 4493–4501 (1994).

98. Cooper, H. M., Armes, P., Britto, J., Gad, J. & Wilks, A. F. Cloning of the mouse homologue of the deleted in colorectal cancer gene (mDCC) and its expression in the developing mouse embryo. *Oncogene* **11**, 2243–2254 (1995).

99. Leggere, J. C. *et al.* NOVA regulates Dcc alternative splicing during neuronal migration and axon guidance in the spinal cord. *eLife* **5**, (2016).

100. Finci, L. I. *et al.* Structure of unliganded membrane-proximal domains FN4-FN5-FN6 of DCC. *Protein Cell* **8**, 701–705 (2017).

101. Gao, X. *et al.* A Floor-Plate Extracellular Protein-Protein Interaction Screen Identifies Draxin as a Secreted Netrin-1 Antagonist. *Cell Rep* **12**, 694–708 (2015).

102. Lim, Y. & Wadsworth, W. G. Identification of domains of netrin UNC-6 that mediate attractive and repulsive guidance and responses from cells and growth cones. *J Neurosci* **22**, 7080–7087 (2002).

103. Liu, Y. *et al.* Structural Basis for Draxin-Modulated Axon Guidance and Fasciculation by Netrin-1 through DCC. *Neuron* **97**, 1261-1267.e4 (2018).

104. Taylor, S. R. *et al.* Molecular topography of an entire nervous system. *Cell* **184**, 4329-4347.e23 (2021).

105. Meier, M. *et al.* The dynamic nature of netrin-1 and the structural basis for glycosaminoglycan fragment-induced filament formation. *Nat Commun* **14**, 1226 (2023).

106. Krahn, N. *et al.* Solution Structure of *C. elegans* UNC-6: A Nematode Paralogue of the Axon Guidance Protein Netrin-1. *Biophys J* **116**, 2121–2130 (2019).

107. Chao, G. *et al.* Isolating and engineering human antibodies using yeast surface display. *Nat Protoc* **1**, 755–768 (2006).

108. Kabsch, W. *XDS*. *Acta Crystallogr D Biol Crystallogr* **66**, 125–132 (2010).

109. McCoy, A. J. *et al. Phaser* crystallographic software. *J Appl Crystallogr* **40**, 658–674 (2007).

110. Liebschner, D. *et al.* Macromolecular structure determination using X-rays, neutrons and electrons: recent developments in *Phenix*. *Acta Crystallogr D Struct Biol* **75**, 861–877 (2019).

111. Webb, B. & Sali, A. Comparative Protein Structure Modeling Using MODELLER. *Curr Protoc Bioinformatics* **54**, 5.6.1-5.6.37 (2016).

112. Varadi, M. *et al.* AlphaFold Protein Structure Database: massively expanding the structural coverage of protein-sequence space with high-accuracy models. *Nucleic Acids Res* **50**, D439–D444 (2022).

113. Afonine, P. V. *et al.* Towards automated crystallographic structure refinement with *phenix.refine*. *Acta Crystallogr D Biol Crystallogr* **68**, 352–367 (2012).

114. Emsley, P., Lohkamp, B., Scott, W. G. & Cowtan, K. Features and development of *Coot*. *Acta Crystallogr D Biol Crystallogr* **66**, 486–501 (2010).

115. Chen, V. B. *et al. MolProbity*: all-atom structure validation for macromolecular crystallography. *Acta Crystallogr D Biol Crystallogr* **66**, 12–21 (2010).

116. Tickle, I. J. *et al.* STARANISO. (2018).

117. Jurrus, E. *et al.* Improvements to the APBS biomolecular solvation software suite. *Protein Sci* **27**, 112–128 (2018).

118. Ashkenazy, H. *et al.* ConSurf 2016: an improved methodology to estimate and visualize evolutionary conservation in macromolecules. *Nucleic Acids Res* **44**, W344-350 (2016).

119. Gasteiger, E. *et al.* Protein Identification and Analysis Tools on the ExPASy Server. in *The Proteomics Protocols Handbook* (ed. Walker, J. M.) 571–607 (Humana Press, 2005). doi:10.1385/1-59259-890-0:571.

120. Zivanov, J. *et al.* New tools for automated high-resolution cryo-EM structure determination in RELION-3. *eLife* **7**, e42166 (2018).

121. Kirby, N. *et al.* Improved radiation dose efficiency in solution SAXS using a sheath flow sample environment. *Acta Crystallogr D Struct Biol* **72**, 1254–1266 (2016).

122. Hopkins, J. B., Gillilan, R. E. & Skou, S. *BioXTAS RAW*: improvements to a free open-source program for small-angle X-ray scattering data reduction and analysis. *J Appl Crystallogr* **50**, 1545–1553 (2017).

123. Manalastas-Cantos, K. *et al. ATSAS 3.0*: expanded functionality and new tools for small-angle scattering data analysis. *J Appl Crystallogr* **54**, 343–355 (2021).

124. Meisburger, S. P. *et al.* Domain Movements upon Activation of Phenylalanine Hydroxylase Characterized by Crystallography and Chromatography-Coupled Small-Angle X-ray Scattering. *J Am Chem Soc* **138**, 6506–6516 (2016).

125. Bushell, K. M., Söllner, C., Schuster-Boeckler, B., Bateman, A. & Wright, G. J. Large-scale screening for novel low-affinity extracellular protein interactions. *Genome Res* **18**, 622–630 (2008).

126. Liu, Y. *et al.* Structural Basis for Draxin-Modulated Axon Guidance and Fasciculation by Netrin-1 through DCC. *Neuron* **97**, 1261-1267.e4 (2018).

127. Gao, X. *et al.* A Floor-Plate Extracellular Protein-Protein Interaction Screen Identifies Draxin as a Secreted Netrin-1 Antagonist. *Cell Rep* **12**, 694–708 (2015).

128. Carrillo, R. A. *et al.* Control of Synaptic Connectivity by a Network of Drosophila IgSF Cell Surface Proteins. *Cell* **163**, 1770–1782 (2015).

129. Özkan, E. *et al.* Extracellular Architecture of the SYG-1/SYG-2 Adhesion Complex Instructs Synaptogenesis. *Cell* **156**, 482–494 (2014).

130. Chao, D. L. & Shen, K. Functional dissection of SYG-1 and SYG-2, cell adhesion molecules required for selective synaptogenesis in C. elegans. *Molecular and Cellular Neuroscience* **39**, 248–257 (2008).

131. Verdino, P., Witherden, D. A., Havran, W. L. & Wilson, I. A. The molecular interaction of CAR and JAML recruits the central cell signal transducer PI3K. *Science* **329**, 1210–1214 (2010).

132. Krahn, N. *et al.* Solution Structure of C. elegans UNC-6: A Nematode Paralogue of the Axon Guidance Protein Netrin-1. *Biophysical Journal* **116**, 2121–2130 (2019).

133. Finci, L. I. *et al.* The Crystal Structure of Netrin-1 in Complex with DCC Reveals the Bifunctionality of Netrin-1 As a Guidance Cue. *Neuron* **83**, 839–849 (2014).

134. Xu, K. *et al.* Structures of Netrin-1 Bound to two Receptors Provide Insight into its Axon Guidance Mechanism. *Science* **344**, 1275–1279 (2014).

135. Geisbrecht, B. V., Dowd, K. A., Barfield, R. W., Longo, P. A. & Leahy, D. J. Netrin Binds Discrete Subdomains of DCC and UNC5 and Mediates Interactions between DCC and Heparin. *Journal of Biological Chemistry* **278**, 32561–32568 (2003).

136. Vallet, S. D., Clerc, O. & Ricard-Blum, S. Glycosaminoglycan–Protein Interactions: The First Draft of the Glycosaminoglycan Interactome. *J Histochem Cytochem.* **69**, 93–104 (2021).

137. Clerc, O. *et al.* A pipeline to translate glycosaminoglycan sequences into 3D models. Application to the exploration of glycosaminoglycan conformational space. *Glycobiology* **29**, 36–44 (2019).

138. Powell, A. K., Yates, E. A., Fernig, D. G. & Turnbull, J. E. Interactions of heparin/heparan sulfate with proteins: Appraisal of structural factors and experimental approaches. *Glycobiology* **14**, 17R-30R (2004).

139. Gallagher, J. R., Kim, A. J., Gulati, N. M. & Harris, A. K. Negative-Stain Transmission Electron Microscopy of Molecular Complexes for Image Analysis by 2D Class Averaging. *Current Protocols in Microbiology* **54**, e90 (2019).

140. Scheres, S. H. W. RELION: Implementation of a Bayesian approach to cryo-EM structure determination. *Journal of Structural Biology* **180**, 519–530 (2012).

141. Thompson, R. F., Walker, M., Siebert, C. A., Muench, S. P. & Ranson, N. A. An introduction to sample preparation and imaging by cryo-electron microscopy for structural biology. *Methods* **100**, 3–15 (2016).

142. Pellegrini, L., Burke, D. F., von Delft, F., Mulloy, B. & Blundell, T. L. Crystal structure of fibroblast growth factor receptor ectodomain bound to ligand and heparin. *Nature* **407**, 1029–1034 (2000).

143. Sasaki, T. *et al.* Structural basis and potential role of heparin/heparan sulfate binding to the angiogenesis inhibitor endostatin. *The EMBO Journal* **18**, 6240–6248 (1999).

144. Zhang, C. *et al.* Structure-based engineering of heparinase I with improved specific activity for degrading heparin. *BMC Biotechnol* **19**, 59 (2019).

145. Wienen-Schmidt, B., Oebbeke, M., Ngo, K., Heine, A. & Klebe, G. Two Methods, One Goal: Structural Differences between Cocrystallization and Crystal Soaking to Discover Ligand Binding Poses. *ChemMedChem* **16**, 292–300 (2021).